Faculdade de Engenharia da Universidade do Porto

Instituto de Ciências Biomédicas Abel Salazar

Engineered hydrogel coating for improved biocompatibility of chronically implanted neural electrodes

Ana Isabel Rocha Stüve

THESIS SUBMITTED FOR THE DEGREE OF MASTER IN

BIOENGINEERING

Supervisor: Dr Isabel Freitas Amaral

Co-Supervisor: Dr Victoria Leiro

September 15, 2022

Engineered hydrogel coating for improved biocompatibility of chronically implanted neural electrodes

Author:
Ana Stüve

Supervisor:
Isabel Freitas Amaral
Co-Supervisor:
Victoria Leiro

Thesis submitted for the degree of Master in
Molecular Biotechnology

Faculdade de Engenharia da Universidade do Porto
Instituto de Ciências Biomédicas Abel Salazar

15 September 2022

The work presented in this thesis was developed at the following institutions:

nBTT - nanoBiomaterials for Targeted Therapies Group
i3S - Instituto de Investigação e Inovação em Saúde
INEB - Instituto Nacional de Engenharia Biomédica
Universidade do Porto, Portugal

Atomic force microscopy studies and fluorescence microscopy were conducted at the Bioimaging i3S Scientific Platform, member of the PPBI (PPBI-POCI-01-0145-FEDER-022122, with the assistance of Manuela Brás and Dalila Pedro, respectively. Contact angle measurements, imaging ellipsometry studies and ATR-FTIR were carried out at the Biointerfaces and Nanotechnology (BN) core facility of i3S, with the assistance of Ricardo Vidal. The authors acknowledge the support of the i3S Scientific Platform BioSciences Screening [and other scientific Platforms, if applies], member of the national infrastructures PT-OPENSCREEN (NORTE-01-0145-FEDER-085468) and PPBI - Portuguese Platform of Bioimaging (PPBI-POCI-01-0145-FEDER-022122), with the assistance of André Maia. This work was funded by Portuguese funds through FCT, in the framework of project BioCoat - Engineered biomimetic hydrogel coating for improved biocompatibility of chronically-implanted neural electrodes - (EXPL/BTM-MAT/1499/2021).

Abstract

Implantable neural interfaces are promising tools for understanding and regulating the CNS through the recording of neural electrical impulses or the stimulation of brain tissue. The clinical benefits of brain implants include improvements in the quality of life of patients suffering from a wide range of neurological disorders, such as Parkinson's disease and essential tremors. Intracortical electrodes, due to their high signal resolution acquisition, have been explored for brain-machine interfaces, platforms with the potential to help restore communication and movement in paralyzed patients.

Although penetrating neural implants have shown promising results in acute applications, their performance is significantly limited in clinically relevant chronic settings. Electrode implantation causes injury to the surrounding brain tissue, resulting in blood-brain barrier disruption and damage to neuronal and glial cells. The adsorption of extravasated plasma proteins onto the implant surface and the infiltration of neutrophils and monocytes, trigger the resident microglia and astrocytes to become activated and release pro-inflammatory factors. This inflammatory response leads to increased neuronal cell loss at the electrode-tissue interface, which in turn, often develops into a chronic inflammation, characterized by a glial scar formation. This process is known as foreign body reaction (FBR) and can result in the isolation of the implant from target neurons, both electrically and mechanically, compromising the electrical performance of the electrode, and eventually leading to instability and device failure.

Overwhelming efforts have been put into designing innovative approaches to overcome the FBR. Due to the mechanical mismatch between currently employed electrodes and soft brain tissue, which contributes to chronic inflammation, compliant materials and coating strategies have been developed. Anti-fouling coatings have also proven to be effective to prevent non-specific protein adsorption and to reduce astrocytic recruitment and electrode impedance. Yet, non-fouling coatings *per se* are not enough to reduce neuronal loss and glial scar formation after electrode implantation.

Biomimetic coatings replicating the brain tissue extracellular matrix (ECM) have also been explored to improve electrode integration. Among the most important ECM proteins explored for neural applications is laminin (LN), a protein highly expressed in the cerebrovascular basal lamina capable of mediating neuronal cell adhesion and neurite extension. LN incorporation into biomimetic coatings has shown promise in improving neuronal cell adhesion to neural electrodes and neurite outgrowth, *in vitro*. Besides, LN immobilization through its agrin-binding domain *via* high affinity binding has been shown to better preserve LN bioactivity, as compared to other immobilization approaches. However, the ability of site-specific immobilized LN to improve the integration of implantable neural electrodes is still to be assessed.

In this work, we developed a mechanically compliant and anti-fouling hydrogel coating presenting site-selective immobilized LN, for application in electrode-neural interfaces. Such hydrogel is expected to direct neurite outgrowth toward the surface of implantable neural electrode while preventing non-specific protein adsorption and cell adhesion, which contribute to glial scar formation. To test this hypothesis, polyurethane (PU) and parylene-c substrates were used as surrogates of PU- and parylene-c-insulated deep brain and intracortical electrodes, respectively. The hydrogel coating was formed by immersing sequentially the substrates in a solution of four-arm maleimide terminated poly(ethylene glycol) (PEG-4MAL) or PEG-dithiol, each sequential immersion in PEG-MAL and in the cross-linker solution being considered one treatment. The resultant hydrogel coating was finally functionalized with a recombinant human N-terminal agrin (NtA) domain, to promote high affinity binding of laminin.

To assure a stable binding of the hydrogel, substrate surfaces were functionalized with maleimide (MAL) groups using silane-PEG-maleimide, to allow the covalent binding of the hydrogel precursor PEG-4MAL using dithiol. Due to the hydrophobic nature of parylene-c and PU surfaces, both surfaces were activated with oxygenated groups via O_2 or UVO plasma, to introduce free hydroxyl groups at the

surface, capable of reacting with silane groups. Different plasma exposure times were tested. All plasma treatments were effective in increasing the hydrophilicity of the surfaces, as shown by water contact angle (WCA) measurements. Parylene surfaces reached a constant WCA after only 2 seconds. Interestingly, XPS analyses also revealed for this O_2 plasma exposure time a higher relative percentage of OH groups. PU surfaces attained a constant WCA after 200 s of UVO plasma treatment, and the presence of oxygenated species was validated by XPS analysis.

Different concentrations of silane-PEG-MAL (5, 10, and 25 mM) were tested for surface functionalization. Maleimide surface density quantification confirmed the presence of maleimide groups on both substrates, particularly for the highest concentration tested. These results were well supported by XPS analysis. Moreover, since the maleimide surface density on parylene-c surfaces was not affected by the exposure time to O_2 plasma, an exposure time of 5 s was selected for parylene-c surface activation instead of 2 s, for higher consistency among assays.

Synthetic hydrogels based on PEG-4MAL and PEG-dithiol were successfully deposited on parylene-c surfaces via the Michael-type addition reaction, leading to a distinct surface morphology when compared with unmodified parylene-c surfaces. These differences were more evident after 4 treatments of PEG-4MAL/PEG-dithiol.

The deposition of a PEG-4MAL hydrogel decorated with site-specific immobilized LN was performed on parylene surfaces subjected to a single PEG-4MAL/PEG-dithiol treatment, as a proof-of-concept. After the treatment, substrates were immersed in PEG-4MAL and then in NtA solutions, varying NtA concentrations (5 and 10 μM).

LN immobilization was assessed by examining LN distribution at the surface by immunofluorescence, at a first approach. Results confirmed the presence of LN on NtA-functionalized coatings, for the NtA concentrations tested. The ability of the developed coating to support cell adhesion of cortical neurons was subsequently assessed. A trend for higher numbers of adhered cells was found on PEG-4MAL coatings decorated with site-specific immobilized LN, when compared to bare PEG-4MAL coatings, particularly for the highest NtA concentration tested.

Altogether, these results suggest that the coating of parylene-c and PU-insulated electrodes with PEG-MAL-based hydrogels decorated with site-specific immobilized LN may be of interest to enhance the biocompatibility of electrode-neural interfaces. Further studies are required in order to validate the present findings and to assess the full potential of this engineered coating.

Acknowledgements

These pages mark the final of a long and happy road along 5 years. These years have taught me the value of challenging myself outside my comfort zone and being open to embarking on new challenges. I am grateful for all the lessons I have learned and especially, for all the people I get to meet through this experience.

First, I would like to express my gratitude to Dr Isabel Amaral, for all the time and effort she has put into our project, for everything she has taught me, for inspiring me to think like an engineer when faced with a challenging task, and for always celebrating our successes. Working with someone so passionate about their work (and result analysis) is incredibly encouraging. Secondly, I would like to thank my co-supervisor Dr Victoria Leiro, for all the scientific input, advice and constructive feedback, particularly concerning chemistry details that are fundamental for scientific growth. I also want to thank Dr Ana Paula Pêgo for welcoming me to the group and for giving me the opportunity to work on this project. For being an example of leadership, cooperation, and dedication.

Finally, to all my colleagues at nBTT, for making me feel like one of them from the first day and for always being available for any questions, even the most trivial ones. I learned a lot from this extraordinary group of people, and I am very grateful for getting to know you. A special mention to all my master colleagues, for sharing this experience with me. It would have not been the same without you. Thank you for always being there for me, and for all the coffees Theodora and I never drank.

To all the members of the i3S community who contributed to the development of this work, particularly to Ricardo Vidal, for all the availability and technical guidance across a wide range of techniques and to Manuela Brás, for all her time around the AFM and scientific advice.

I would also like to give a special thanks to professor Susana Cardoso Freitas (INES-MN) for kindly preparing the silicon substrates used in this project, and to Jorge Martins, Dzimitry Ivanou and professor Adélio Mendes from (LEPABE/FEUP) for always receiving us with the most sympathy and borrow us their UVO equipment.

Now, I would like to thank and spread my appreciation to all my friends who were always by my side, supporting all my choices and encouraging me to never give up. I am truly thankful for having such a group of inspiring and different friends that teach me more than they could ever imagine. I also had to express my gratitude to my family, without whom I'm sure I would not have accomplished as much in my life. Thank you for all your love and wisdom words, which keep going even when I didn't think I could. Thank you for laughing and crying alongside me, only to see me happy, I could not have asked for a greater support team to keep me going.

Lastly, I want to thank a person that has become really important in my life, Pedro. Your perspective on life, enthusiasm and passion have been very inspiring to me. Thank you for not only supporting me during my difficult moments but also celebrating my accomplishments.

Contents

List of Figures

List of Tables

Abbreviations

AFM Atomic force microscopy

ATR-FTIR Attenuated total reflectance fourier transformed infra-red

BBB Blood Brain Barrier

BE Binding energy

BMI Brain-machine interface

CNS Central Nervous System

DBS Deep brain stimulation

ECM Extracellular matrix

ECoG Electrocorticography

EEG Electroencephalography

FBR Foreign body response

FTIR Fourier transformed infra-red spectroscopy

FWHM Full width at half maximum

GFAP Glial fibrillary acid protein

GSH reduced glutathione

HEPES 4-(2-hydroxyethyl) piperazine-1-ethanesulfonic acid

hNSC Human neural stem cells

IBA-1 ionized calcium-binding adapter molecule 1

iBMI Intra-cortical brain-machine interface

LN Laminin

MAL Maleimide

MEA Microelectrode arrays

MEMS Microelectromechanical systems

MMEA Michigan microelectrode arrays

PBS Phosphate buffered saline

PD Parkinson disease

PEG Poly(ethylene glycol)

PEG-4MAL Four-arm maleimide-terminated poly(ethylene glycol)

PFA Paraformaldehyde

PU Polyurethane

RPM rotations per minute

RT Room temperature

silane-PEG-MAL silane-poly(ethylene glycol)-maleimide

UEA Utah Array

v/v Volume per volume

w/v Weight per volume

THF Tetrahydrofuran

UVO UV/ozone

XPS X-ray photoelectron spectroscopy

Chapter 1

Introduction

This chapter starts by briefly reviewing the most important components of the central nervous system (CNS). An overview of the current neural interfaces is provided, with emphasis on invasive and penetrating interfaces. Their clinical applications are briefly described, and an analysis of the neural engineering market size is also provided.

1.1. Central Nervous system: structure and function

The human nervous system is a complex and distinctive network that manages our actions, reactions, and sensations. It can be divided into two main parts, the central nervous system (CNS) and the peripheral nervous system (PNS) [1]. CNS is responsible for processing the information obtained by the PNS and includes the brain and spinal cord. While the brain regulates body functions such as movement, thinking, speech, and the five senses, the spinal cord can transmit messages towards and from the brain through peripheral nerves [2]. The brain is the most complex component of the human body. The cells in the brain that are involved in essential neurological processes include neurons and glial cells. The human brain has 86 billion neurons communicating with each other and with muscles through electrical signals. Neurons are known as the building blocks of the nervous system, while glial cells have an important role in supporting neuronal development and signalling [2].

1.2. Neural interfaces

Neural interfaces are recording devices that establish the interfaces between the nervous system and external devices [3]. Communication through these interfaces can go in two directions. Electrical recording allows information to be extracted from the neurological system, whereas electrical stimulation, such as neuron stimulation, allows information to be delivered into the nervous system [4]. Applications for neural interfaces include basic neuroscience research to understand the underlying behaviour of the nervous system, neural-information encoding, understanding disease causes, as well as treatments for neurological disorders [5][6].

Metal wire recording of electrophysiological signals in human individuals was first recorded in the 1940s but acquired information was insufficient to grasp how the complex neural circuitry of the brain works [7]. In 1999 the manipulation of a robotic arm by cortical neurons triggered the interest of the scientific community in neural engineering [8]. Later, the activity of the motor cortex of monkeys to control the cursor position on a monitor was recorded by intracortical multi-electrodes arrays. The neuronal activity recorded was then used by the same monkey to reproduce the task [9].

As seen in **Figure 1**, different neural interfaces have been developed according to the level of invasiveness. Electrodes can be non-invasive such as electroencephalography (EEG) scalp electrodes, and invasive such as epi/subdural electrocorticography (ECoG) arrays, intracortical microelectrode arrays (MEAs) and depth electrodes. The obvious advantage of non-invasive interfaces includes the safety of recording signals from the scalp not only on patients but on the general population. Neural electrodes have a trade-off between signal resolution and invasiveness. Contrary to non-invasive electrodes, invasive electrodes record high-quality and reliable signals from neuron populations, with safety being a major concern [10].

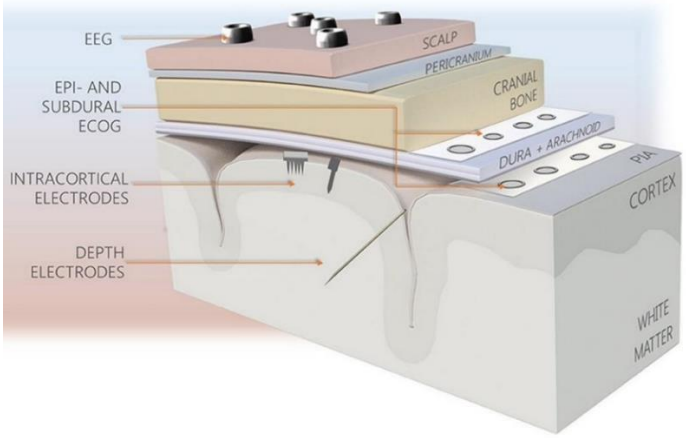

Figure 1 **-** Types of brain interfacing electrodes and their locations in reference to the brain. Reprinted from [11], under a creative commons attribution (CC BY).

EEG records electrical impulses from a network of scalp-attached electrodes and is the most popular method for studying the brain [7]. The brain signals are acquired with a high temporal and low spatial resolution. EEG recordings are widely used for drug-resistant epilepsy studies, offering solutions for communication [12]. However, these recording devices aren't able to obtain high-quality neuronal recordings in deeper regions of the brain due to signal attenuation passing through the dura, skull, and scalp [6].

Currently, non-invasive signals state about 80% accuracy. While signal resolution can be appropriate for communication tasks, neurorehabilitation or evaluating the patient condition, it is unsatisfactory for controlling external devices such as wheelchairs, cars or prosthetic hands [13]. As such, invasive electrodes hold great potential for accurate signal control in complex applications.

ECoG-based electrodes provide electrical signal improvement compared to EEG-based techniques since they are recorded from the epidural or subdural area closer to the cortical surface. This technique offers a high signal-to-noise ratio, less sensitivity to distortion factors, and a high spatial and temporal resolution. [14] Additionally, ECoG electrode implantation only involves minimally invasive surgery, without intrusion into brain tissue. ECoG stimulation technique is commonly used to decode small brain signals. Clinic applications include localization of epileptic foci and communication solutions (movement, vision and speech decoding) [15].

Intracortical and deep brain electrodes are in close proximity to neuronal processes, being able to obtain signals with a higher spatiotemporal resolution than ECoG electrodes. The advantage of improved signal resolution is the capacity of single-neuron recordings, that when combined with current developments in computational capabilities, allows a relatively high level of information specificity [16].

In the last decade, neural interfaces have been promoting brain health, from regulating mood disorders or neurological diseases via deep brain stimulation (DBS) [17] to controlling brain-machine interfaces (BMI) through the use of intracortical multi-electrodes arrays [15].

1.2.1. Intracortical Recording Interfaces

The innovation of materials and advances in microelectromechanical systems (MEMS) enabled researchers to fabricate a wide variety of **intracortical arrays** that record and stimulate neural elements in animal brains with a high density of electrodes [18]. Technological advances in the field led to penetrating multi-electrode arrays with geometric surface areas typically smaller than 10,000 μm^2,

allowing increased proximity to the CNS. These electrodes interact closely with neuron populations, enabling stable brain electrical signal records and high precision cortical neuron stimulation (micro- to millivolt electrical signals) [19]. Multi-electrode arrays (MEAs) can be distributed in three types of devices: microwire arrays, fabricated planar arrays, and machined arrays. **Figure 2** is a schematic representation of the current MEAs design.

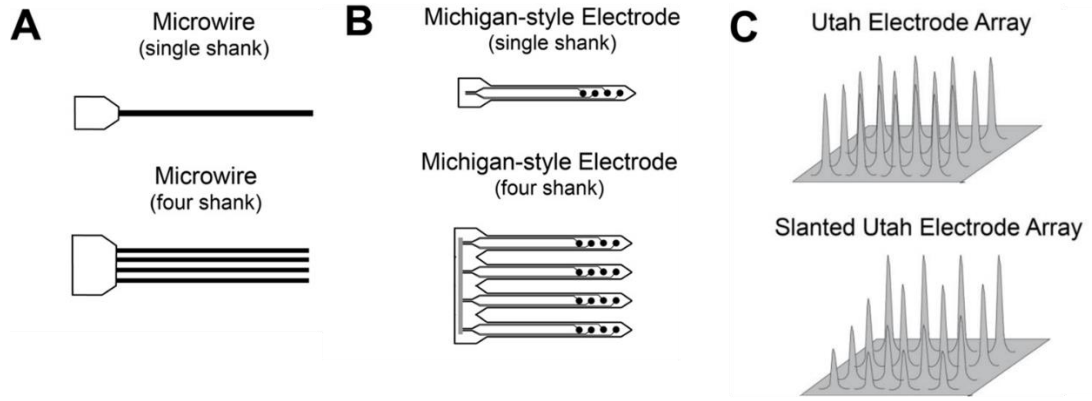

Figure 2 **-** Schematic representation of the generic design of leading microelectrode array technologies, including A) Microwires, B) Michigan Microelectrodes Arrays, and C) Utah Electrode Arrays (EUA). Adapted with permission from [20]. Copyright © 2015, IOP Publishing Ltd.

Figure 2A shows a schematic representation of a single and four-shank microwire. **Microwires** have been commonly used to capture neuronal activity in the brains of rodents and primates [21]. These can either be custom-designed or commercially available (e.g. Plexon Inc., Microprobes) and typically have a 25-50 µm shank [22]. Microwires are thin wires with a usual core made of tungsten, stainless steel, steel alloys, iridium, or platinum. The common insulation for microwires is glass, parylene-C, polyimide, or Teflon. The electrode tips can be sharpened or left unpolished as desired. Metal is typically exposed at the tips of the electrodes to lower impedance at the recording point. However, the use of a single electrode per shank restricts the positioning of electrode sites [22].

Improvements in microelectromechanical systems (MEMS) techniques and semiconducting materials made the fabrication of silica-based microelectrodes arrays (planar and machined arrays) became possible [21].

Planar arrays are planar structure devices produced using photolithography techniques, by conductive and nonconductive material deposition on a silicon substrate. Metals like gold or iridium are frequently utilized to make conductive electrodes, which are then covered with polymer coatings similar to those found on microwires to provide insulation [21]. The development of planar arrays leads to the fabrication of **Michigan microelectrode arrays (MMEA)**. The basic structure of a single-shank MMEA microelectrode is shown in **Figure 2B**. MMEAs typically have shanks 5 mm long, spaced 400 m apart, and with thicknesses of 15 µm or 50 µm. These electrodes contain up to four recording sites along the length of the shank and can contain a range from one to 16 shanks. MMEA electrode advantages include the capacity to record from several places at precisely controlled tissue depths [22].

Machined arrays are high-density arrays that assemble various microelectrodes in a limited region of the cortex. The electrodes are produced through dicing, etching, and glass reflow of a silicon substrate. Next, shanks are covered with a conductive material, often platinum or iridium, and an insulator material, such as parylene-c, that similarly to the other electrodes is removed at the tips to expose the recording sites [21]. The most known machined array is **Utah Array (UEA)** used in rodents, small animals, primates and human studies [22]. A basic schematic of the UEA is shown in **Figure 2C**. UEA high-density arrays have a standard shank length range of 0.5 to 1.5 mm and 0,4 mm of separation from each other. Normally, UEA clusters 100 microelectrodes (10x10 array) in an area of the cortex that is just 16 mm^2 in size [23]. At the moment, UEA is the only high-density, penetrating recording electrode that

has been authorized by the US Food and Drug Administration and has been given the CE mark for usage in Europe [20].

Additionally, MEAs can be designed in two different configurations: tethered to the cranium or untethered, as shown in **Figure 3**. Untethered electrodes are tightly fixed to the skull and implanted into the brain parenchyma at the appropriate depths using an insertion tool. In terms of electrode characteristics and shank design, tethered arrays are comparable to untethered arrays; however, stability is accomplished with a flexible cable that connects the electrode to a connector that is placed rigidly inside the skull. Untethered configuration aims to decrease brain micromotion caused by tissue reactions [22].

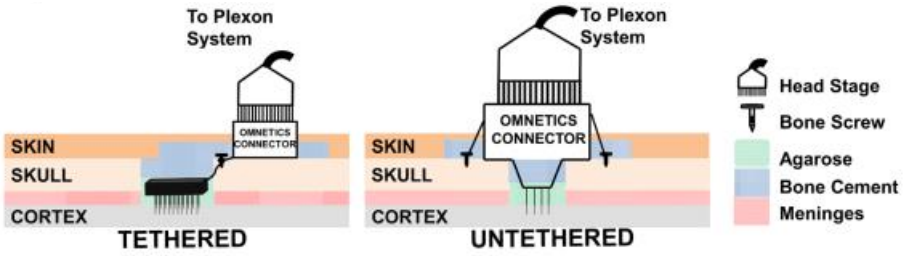

Figure 3 **-** Depiction of intracortical neural interface platform insertion and head cap placement in the case of the tethered and untethered probes. Adapted with permission from [22]. Copyright © 2015 American Chemical Society.

1.2.1.1. Intra cortical Applications

In 2013, a survey estimated that more than 5.4 million people in the USA suffered from paralysis [24]. This devastating condition is related to severe neurological disorders such as amyotrophic lateral sclerosis (ALS), brainstem strokes, and spinal cord injury (SCI), which disrupt neural pathways, limiting voluntary muscular performance, often resulting in quadriplegia and aphonia [25]. It is anticipated that the ageing population, which increases the prevalence of chronic health problems, would also increase the number of people with neurological diseases that lead to paralysis. Individual costs for patients with paralysis might surpass 1 million dollars in the first year following injury, placing an enormous burden on the patient, their family and public health resources [26].

The conventional rehabilitation procedure used to treat these disorders is physical therapy. However, for 40% of stroke subjects, and most SCI subjects, therapies have not been successful in effectively reversing the motor deficits [27], [28]. Thus, there is a need to develop neurorehabilitation research to enhance the mobility and independence of paralyzed individuals.

Currently, communication strategies rely on eye movements that are followed by a camera, enabling the selection of items on a computer screen ("eye tracker") [28]. In the most severe cases, patients may lose all voluntary muscle control, including the ability to move their eyes, and they may become entirely immobilized, unable to communicate with or express any intent to the outside world. Therefore, it is important to improve new rehabilitation strategies that effectively restore patients' motor functions.

Intra-cortical electrodes have been investigated for brain machine interfaces (BMI) due to their capacity for establishing direct contact in real-time between a neuronal population and the implanted device [29]. The closeness to the neuronal signals allows the quick translation of accurately detected signals from multiple neurons into complex instructions. BMI provide a non-muscular channel between the CNS and external devices [30]. The input information in BMI systems can come from artificial sensors or can come from the neuronal tissues themselves, in the form of electrical activity. BMI system performance depends greatly on the quality of neural signals acquired. After being obtained, the signal is decoded by a computer processor and then used to carry out a specific operation. The output complexity depends on the neural signal in terms of accuracy and time of acquisition [31].

Intracortical brain-machine interfaces (iBMI) have been exploring applications such as the use of robotic neuro-prostheses and other effectors in humans [32] and the decoding of speech in real-time [33]. In humans, the first clinical trial with intracortical electrodes was in 2004 with Utah electrodes (developed by Cyberkinets) in patients with tetraplegia due to C3 spinal cord injury. Braingate is now responsible for further clinical studies in BMIs with Utah arrays [34]. According to their preliminary investigations, patients with functional CNS deficits that never entirely lose their ability to move are promising candidates for iBMI applications. Over the years, Utah electrodes have been successfully explored by Braingate for handwriting applications [35], cursor communication [36] and hand movement [37]. Until now, the Utah electrode array remains the only penetrating electrode approved for neural activity recording on timescales smaller than 30 days [34]. **Figure 4** shows a schematic representation of an iBMI application.

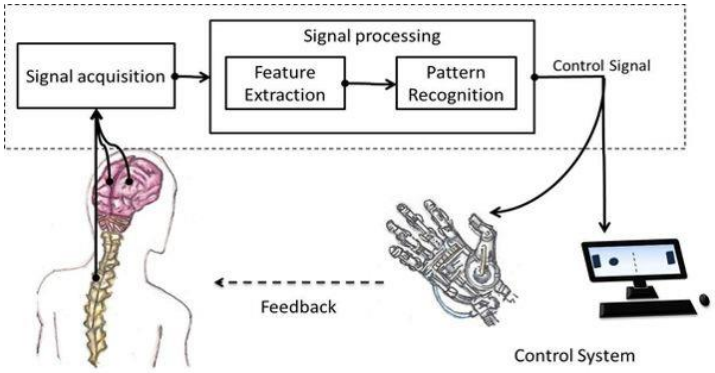

Figure 4 **-** Neural signals are acquired from intracortical electrodes and processed through signal processing to execute tasks, such as controlling robotic neuro-prostheses or decoding speech in real-time [38].

In the most recent research, recorded electrical activity has been used to bypass lesion sites and electrically stimulate muscle nerves through signals obtained by intracortical electrodes. For example, in a person with hand paralysis, neural activity restored grasping activity [37], [39]. Restoring leg muscle movement in animals [40], and humans [25] has also been achieved through spinal cord stimulation. Thus, the iBMI holds great promise for increasing the autonomy of debilitated patients. Additionally, the chronic use of iBMI platforms could permanently restore communication or movement of paralysed patients, which would significantly improve their quality of life. Nevertheless, chronic implantation often behaves poorly because neural activity recording is hampered by glial sheet formation, as well as neuronal death [18], [41].

1.2.2. Deep Brain Stimulation- Electrodes

The basic principle of DBS involves the stimulation of specific brain regions through chronic low electric fields to modulate dysfunctional neurophysiological signals. DBS electrodes are commonly introduced in the brain's subcortical nuclei or fibber bundles through stereotactic surgy [42]. As shown in **Figure 5**, clinically used DBS components include an internal system composed of a lead, an extension cable and an implantable neurostimulator responsible for generating electrical pulses. It also has an external system, that includes the clinician programmer, the patient programmer, and a recharger for rechargeable devices [43].

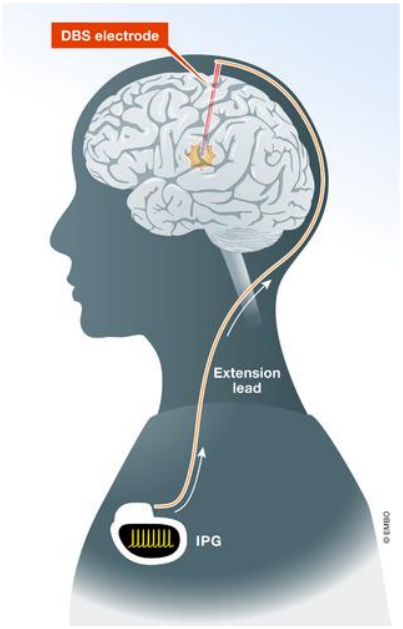

Figure 5 - DBS system used for clinical applications. The extension lead connects the brain electrode to the neurostimulator (internal pulse generator, IPG), the implanted power source. Reprinted from [42], under the terms of the CC BY 4.0 license.

Typically, DBS lead consists of an electrode array, with about 1.3 mm thick and 7.5–10.5 mm long, with four stimulating electrode contacts of 1.5 mm in length, separated by 0.5 or 1.5 mm [44]. The lead is inserted into a specific brain target and connected through an extension cable to the neurostimulator, which is commonly implanted in the anterior chest or abdomen.

DBS electrodes' performance is highly influenced by their materials. At the moment, commercialized DBS electrodes are made of platinum-iridium wires and nickel alloy connectors encased in a polyurethane sheath. Platinum-iridium was selected due to its low toxicity and outstanding conduction qualities. Additionally, the electrode's iridium component gives it a useful and practical rigidity [43]. There are various active stimulating contacts available in terms of electrode configurations, as shown in ***Figure 5***. Such configuration allows the electric stimulation to be shaped along the z-axis, through the combinations of anodes and cathodes, depending on the condition that has to be treated. DBS devices work by setting constant stimulation parameters between visits to the physician, typically set as 100Hz [45]. (**Figure 2B**)

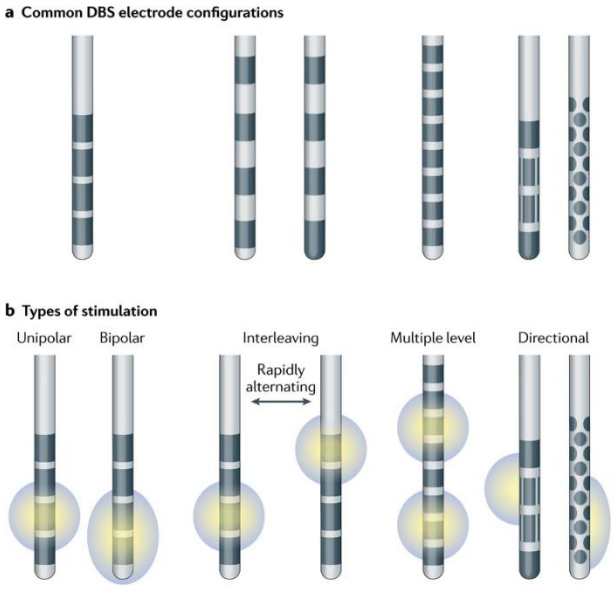

Figure 6 - DBS electrode configurations. a) Common electrode configurations for deep brain stimulation (DBS). Dark grey regions illustrate electrode contacts, which can be activated to deliver current. b) Modes of stimulation, depending on the type of DBS system in use. Unipolar stimulation refers to the current being directed from the battery to the contact or vice versa. Bipolar stimulation indicates the current flowing between electrode contacts, with at least one functioning as an anode and one as a cathode. Interleaving stimulation refers to the alternation of different stimulation settings. Multiple level stimulation enables multiple neural targets to be stimulated, provided that they lie along the electrode trajectory. With directional stimulation, the current can be directed or 'shaped' based on local anatomy or clinical symptoms. Reproduced with permission from [17]. Copyright © 2020, Springer Nature Limited.

1.2.2.1. Deep Brain Stimulation Applications

DBS is a neurosurgical procedure that has received FDA and CE approval for therapeutic usage due to its high safety profile, therapeutic efficacy, instantaneous effect, reversible and adjustable nature in several studies and clinical trials, without permanently harming neuronal tissue [46]. To date, is estimated that over 200.000 patients have been implanted with DBS devices [47]. Besides, the recent hypothesis that DBS may have neuroprotective effects presents new possibilities for neurological implants [48].

DBS is standard of care for patients with advanced Parkinson disease (PD) [49], essential tremor (ET) [50], dystonia [51] and Tourette syndrome (TS) [52]. Moreover, it has also been explored for non-motor diseases such as pain syndromes, neuropsychiatric disorders, epilepsy as well as other treatment-resistant conditions, including depression, Alzheimer's disease, addiction, anorexia nervosa and schizophrenia [52].

The great majority of DBS treatments are carried out for PD [53]. Parkinson's disease (PD) is the second most prominent neurodegenerative disease after Alzheimer's disease. In 2016, PD affected more than 6 million people, and by 2030, the number of individuals with Parkinson's disease is estimated to grow by more than 50% [54], [55]. PD is a progressive condition leading to gradually disabling both motor and non-motor symptoms. The main pathological manifestation is the loss of dopaminergic neurons in the substantia nigra, leading to bradykinesia, muscular rigidity and resting tremors [56]. In the early stages of the disease, PD treatment involves dopaminergic medication, such as levodopa, which the brain converts into dopamine [57]. However, for advanced stages of the disease, medication alone cannot control the symptoms leading to medication-related motor problems such as levodopa-induced dyskinesias and motor fluctuations. Neurostimulation has become an established treatment approved by the FDA in 2002 for an advanced stage of PD [57]. DBS is mainly indicated for patients with

levodopa-responsive symptoms [58], [59]. Patients with severe cognitive abnormalities, and pronounced gait and balance disorders do poorly after DBS surgery and are not considered for surgery [60]. Among neurostimulation targets, the subthalamic nucleus (STN) or globus pallidus interna (GPi) has been demonstrated to improve motor function for up to 10 years [61]. However, its effectiveness in treating non-motor symptoms is less clear [62]. Thus, while motor problems may still be resolved, the non-motor symptoms deteriorate and the patient may have cognitive declines, dysarthria and difficulty walking [58].

Despite the success of DBS surgery, there are still some limitations to overcome. For instance, DBS treatment is unable to effectively treat various symptoms. Thus, it is required to find more suitable targets, increase the precision of implantation, and software upgrades for noticeable improvements in BDS technology [63]. Additionally, the stiffness of the materials used to fabricate DBS electrodes, as well as the high dimensions of the probe's size, aggravates the neuroinflammatory reaction and tissue damage prompted by the wound healing process [64]. Nevertheless, the overall experience to date confirms that long-term DBS is relatively safe [17]. Even though the extent of the patient's benefit tends to decrease over time, long-term implantations of STN-DBS for PD (up to 10 years) have shown the safety and effectiveness of the therapy. [62].

1.3. Market Size for Neural Engineering

Globally, neurological disorders are the second-leading cause of death and the primary cause of disability, representing a major health concern [65]. Due to the limited available clinical options, effective therapies need to be addressed [66]. The burden of neurological diseases continues to rise due to population growth and ageing since the majority of neurologic disorders severely increase with age [65]. New treatment strategies are required for improving the quality of life of patients with neurologic disorders.

There are numerous opportunities to enhance the effectiveness, functionality, and efficiency of neural devices. Neural technology has already proved to benefit people with neuronal disabling medical conditions [53]. It has been anticipated that the global market for neurotechnology will grow from 9,3 billion dollars in 2020 to 21,9 billion dollars by 2026, with a 15.3% growth during the forecast period [67].

The deep brain stimulation market alone was valued at 1.05 million dollars in 2021, worldwide, and is projected to grow annually by 9.8% until 2030 [68]. Regarding BMI technology, the market size was evaluated in 2021 at 1.52 billion dollars and is expected to grow 17,16% until 2030 [69].

Chapter 2

Brain-Electrode Interface

This section will comprise an overview of the main cascade of biochemical and cellular events that follow the chronic implantation of electrodes, with an emphasis on biotic reactions. An overview of the current strategies being pursued to overcome FBR and promote electrode integration are outlined, with a focus on biomimetic coatings-based approaches.

2.1. Challenges Interfacing the CNS

While implantable devices proved to be a powerful tool to record neural activity and stimulate brain tissue, one significant issue for neural interfaces is the maintenance of long-term function [17]. The use of iBMI and DBS in long-term treatments has already proven to be advantageous for their clinical applications, however, over time, the neural recorded signal stability tends to decline, restricting electrode quality recording [70]. According to a study, 90% of Utah arrays implanted in the CNS of non-human primates failed over a 6-year period, with the majority of failure within a year of implantation [71].

The complexity of achieving long-term stimulation/recording of neural signals can be divided into two factors. The **biotic factors**, which include disruption of the BBB, the recruitment of microglia and macrophages to the implant site and the beginning of astrogliosis [72]; and **the abiotic factors**, which are associated with the electrode surface structural changes that impact the inherent properties of the electrode after exposure to extracellular fluids and molecules (damage of insulation coatings, direct mechanical damage, oxidation/reaction, and corrosion [20]). Since biotic and abiotic elements occur simultaneously and interact in various ways during the lifetime of the electrode, they cannot be separated into two distinct processes, and further studies are required to understand the complexity of their relationship [73].

2.1.1. Immune response to electrode-like implants in the brain

The chronic implantation of electrodes leads to continuous interaction between the electronic devices and the living neural tissue, which triggers a cascade of biochemical alterations and chemical reactions which may result in a Foreign Body Reaction (FBR), which is thought to be one of the main causes of poor signal and chronic recording failure. Understanding the neural tissue response to device implantation is a key point for improving the body's response and developing strategies to mitigate signal degradation.

The FBR process can be divided into two phases. The **acute phase** begins immediately after implantation and is characterized by an inflammatory response, followed by a **chronic phase** characterized by a transition from solely inflammatory to a fibrotic process.

2.1.1.1. Cells involved in the brain tissue response

There are different cell populations involved in the wound healing response to implanted materials in the CNS. Neurons and glial cells are the two main cell types found in nervous tissue. **Neurons** are the CNS's functional units and are special in their capacity to transfer and store information. The position of the neuron soma and its cellular processes relative to the electrode recording sites is determinant for the acquisition of a stable and viable signal for neuro-prosthetics and neurostimulation systems over long-term recording [74].

While neuronal populations are responsible for information processing and body function control, they are outnumbered by glial cells, which include oligodendrocytes, astrocytes, microglia cells, and other specialized cells. Microglia and astrocytes are the main cell types involved in the neuroinflammatory response in the CNS. **Microglia** act as cytotoxic cells that destroy pathogenic organisms while also acting as phagocytes that produce proteolytic enzymes to eliminate cellular waste and damaged extracellular matrix either during health or in response to injury [87]. Until a stimulus, such injury process, microglia are in an inactive or "ramified" state, acting as immunologic surveillance. Once activated, they start to multiply and change their shape into a more compact form, an "amoeboid" state [92]. Activated microglia express an elevated level of IBA-1 (ionized calcium-binding adapter molecule 1), an intracellular protein related to the reorganization of the microglial cytoskeleton which can be used in immunohistochemical staining to identify activated microglia in tissue [75].

Astrocytes are a dominant type of macroglia that support neurons in the CNS characterized by a star-like morphology and multiple projections with different functions in CNS health. These functions include the maintenance of the CNS homeostasis, control and support of neurons, neurotransmitter recycling and control/degradation of neuron synapses [76]. They also have an important role in the biochemical support of endothelial cells that form the BBB. After tissue injury, astrocytes become activated and undergo phenotype alteration to a “reactive” stage characterized by migration, proliferation, hypertrophy, and upregulation of glial fibrillary acid protein (GFAP), the main component of astrocyte cytoplasmic intermediate filament [77]. The stage of “reactive gliosis”, which refers to the activation, hypertrophy, and proliferation of astrocytes in response to injury is commonly assessed by immunostaining for GFAP [78].

In the CNS, **oligodendrocytes** are responsible for the assembly of myelin, a multi-layered sheath of membrane, that surrounds axonal segments promoting rapid conduction of action potentials down axons [79].

2.1.1.2. Brain tissue response to electrode implantation on acute and chronic timescales

Due to the dense and often highly vascularized neural tissue, the initial mechanical insertion of the electrode into the brain is a violent process that injures the surrounding brain tissue [20]. For example, mechanical stress leads to axonal morphological changes and neuronal membrane rupture suggesting neuronal damage [64].

Disruption of the blood-brain barrier (BBB) is an inevitable event during device implantation, which will reduce blood flow and oxygen supply [80]. Additionally, the adsorption of extravasated serum proteins onto the implant surface and the infiltration of neutrophils and monocytes, trigger the activation of inflammatory pathways of neighbouring glial cells including resident microglia and astrocytes [80]. The initial BBB damage upon implantation has been demonstrated to endure and cause chronic BBB leaking over time, which in turn has a negative impact on electrode function [81].

Nearby **microglia activation** is characterized by the extent of their process towards the electrode surface. As seen in **Figure 7**, after approximately 12 h, microglia progress to a motile stage and move their cell bodies to the injury site. At this stage, resident macrophages help microglia surround the implantation site and together, carry out their neuroprotective functions [82]. They act as main responsible for neuroinflammatory response, secreting pro-inflammatory cytokines and chemokines such as interleukins IL-1α, IL-1β, IL-6, tumour necrosis factor (TNF-α), monocyte chemoattractant protein 1 (MCP-1), reactive oxygen species (ROS) and reactive nitrogen species (RNS), leading to immune cell recruitment and additional cytokine production [64]. Both microglia and macrophages are accountable for recognizing released serum proteins and participating in the removal of cellular debris.

Oligodendrocytes are highly sensitive to oxidative stress by ROS and RNS as well as excitotoxic damage by glutamate over signalling. Depending on the severity of the inflammation reaction, oligodendrocyte

apoptosis causes demyelination and may cause neuronal death [64]. Additionally, *in vivo* studies have shown that the nearby adult brain's oligodendrocyte precursor cells (also called NG2-glia) are activated by pro-inflammatory environments, causing them to migrate and differentiate into astrocytes that will further contribute to the formation of the glial scar [83].

As it is shown in **Figure 7**, by one week after implantation, the density of microglia around the implant has significantly increased, while astrocytes start to move to the implant's surrounding tissue.

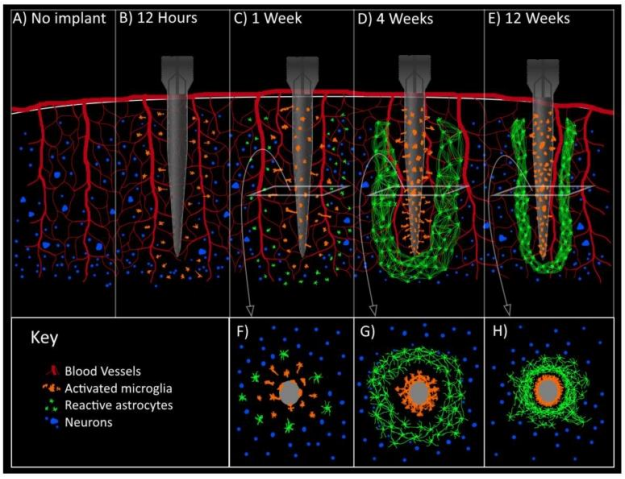

Figure 7 **-** Illustration of the glial encapsulation response (A) before implantation, (B) 12 h post-implantation, (C) 1-week post-implantation, (D) 4 weeks post-implantation, and (E) 12 weeks post-implantation. Panels (F), (G), and (H) represent cross-sectional views of (C), (D), and (E), respectively. Reprinted from [11], under a creative commons attribution (CC BY).

If microglia and macrophages were able to successfully remove the implant during this acute phase of FBR, the glial activation and neuronal degeneration would be minimal. However, being unable to degrade and phagocytose the implant, the inflammatory response persists with activated microglia/macrophages in the vicinity of the implants over chronic implantations [84],[85]. Neural progenitor cells have exhibited tissue regeneration and neuronal repopulation in implants that progressively dissolve. It's interesting to note that while these cells are present in the vicinity of rigid microwires, they do not repopulate the injured area with neurons [86]. These results indicate that the presence of a device may be responsible for the perpetuation of reactive tissue response, and implant removal contributes to the minimization of the pro-inflammatory process as well as tissue regeneration.

Surrounding the inflammatory core, a dense layer of **astrocytes** and plasma-extravasated fibroblasts starts to develop, which gradually turns into a barrier between the implant and the host tissue into which was implanted. This phase corresponds to the transition from an inflammatory to a fibrotic stage specific to the chronic phase of FBR and may take over 6 weeks to occur. Astrocytes are activated by IL-1β, TNF-α and complement component 1q (C1q) produced by microglia, losing their ability to promote neural health and, in turn, start stimulating neurons and oligodendrocytes death [87]. Since most of the tissue of the glial scar is formed by astrocytes, they are used commonly used as an index for neuronal damage and to evaluate gliosis extent.

As seen in **Figure 7**, at four weeks, cell architecture suggests the formation of a **glial scar** characterized by an inner microglia core in contact with the implant and a shell of surrounding astrocytes. The microglia seem to organize themselves into a more compact arrangement around the electrode, while astrocytes increase their density. At 12 weeks, the layers seem to be more compact and localized with less ED1 and GFAP reactivity outside these layers [11]. This period of time seems to correspond to the

proximity peak of the GFAP intensity to the implant site, indicating the contraction of reactive astrocytes over time [88]. It only takes weeks after implantation, for FBR gradually changes into its chronic fibrotic stage. Nevertheless, chronic inflammation and astrogliosis will remain indefinitely active until implant removal, usually in a steady state.

Inflammatory environment and reactive gliosis of FBR have been well described as a cause of **neuronal loss** (40%-60% in most studies) in the surrounding area of electrodes [89]–[91]. The decreased number of NeuN-stained neuronal cell bodies in the vicinity of the electrode indicates the death of the neuronal population. As electrode contacts must remain close to active neurons that are integrated into the functional neural network for proper transmission and reception of electrical signals, neural death contributes to device failure [91].

The glial layer formed is hypothesized to play a beneficial role in limiting the microglia-secreted factors to the surrounding tissue, as well as eliminating the stress shield caused by the stiffness of the electrode. However, fibrotic encapsulation not only compromises the electrical performance of the electrode, as it works as an **electrical insulator** tissue but also increases the distance between electrodes and viable neurons, which can seriously compromise the electrochemical performance of the electrode, since as previously mentioned, neurons must be present near the electrode site for neuronal stimulation/recording [88]. In the case of DBS, after glial scar formation, the volume of neurons stimulated commonly decreases by 50%. This effect leads to the need to increase current settings for a therapeutic effect, which can result in tissue damage through electrochemical reactions or physiological changes [92].

2.2. Strategies to improve electrode biocompatibility and long-term performance

To enhance the performance of implantable neural electrodes in the long term, it is essential to reduce the FBR. In this sense, in the last decade, efforts have been made to improve biocompatibility through the design of new neural interfaces. However, the challenge of obtaining a chronically reliable technology remains. In this section, an overview of strategies applied to improve neural interfaces is presented.

2.2.1. Electrode Geometry optimization

Electrode geometrical factors such as size, shape and design affect the brain tissue response. Smaller implants result in less brain tissue disruption, lower neuronal loss at the electrode/brain interface, and decreased chronic tissue responses [93]. As such, the field of chronically implantable electrodes is progressing toward the use of smaller and thinner electrodes.

In fact, the effects of commercially available intracortical electrode designs were studied at acute (3 days) and chronic (12 weeks) time points [94]. Electrode designs vary in terms of size (15 µm, 50 µm, 75 µm), shape (cylindrical or planar), and untethering/ tethering (anchoring an electrode in brain tissue) (**Figure 8**). In comparison to cylindrical electrodes with a 75 m thickness and planar electrodes with a 15 µm thickness, histological results showed that planar electrodes with 50 µm thickness and planar tethered electrodes resulted in greater glial scarring and less neuronal survival in regions of the blood-brain barrier (BBB) breach. This was true for both the acute and chronic responses [94].

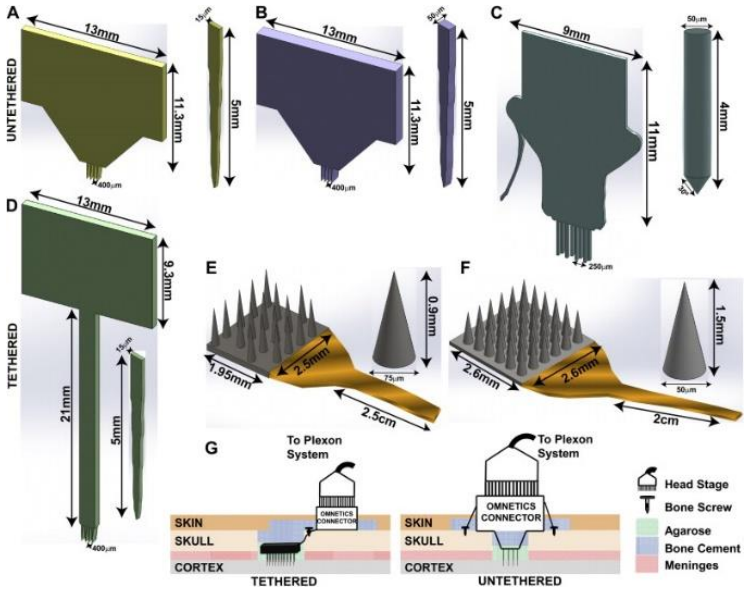

Figure 8 **-** Electrode design space of untethered and tethered electrodes. Overall dimensions of untethered Michigan 15 µm (M15), Michigan 50 µm (M50), and microwire (MW) electrodes are presented in figure panels A, B, & C; and tethered Michigan (MT), floating microwire array (FMA), and Utah array electrodes are presented in figure panels D, E, & F respectively. Individual shank geometry and dimensions are presented alongside electrodes. Electrode insertion and headcapping of tethered and untethered electrodes is depicted in figure panel G. Note that schematics are not to scale. Reprinted with permission from [94]. Copyright © 2013, Elsevier.

2.2.2. Electrode Stiffness modification

Mechanical Properties, particularly stiffness, are one of the most crucial parameters affecting electrode biocompatibility. Materials used for brain implants and the surrounding tissue have a mechanical mismatch in different orders of magnitude. While electrodes are composed of extraordinarily stiff materials like silicon or platinum, with shear moduli of 50GPa and 61GPa, respectively, brain tissue has a shear young modulus of about 1 kPa [95]. Although electrode high stiffness makes implantation into the cortical cortex easier, several researchers have demonstrated that the mechanical mismatch between the brain and microelectrodes prevents cells from pulling and stretching the electrodes as they would in normal brain tissue, activating the inflammatory response [96]. Besides, micromotion and interfacial friction because of breathing and movement may also cause a persistent inflammatory response [97]. Strategies for enhancing electrode integration by reducing trauma and inflammatory response include using flexible and mechanically-matched electrodes that endure less micromotion [98].

Most electrodes have an insulating layer deposited on their surface to protect them from unintended electrical signals. As such, insulating layers based on materials that have mechanical properties similar to those of the brain are highly desirable [99].

Polymers such as parylene-c, polyimide, Teflon and SU-8 are frequently employed to enhance the mechanical compliance of intracortical microelectrodes since they can attain a substantially lower Young's modulus than metals and can introduce stretchability into the material [20], [100]. However, even with softer polymers, an orders-of-magnitude disparity is found (E~1MPa to 1Ga) [95]. When compared with other polymers, parylene-c has enormous advantages, such as pinhole-free conformality, low water absorption, and high flexibility and mechanical strength (Young's modulus ~4 GPa) [101]. This polymer is a United States Pharmacopeia Class VI polymer with a long history of use in medical implants for its desirable properties, such as biocompatibility. Sohal et al. compared the FBR elicited by the implantation of a flexible, parylene-c sinusoidal microelectrode array (MEA) with a nonflexible Teflon-insulated tungsten microwire control in the brains of white rabbits. Results showed for parylene-c implants lower FBR and higher neuronal density at the implantation site over 26 to 96

weeks [102]. In another study, an ultrasoft MEAs with Young's moduli smaller than 1 MPa was designed and implanted in a rodent brain after 1 and 8 weeks and compared with a tungsten intracortical electrode. Successful integration of the soft MEAs was shown by immunohistochemical examination, which also showed no drop in neural density and reduced gliosis [103]. According to numerous studies, it is advantageous for electrode biocompatibility to use softer and flexible materials that resemble the brain tissue Young's modulus.

Practically, however, the process of implanting softer, more flexible and thin intracortical electrodes into the brain becomes more challenging than rigid electrodes [104]. One common strategy is to modify the mechanical properties of electrodes so that they are stiffer before implantation to enable insertion but become compliant after implantation. Nguyen and colleagues developed temporarily stiffen probes presenting a resorbable coating to prevent the buckling of parylene-c thin flexible electrodes. Upon coating resorption, the initially stiff probe becomes flexible. The resulting FBR was shown to be minimal, with improvements in neuronal health after 4 months [105].

Additionally, instead of altering the mechanical properties of the entire electrode, soft, flexible hydrogel coatings have been explored to attain a conductive and mechanically-compliant electrode/brain tissue interface of neural electrodes, [106]. Hydrogels are cross-linked networks of hydrophilic polymeric chains, which can be engineered to mimic the mechanical and chemical properties of biological tissues. Besides, their high water content offers an ionic physiological environment [107]. In fact, hydrogel coatings with matching microstructural and mechanical properties of the brain tissue have been shown to reduce micromotion and adverse biological responses [108].

Hydrogels made of alginate [109], poly(ethylene glycol) (PEG) [110, 111] and poly(vinyl alcohol) (PVA) [112] have been used to reduce FRB and neuronal loss. Spencer et al, investigated the capacity of thick (25–100 µm) polyethylene glycol dimethacrylate (PEG-DMA) hydrogel coatings, with mechanical properties close to that of brain tissue (E ~11,6 kPa) to attenuate acute and chronic *in vivo* responses. These coatings were tested in a rodent cranial implantation model, and the results confirmed hydrogel's ability to reduce strain caused by micromotion, as well as, glial scar formation compared to a harder material, un-coated glass devices [113]. Therefore, hydrogel coatings may offer an effective mean of mimicking brain tissue mechanical properties, enhancing the functionality and biocompatibility of penetrating electrodes.

2.2.3. Surface Modification

Surface chemistry and topography have a significant impact on the overall response of brain tissue to implantable microelectrodes, from early protein adsorption events to the ability of neuronal cells to adhere to the electrode surface and survive, as well as interactions with glial cells [99].

2.2.3.1. Biomimetic Coatings

One approach to improve the integration of implantable electrodes within the brain tissue is by decorating their surface with cell adhesive proteins/motifs present in the brain extracellular matrix (ECM). ECM-based coatings is one of the simplest and most common approaches to promote neuronal regeneration, growth and other functions [114]. ECM serves as the scaffold for cell adhesion, facilitates intercellular communication and plays an important role in many cellular behaviours, such as cell growth and cell movement [115]. The incorporation of ECM components, such as laminin (LN) [116] and L1 [117], on electrode coatings, have been shown to contribute to better electrode integration into the neural tissue.

LN is among the most important ECM proteins explored for neural applications [118]. LN is a highly expressed protein in the cerebrovascular basal lamina, capable of mediating neuronal cell adhesion, migration, neurite extension, axonal pathfinding, and synapse formation [118]. Laminins are a family of large heterotrimeric glycoproteins composed of three polypeptides subunits, five alpha (α), three beta

(β) and three gamma (ϒ) subunits, which assemble into cross-shaped molecules. (**Figure 9A**) Laminin isoforms are composed of three short arms and a triple helical coiled-coil domain (long arm), formed by the combination of α, β and ϒ subunits [119].

LN bioactivity results from its multiple bioactive domains and their exposure. The globular domains located at the N-terminus of the three LN short arms are responsible for mediating LN polymerization into a polygonal LN network [119]. The process of laminin polymerization contributes to correctly orientating the globular domains at the C-terminus of the LN long arm, which in turn will be able to interact with cell surface receptors, including integrins [120], syndecans and dystroglycan [121], bind to growth factors [122] and other ECM proteins [123], [124]. (**Figure 9B**)

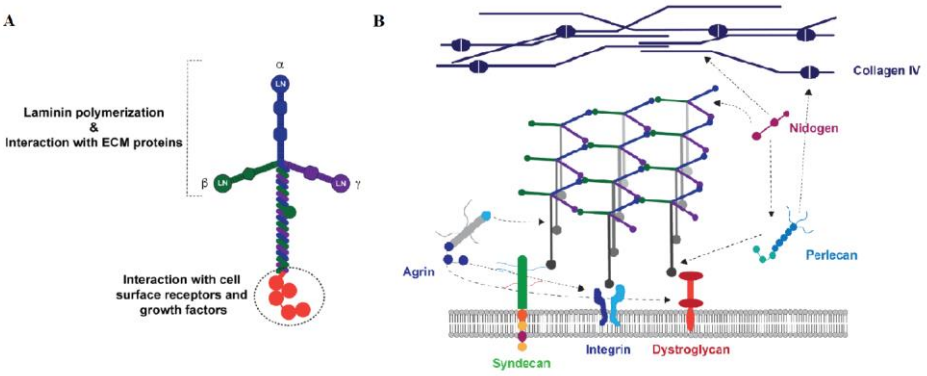

Figure 9 **-** Schematic representation of laminin's structure and main biological functions. (A) Representative model of laminin structure and domain architecture. The three, and polypeptidic domains composing laminin are presented in blue, green and purple, respectively. (B) Schematic representation of the supramolecular assembly of the basal membrane, in which laminin interacts with other ECM proteins and several cell receptors. Adapted with permission from [119]. Copyright © 2020, American Chemical Society.

The incorporation of two LN peptides (CDPGYIGSR and RNIAEIIKDI) into conductive poly-pyrrole coatings promoted neuronal density and neurite outgrowth, while significantly reducing astrocyte adhesion *in vitro*. Despite these promising results, no further *in vivo* tests were performed [125].

The *in vivo* performance of LN coatings was addressed in Bellamkonda's lab. In this study, intracortical silicon microelectrodes were coated with alternating layers of polyethyleneimine (PEI)and LN to create a PEI-LN multilayer nanoscale coating using an electrostatic layer-by-layer deposition. *In vitro*, the PEI-LN layer significantly enhanced cortical neuronal adhesion and neurite extension without compromising electrode impedance [126]. Subsequent intracortical implantation in a rat model revealed for PEI-LN coated electrodes a significant reduction of the glial scar (GFAP expression) 4 weeks post-implant, as compared to uncoated silicon probes. However, the coating did not have a significant impact on the neural density at the interface. This effect was associated with a higher number of activated microglia near the probe available for clearance of necrotic debris, one-day post-implant [116].

Noteworthy, in the biomimetic coatings reported in the literature, LN was immobilized without any control of LN orientation, through either non-specific adsorption or electrostatic binding, or by non-selective covalent immobilization using the multiple amine groups of LN.

In an attempt to assure the exposure of LN bioactive domains upon its immobilization, Barros and colleagues reported a high affinity-binding approach to immobilize LN through its agrin-binding domain, localized in the central region of the LN long arm, using the N-terminal domain of human agrin (NtA). When applied to model surfaces (self-assembled monolayers on gold), site-selective immobilized LN enhanced cell adhesion and spreading of human neural stem cells (hNSC) compared to non-specific covalently-bound LN, being this effect conditioned by NtA concentration [127]. When further explored

for the bio-functionalization of synthetic matrices, site-selective immobilized LN better supported the 3D culture of hNSC than gels with physically entrapped LN, namely proliferation, differentiation, and neurite extension [128]. Yet, the efficacy of site-specific conjugated LN to improve the integration of implantable neural electrodes is still to be addressed.

The main drawback of bioactive strategies based on full-length ECM proteins or peptides is their short-lived nature. It is known that over time, activated inflammatory cells phagocytose and eliminate both adherent and covalently immobilized proteins. Therefore, it is unclear if ECM proteins or peptides-based techniques will enhance long-term recording performance. However, as they are feasible to decrease initial wound healing and enhance tissue integration after implantation, this strategy might be used in combination to enhance the biocompatibility and functionality of microelectrodes [20]. Furthermore, ECM coating materials from other species, such as animals, present chemical and physical inherent differences from human ECM, which can result in unwanted immunological responses. This problem might be mitigated by using patient-derived ECM or alternatively, recombinant human ECM proteins [129].

2.2.3.2. Anti-fouling coatings

ECM-based coatings may enhance the number of neuronal cells surrounding the electrode, but they may also encourage the attachment of other cell types, such as astrocytes, which are a major component of glial tissue. As such, non-adhesion coatings have been explored to reduce non-specific protein adsorption to the neural interface, and hopefully contribute to preventing glial cells and inflammatory cells to adhere to the probes [99].

Due to their anti-fouling properties, poly(ethylene glycol) (PEG), an FDA-approved polymer, has become increasingly used to reduce protein adsorption and minimize non-specific cell adhesion. PEG is a hydrophilic, nondegradable polymer commonly used in biomedical applications due to its biocompatibility, nontoxicity, low immunogenicity, and water solubility [130].

Rao et al. investigated the effects of PEG-containing polyurethane (PU) hydrogel coatings on electrode behaviour *in vitro* and *in vivo*. PEG-PU hydrogel coating showed a reduction of 93% of protein adsorption compared to polydimethylsiloxane (PDMS) substrates [110]. Additionally, PEG-PU coating was able to achieve reduced gliosis and neural loss than PDMS substrates [110].

Particularly, Four-arm maleimide-terminated poly(ethylene glycol) (PEG-4MAL) has been investigated for neural applications due to its versatile design, which allows adapting biochemical and biophysical properties like the type and density of cell-adhesive ligands, mechanical and structural properties, and protease-dependent degradation [131], [132]. These characteristics make the use of PEG-4MAL-based matrices particularly desirable for interaction with brain tissue, namely, to enhance the biocompatibility of electrode surfaces. Garcia et colleagues have already used PEG-4MAL hydrogels conjugated with an anti-inflammatory factor to improve electrode performance. Results indicate promising findings for an engineered coating to increase neuronal survival and improve tissue response around implanted neural electrodes [133].

Additionally, the coating of silicon neural electrodes with a PEG- (N-isopropylacrylamide) (PEG-NIPAm) multi-layer hydrogel significantly reduced astrocytic recruitment compared to uncoated electrodes, after intracortical electrode implantation in rat brains. Still, the microglial response showed a persistent inflammation at the implantation site, and neuronal density was not improved [111]. Thus, the coating of electrodes with non-fouling materials *per se* seems to have limited success, underscoring the need for further improvements in implantable electrodes.

2.2.3.3. Anti-inflammatory drug delivery

Delivery of anti-inflammatory drugs or factors is another important strategy to enhance electrode integration, as these can “camouflage” the electrode from the immune system and enhance its

performance in the long term [90]. Boehler et al. explored the effect of dexamethasone (DEX) controlled release upon chronic implantation of a flexible neural microelectrode in the rat hippocampus. DEX was incorporated in the probe coating and was weekly released by electrical signals. After 12 weeks of implantation, results showed that both flexible probes had a small inflammatory response, whereas electrodes coated with DEX presented more neurons nearby the electrode than controls. [134]

The incorporation of antagonists of pro-inflammatory cytokines [135], has also been explored. For instance, LN-coated probes containing an antagonist of the IL-1 receptor (IL1-ra) were effective in reducing glial scaring around the electrode, after 4-weeks of implantation in rats [136].

2.2.3.4. Topography

Another characteristic that influences electrode biocompatibility is surface topography. Cell adhesion is intimately related to the topography of the exposed surface area of the electrode [137]. In one study, *Ereifej* et al. fabricated surfaces made of poly(methyl methacrylate) (PMMA) with varying groove widths (no grooves, 555 nm, or 277 nm). Both patterns had a depth of 200nm. When comparing all the surfaces, the 277 nm grooves nanopattern surface has been shown to elicit less astrocyte activation [138].

Chapman et al. also demonstrated the effect of nanostructured intracortical electrodes through the inclusion of nanoporous gold at the surface. Results showed a high neuron-to-astrocyte surface coverage ratio, as well as a reduced glial scar formation, that ultimately leads to the proximity of the neuron-electrode interface [139].

2.3. Summary and Motivation

The development of implants that can electrically stimulate or record neural activity in nervous tissue is expanding quickly as these tools have offered various therapeutic approaches to multiple neural disorders. However, chronic long-term recordings are constrained by the foreign body response, which happens during the wound healing process, characterized by a cascade of inflammatory events, which develops into glial scar formation, and, in turn, causes the implant to fail over long periods of time. While many strategies have been employed to improve long-term neural electrode functionality, the challenging issue of improving the long-term biocompatibility of chronically implanted neural electrodes is still persistent.

The underlying mechanism of FBR is still not fully understood, which hinders the establishment of the optimal strategy for a given application. To surpass these hurdles, biocompatible coatings have been commonly employed. Specifically, hydrogels have been explored as potential coatings for implanted electrodes as their mechanical properties can be tailored to mimic the brain tissue microenvironment. As fouling remains a key issue in FBR, the use of antifouling polymers for hydrogel coatings contributed to the reduction of protein absorption and non-specific adsorption. However, anti-fouling performance *per se* is not enough to surpass FBR.

Additionally, the introduction of bioactive factors on the surface of electrodes recapitulating the native neural *in vivo* environment is another strategy that has been pursued for enhancing electrode performance. Since synthetic hydrogels allow independent control over their biochemical and biophysical properties, these platforms constitute an attractive option for presenting bioactive factors to the brain tissue. Synthetic hydrogels have been commonly synthesised with reactive functional groups for further tethering the bioactive cues. Despite being widely used, one of the main limitations presented by these strategies is the inability to control the conformation and orientation of bioactive molecules upon immobilization.

Among the bioactive factor used for neural applications, ECM-based protein laminin stands out as a protein for neural applications due to its role in the modulation of neuronal behaviour, including cell adhesion and viability, and neuronal outgrowth and migration. However, only a few have addressed the performance of LN coating. Noteworthy, in all the biomimetic coatings reported, LN was immobilized without any control of LN orientation.

Given the situation, it is clear that further studies exploring the biological impact of site-specific conjugation of a bioactive factor on cortical cell behaviour in a modular anti-fouling synthetic hydrogel platform are of great interest. These studies can offer valuable insights for improving the long-term biocompatibility of chronically implanted neural electrodes, particularly concerning the use of biofunctionalized hydrogel systems as cell instructive 3D platforms for the culture of cortical neurons. This can eventually bring us closer to a clinical solution for FBR.

2.4. Research goals and Strategy

This thesis focuses on the challenging issue of **improving the long-term biocompatibility of chronically implanted neural electrodes**. To ensure the long-term efficacy of the electrode, effective methods are specifically required to reduce glial scar formation and neuronal loss at the electrode-brain interface.

The main goal of the work is to develop a **non-fouling hydrogel coating mechanically compliant with brain tissue,** recapitulating the native microenvironment of brain tissue. Specifically, we propose **to develop a hydrogel coating based on four-arm maleimide terminated poly(ethylene glycol) (PEG-4MAL), decorated with site-specific immobilized LN**, to better preserve LN bioactive epitopes upon immobilization. This hydrogel is predicted to offer cell instructive cues directing neurite outgrowth toward the surface of implantable neural electrodes, while preventing non-specific protein adsorption and cell adhesion, which contribute to glial scar formation.

To test this hypothesis, we propose a proof-of-principle study using parylene-C and polyurethane substrates, polymers commonly used to insulate intracortical and deep electrodes, respectively.

Specific objectives include:

✓ **Preparation and characterization of a PEG-4MAL hydrogel coating decorated with site-selective immobilized LN.**

✓ **Evaluation of the *in vitro* biological performance of the developed hydrogel coatings,** to unravel the ability of site-specific immobilized LN to mediate cell adhesion and axonal extension of cortical neurons.

Chapter 3

Materials and Methods

3.1. Substrates

3.1.1. Parylene-c coated silicon substrates

Single-side polished silicon samples (<100> orientation) with a 100 nm thick layer of thermal SiO_2 (average roughness: 0.1 nm), diced into 10×10 mm^2 and 5×5 mm^2 samples were provided by INESC-MN. The parylene-c insulation layer (2 µm thick) was deposited through chemical vapour deposition (CVD) by Para Tech Coating UK Ltd. To improve the adhesion of parylene-c to the SiO_2 surface, a silane adhesion promoter (Methacryloxypropyl trimethoxysilane, Silane A 174, Polyfix 100) was applied before parylene-c deposition.

Parylene surfaces were finally washed trice with isopropanol (Biochem Chemopharma; 5 min with agitation) and trice with water type II, dried under vacuum at 40 °C overnight, and stored in the desiccator until being used.

3.1.2. Polyurethane films (PU) preparation

Commercially available medical grade polyurethane, Pellethane 2363 80 AE (Lubrizol LifeSciences, Ohio, USA), was obtained in pellet form. The pellets were sonicated for 15 min twice with hexane (Merck), and once with 99% (v/v) ethanol to eliminate any trace of silicone remaining from the extrusion fabrication process. This step was repeated twice. Pellets were then left to dry overnight in the hood and another 24 h in a vacuum oven at room temperature (RT) for complete evaporation of the solvent.

PU films were first prepared by solvent casting. The pellets were dissolved overnight, under stirring, in analytical grade tetrahydrofuran (THF), at a final concentration of 7.5 % (w/v). The resultant solution was then casted into clean glass 140 mm Petri dishes (40 mL per Petri dish). These were covered with perforated aluminium foil and kept in a hood for 48 h at RT, to slowly vaporize the solvent. All the films were dried overnight under vacuum at 40 °C, to ensure complete solvent evaporation. PU films were then cut into 1×10 cm^2 pieces with a blade and washed in hexane, ethanol, and trice with type II water (5 min each under under sonication), to remove possible impurities resulting from the cutting process. PU films were finally dried under vacuum at 40 °C overnight and stored in a desiccator.

PU films were also obtained by spin coating, using a spin-coater (model WS-650-23, Laurell Technologies Corp., North Wales, PA, USA). The pellets were dissolved overnight, under stirring, in analytical grade tetrahydrofuran (THF), at a final concentration of 5 % (w/v). PU solution (100 µL) was applied to the centre of a 10 mm glass coverslip at different spin speeds (4500, 600 and 900 rpm) for three different periods of time (30, 45 and 60 seconds). However, in all of the following procedures, only PU films obtained by solvent casting were used.

3.2. Surface Activation

3.2.1. Parylene-c surfaces

Parylene-c surfaces were treated with oxygen plasma using a Diener Zepto (Model 2) at a fixed power (50 W) and pressure of (0,4 mbar). Parylene-c coated substrates were placed on a microscope glass slide, transferred to the plasma cleaner chamber, and then subjected to oxygen plasma, varying the exposure time (2, 3, 5, 10, 15 and 30 seconds). After oxygen plasma treatment, parylene surfaces were stored under an inert atmosphere and functionalized on the same day, shortly after plasma treatment.

3.2.2. PU films

PU films were activated with UV/ozone (UVO) plasma, using a UVO cleaner apparatus (model No.42-220, Jelight Company Inc) inside a fume hood. Films were placed on a microscope glass slide, transferred to the UVO chamber just below the UV light source and subjected to different UVO treatment times (50, 100, 200 and 300 seconds). The chamber was pre-run for five minutes before the first treatment to attain ozone gas and UV light power saturation in the chamber [140]. An air pump was kept running throughout the UVO treatment to keep the ozone saturation level constant. Activated PU surfaces were stored under an inert atmosphere and functionalized on the same day.

3.3. Surface functionalization with silane-PEG-maleimide

Pre-activated parylene-c and PU surfaces were functionalized with maleimide groups using silane-PEG-maleimide (silane-PEG-MAL). Briefly, the substrates were transferred to a 48 well-plate suspension culture plate (CELLSTAR®) and incubated with 5, 10 and 25 mg/mL of silane-PEG-maleimide (silane-PEG-MAL) (2 kDa, Nanosoftpolymers) in ethanol: water 95:5 (v/v) for 2 h at RT and 100 rpm, rinsed trice with 10 mM phosphate-buffered saline (PBS, pH=7.4) and stored under argon at -20 °C. As a control, substrates were also incubated with the same conditions referred to, but without silane-PEG-MAL.

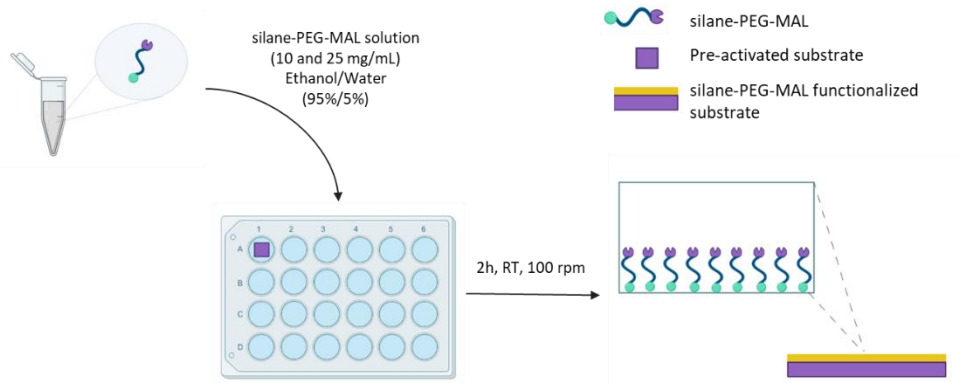

Figure 10 - Schematic representation of the surface functionalization of pre-activated parylene/PU surfaces with silane-PEG maleimide (silane-PEG-MAL) (not to scale).

3.4. Coating of parylene surfaces with a PEG-4MAL hydrogel decorated with site-selective immobilized laminin

Parylene-c surfaces were selected to test the deposition of a PEG-4MAL hydrogel decorated with site-specific immobilized laminin, due to time constraints.

3.4.1. Deposition of a PEG-4MAL-based hydrogel coating

Four-arm maleimide-end functionalized poly(ethylene glycol) (PEG) macromer (PEG-4MAL), was used as the hydrogel backbone, while PEG-dithiol was used as the cross-linker. PEG-4MAL (40 kDa, 98,6% purity, 96,7% end-group substitution, a polydispersity of 1.02, Jenkem Technology) was dissolved in 10 mM 4-(2-hydroxyethyl) piperazine-1-ethanesulfonic acid (HEPES) buffer in PBS (pH 6.5), to obtain a final polymer density of 10% (w/v). PEG-dithiol (3.5 kDa; 99.8% purity, Jenkem USA) was dissolved in 10 mM HEPES buffer (pH 6.5) at a concentration assuring a stoichiometrically balanced 1:1 maleimide/cysteine molar ratio.

Silane-PEG-MAL functionalized parylene surfaces were firstly immersed in PEG-dithiol solution for 2 min, to allow the covalent binding of the hydrogel precursor PEG-4MAL. Unreacted PEG-dithiol was removed immersing the substrates in HEPES buffer for 1 min. Then, the formation of the hydrogel coating was obtained by immersing sequentially the substrates in PEG-4MAL and PEG-dithiol (2 min

each incubation step) and repeating this sequence according to the number of treatments envisaged for each coating (each sequential immersion in PEG-MAL and the cross-linker is considered one treatment). Throughout this procedure, unreacted precursors were removed immersing the substrates in HEPES buffer for 1 min. Of note, in spite of sequential reactions, no layers are expected to be formed. Instead, a 3D hydrogel is created through the dynamic interplay of hydrogel precursors [133].

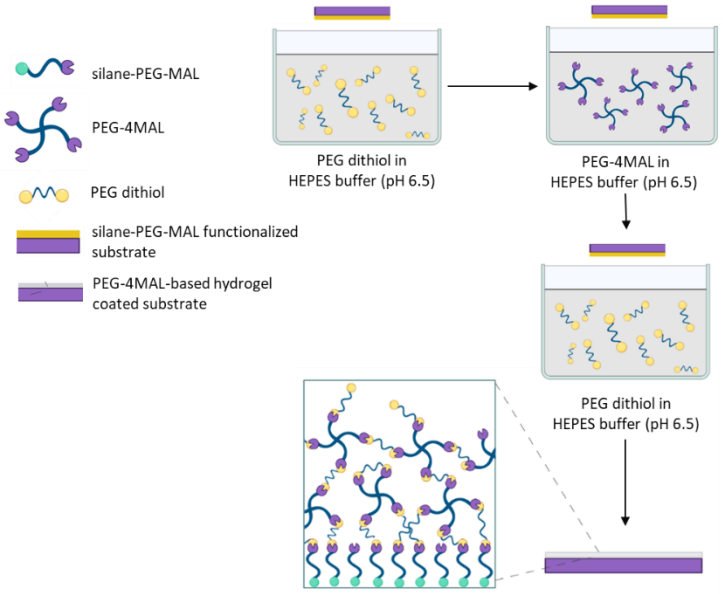

Figure 11 **-** Schematic representation of the deposition of a PEG-4MAL hydrogel coating on pre-activated parylene surfaces (not to scale). Silane-PEG-MAL functionalized parylene surfaces were firstly immersed in PEG-dithiol solution, to allow the covalent binding of the PEG-4MAL. The formation of the hydrogel coating was obtained by flipping the substrates and dipping them sequentially in PEG-4MAL and PEG-dithiol solutions. This sequence was repeated in order to attain the number of treatments envisaged (each sequential immersion in PEG-MAL and the cross-linker is considered one treatment).

3.4.2. Deposition of a PEG-4MAL-based hydrogel coating with decorated with site-specific immobilized laminin

The N-terminal domain of human agrin (NtA), localized in the central region of the LN long arm, was used to assure the exposure of LN bioactive domains upon its immobilization, *via* high-affinity binding [127]. NtA, produced and conjugated at its N-terminus with a thiol-terminated PEG according to Barros et al. [127], was used for LN immobilization onto PEG-4MAL. Thiol-ended PEGylated NtA was dissolved in 10 mM HEPES buffer in PBS (pH 6.5) at two different concentrations (5 and 10 µM).

The deposition of a PEG-4MAL hydrogel decorated with site-specific immobilized laminin (LN) was performed on parylene surfaces subjected to a single PEG-4MAL/PEG-dithiol treatment, as a proof-of-concept. After the first PEG-4MAL/PEG-dithiol treatment (see section 1.4.1.) substrates were immersed in PEG-4MAL solution (2 min) and then in the solution of thiol-ended PEGylated NtA for 15 minutes, to allow covalent binding to maleimide groups from PEG-4MAL through Michael-type addition. Substrates were subsequently incubated for 2 hours at 37 °C with laminin 111 from mouse Engelbreth-Holm-Swarm sarcoma basement membrane (Sigma-Aldrich) (20 µg/mL in 10 mM HEPES buffer in PBS pH 7.4), for LN high-affinity binding to the surface. Substrates were finally immersed for 1 min, twice, into 10 mM HEPES buffer (pH 7.4) for removal of unbound LN and stored in PBS (pH 7.4) at 4 °C.

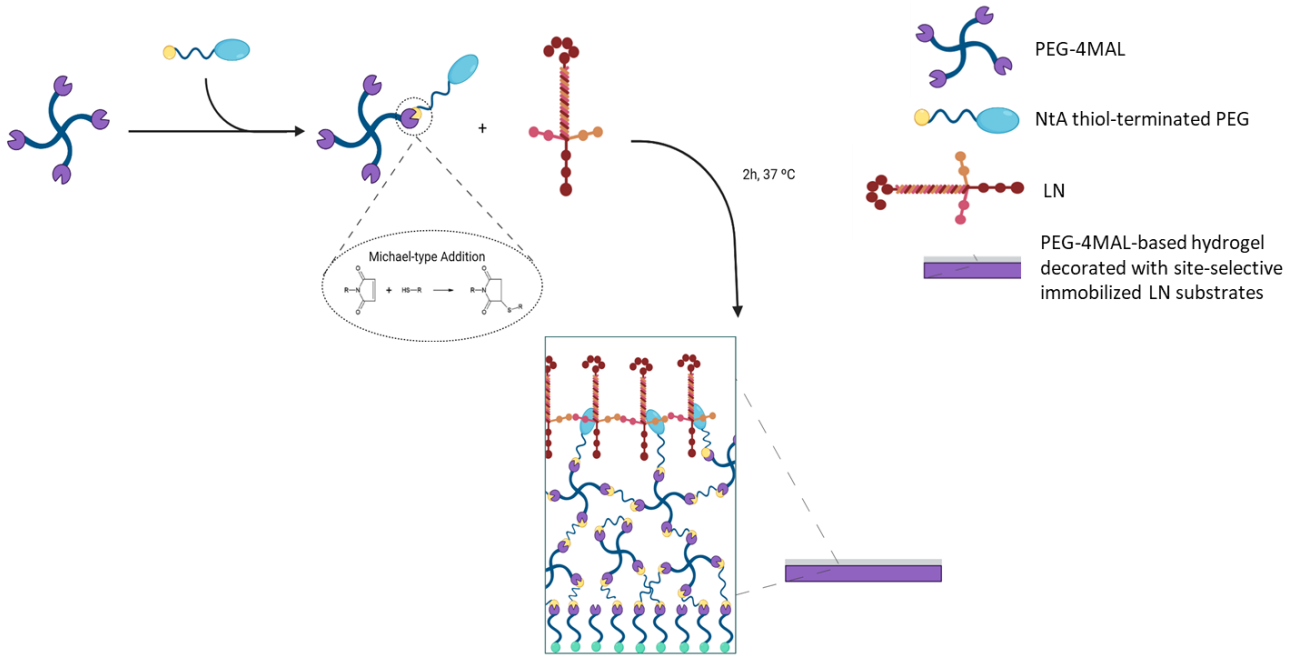

Figure 12 - Schematic representation of the formation of a PEG-4MAL-based hydrogel coating decorated with site-specific immobilized laminin (not to scale). After the first PEG-4MAL/PEG-dithiol treatment, substrates were immersed in PEG-4MAL solution and then in the solution of thiol-ended PEGylated NtA, which promotes high affinity binding of laminin. PEG-4MAL functionalization with thiol-ended PEGylated NtA will contribute to the exposure of LN bioactive domains upon its immobilization.

3.5. Surface characterization studies

3.5.1. Surface wettability

The water contact angle was determined using a contact angle measuring device from Data Physics, model OCA 15, equipped with an electronic syringe, a video CCD camera and SCA 20 software. Contact angle measurements were performed at RT (25 °C), using the captive bubble method, Briefly, the substrates were attached to glass slides with the surface of interest facing upwards, and the glass slides were placed upside down in a quartz chamber filled to the top with type II water. Then, 10 µL air bubbles were released from a J-shaped needle positioned underneath the substrate's surface. Images of the bubble profiles were immediately captured with the CCD camera, and the water contact angle was determined using the Young-Laplace fitting model. Water contact angles of parylene-c surfaces were measured immediately after surface plasma activation. In the case of PU films, measurements were carried out approximately 2 hours after plasma treatment. In each substrate, eight to ten random locations were analysed, and average contact angle values were reported.

3.5.2. Surface chemistry

3.5.2.1. X-ray photoelectron spectroscopy (XPS) analysis

Changes in the chemical composition of parylene/PU surfaces after modification (depth analysis between 5 and 10 nm) were examined through XPS analysis. XPS spectra were obtained on Kratos Axis Ultra HSA spectrometer, using an Al monochromator x-ray (Al- Kα 1486.6 eV) as the excitation source (15 kV), operated at 90 W. The analyser was run in the constant transmission mode. Emitted photoelectrons were evaluated, for all substrates, at a 20° take-off angle from the horizontal surface plane. Survey spectra were acquired with an energy binding range of 0 to 1350 eV, using a pass energy of 160 eV. High-resolution spectra for the C 1s, and O 1s regions were obtained using a pass energy of 40 eV.

Spectral analysis was performed using CasaXPS software (version 2.3.24), using the Gaussian/Lorentzian product function- GL(30) for spectra deconvolution and curve-fitting [141]. The background of the survey spectra was corrected using the Shirley method, and element atomic percentages were calculated from the integrated intensities of the XPS peaks, considering the atomic sensitivity factors of the instrument data system. Due to parylene-c and PU insulating nature, there is a build-up of positive charge at and near the substrate surface resulting in the electrons' emission, and leading to a shift toward higher binding energy [142]. Therefore, the binding energies of the high-resolution photoelectron peaks were calibrated, setting the binding energy of the aliphatic carbon (C-C) C 1s peak to 285.0 eV. A linear background was used for the C 1s spectrum, while an integral background based on the Shirley method was used for the O 1s spectra. Initial assumptions on the possible species were derived from polymers' stoichiometry and chemical bonds. Regarding the unmodified parylene-c surfaces, the deconvolution of the C1s spectrum was made according to the stoichiometry of the polymer (1 chlorine atom and 8 carbon[143]). Chlorine concentration normalized to carbon gives a value of 0.125, which was used to restrict the intensity area of the C-Cl component, assuring the proper concentration of chlorine in C 1s spectra. The deconvolution of plasma-treated parylene-c surfaces was also performed by applying some restrictions. First, the difference between the binding energies values of the C-Cl component and the C-C component as well as the difference between the aromatic component and the C-C peak obtained in the non-modified substrate was used to restrict the binding energies of the C-Cl component and aromatic component regarding the C-C component for plasma treated surfaces. The hydroxyl group's binding energy range was likewise constrained to a range between 286.3 and 286.7 eV. For all the conditions, components' FWHM values in C 1s spectra were fixed based on the FWHM value of the respective C-C component, except for the satellite component [144]. Concerning PU surfaces, components' FWHM values in C 1s were also fixed based on the FWHM value of the C-C component of each condition.

3.5.2.2. Fourier transformed infrared spectroscopy with attenuated total reflectance (FTIR-ATR)

Thermo Scientific's Nicolet 6700 Class 1 Laser Product was used to record ATR-FTIR spectra. Data were acquired at 4 cm^{-1} resolution with a total of 32 scans. Films were uniformly held up against a diamond tip using a Smart Omni Sampler during readings. Measurements were acquired in the mid-IR frequency range from 4000 to 400 cm–1 and treated using the Omnic software.

3.5.2.3. Measure Thiol Assay

Maleimide surface density after surface functionalization with silane-PEG-MAL was determined by measuring the amount of unreacted/free thiols after surface incubation with reduced glutathione (GSH), using a Fluorometric Thiol Quantitation Kit (Sigma-Aldrich). Briefly, silane-PEG-mal functionalized surfaces were incubated with a 160 µM GSH solution for 15 minutes at RT and under stirring at 100 rpm. The plate was protected from light during incubation. Serial dilutions of the thiol quantitation standard (reduced glutathione; 0-30 µM) were also prepared to generate a standard curve. Afterwards, 25 µL of the reacted GSH solutions substrates and the standard solutions were mixed with an equal volume of the thiol-detection reagent in the wells of a black-walled 384-well fluorescence plate, and the fluorescence read using a microplate plate reader (BioTek™Synergy™ Mx; $\lambda_{excitation}$/ $\lambda_{emission}$ of 490/535 nm). Unmodified surfaces were used as a blank, and their background fluorescence value was subtracted. The concentration of free thiols was inferred from the GSH standard curve, and the maleimide surface density was determined by taking into account the surface area.

3.6. Surface morphology

3.6.1. Atomic force microscopy (AFM)

AFM analysis was performed in Contact mode at RT. V-shaped cantilevers with triangular silicon tips were used. Images of unmodified surfaces, plasma-treated surfaces, and surfaces functionalized with silane-PEG-MAL, were acquired in air using a cantilever tip (Hydra-All-G, AppNano, USA) with a spring constant (k) of 0.085 N/m. AFM images of plasma-treated surfaces were captured 30 to 60 min after plasma treatment after applying an argon current on the surface. Scan speeds were set between 0.8 – 2.0 lines/s. Hydrogel-coated surfaces were imaged in PBS (pH 7.4), using an MLCT-BIO-DC cantilever tip (Bruker, USA) with a spring constant of 0.03 N/m, and scan speeds set between 0.5 – 1.0 lines/s. PicoView 1.2 software was used for image acquisition, while the Ws×M5.0 software was used to determine surface roughness using the following height parameters: average roughness (R_a, the arithmetic average of the deviations from the center x–y plane), root-mean-square of the deviations from the center x–y plane (R_q), and average maximum roughness (R_z, the difference in height between the average of five highest peaks and five lowest valleys) [145].

3.6.2. Hydrogel coating thickness

Ellipsometry measurements were performed using an imaging ellipsometer, model EP3 and EP4, from Nanofilm Surface Analysis. Wet cell ellipsometry was performed by immersing substrates in PBS (pH=7.4). The light source was a solid-state laser with a wavelength of 532 nm. The parylene-c substrate refractive index (n = 3.829) and extinction coefficient (k = 1.459) were determined by using a delta and psi spectrum with an angle variation between 58° and 62°. These measurements were made in four zones to correct any instrument misalignment. The thickness of the PEG-4MAL hydrogels was determined considering n = 1.5 and k = 0, for the PEG-4MAL layer [146].

3.7. Distribution of site-specific immobilized LN on PEG-4MAL hydrogel coating

The laminin-functionalized silicon wafers were placed in the wells of a 48-well culture plate, fixed with 3.7% (w/v) paraformaldehyde (PFA) for 20 min at RT, and washed 3x with PBS (pH 7.4). Substrates were then incubated with blocking buffer (2% (w/v) BSA in PBS for 30 min at RT), followed by incubation with the primary antibody – rabbit polyclonal laminin antibody (1:200; Sigma-Aldrich, L9393), overnight at 4 °C. Substrates were washed 3x with PBS pH 7.4 and incubated with Alexa Fluor® 488 conjugated anti-rabbit secondary antibody (1:500; Life Technologies, A11034), for 1 h at RT. The substrates were finally rinsed trice with PBS, mounted in Fluoromount™ Aqueous Mounting Medium (Sigma), and finally observed under an inverted fluorescence microscope (Axiovert 200M Zeiss).

3.8. *In vitro* biological performance evaluation of the hydrogel coating decorated with site-specific immobilized laminin

Primary cultures of mouse cortical neurons were used to assess the ability of the surfaces to support cell adhesion and neurite extension of cortical neurons.

3.8.1. Suitability to support cell adhesion of cortical neurons

3.8.1.1. Isolation of cortical neurons:

16.5-day-old embryos from C57BL/6 female mice were used to isolate cortical neurons. Briefly, after removing the gravid uterus, fetal membranes and placenta were dissected away to reveal the pups. Cortical tissue was collected to a small petri-dish (35 mm), with sterile ice-cold Hanks Balanced Salt Solution (HBSS pH 7.4, Sigma-Aldrich) and maintained on ice until the cell culture room. Cells were dissociated using a 1.5 mg/mL trypsin (Gibco) solution in HBSS and washed with sterile HBSS. The cell suspension was further filtered with a 70 µm strainer to a sterile 50 mL tube.

3.8.1.2. Culture of cortical neurons on parylene-c surfaces coated with PEG-4MAL hydrogel decorated with site-specific immobilized laminin

Parylene substrates used in the cell culture studies were sterilized by immersion in ethanol 70% for 2 hours, and hydrogel coatings were prepared under sterile conditions. Unmodified parylene surfaces and parylene surfaces coated with bare PEG-4MAL hydrogel or PEG-4MAL hydrogel decorated with site-specific immobilized LN were transferred to a 48 well-plate suspension culture plate (CELLSTAR®), with the coating facing upwards. 40 microliters of cell suspension were added to the substrates to obtain a cell seeding density of 75×10^4 cells/mL. Cells were incubated at 37 °C for 2 h. 260 µL of culture medium were added. Culture medium consisted of Neurobasal Medium (Gibco, Life Technologies), supplemented with 2% v/v NeuroCult™ SM1 Neuronal Supplement (StemCell Technologies), 0.5 mM GlutaMAX (Gibco, Life Technologies), 50 µg/mL gentamicin and 25 µM glutamate. Cells were cultured for 24 h and 48 h. Unmodified parylene surfaces and surfaces coated with bare PEG-4MAL-based hydrogel were also used as controls).

3.8.1.3. DNA staining and cell adhesion quantification analysis:

After 24h and 48h of cell culture, the cultures were processed for DNA staining, for quantification of the number of adhered cortical neurons. To that end, 4′,6-diamidino-2-phenylindole (DAPI) was used. DAPI is a DNA-specific probe that binds to the minor groove of double-stranded DNA (preferentially to AT rich DNA), forming a stable complex which fluoresces approximately 20 times greater than DAPI alone.

The cell-seeded surfaces were fixed in 3.7% w/v PFA in cell culture media diluted 1:1 in culture media (30 min, 37 °C), and subsequently washed trice with PBS (5 min each rinsing step; RT). The cells were first permeabilized with 0.2% (v/v) Triton X-100 (Sigma) in PBS (10 min, RT), and washed trice in PBS (5 min, RT). Cells were then incubated with 0.1 µg/mL DAPI (1:10000; Sigma) in PBS for 10 min at RT, and washed trice in PBS (5 min each rinsing step, RT). All the incubation steps were performed under stirring (50 rpm) and in the dark. Except for the fixation step. Finally, substrates were mounted in Fluoromount™ Aqueous Mounting Medium (Sigma). Images covering the substrate area were acquired using a high content screening system (Opera Phenix Plus, PerkinElmer), and a 10× air objective, in confocal optical mode. For cell quantification 9 adjacent fields of view (fov) in the center of the substrate were used covering 0.18 cm^2 (72% substrate). The software used to perform image acquisition and analysis was Harmony 5.1 (PerkinElmer). Briefly, nuclei were segmented via the DAPI channel and selected with the following criteria: signal intensity >850 a.u. intensity STDev >200 a.u. and roundness >0.7. Total nuclei area per substrate region was then measured and results are expressed in total nuclei area divided by the analysed area.

3.9. Statistical Analysis

Statistical analysis was performed using SPSS® Statistics 25 software (IBM). Sample distribution was initially tested for normality using the Shapiro-Wilk test (commonly used for datasets with less than 50 samples). For normally distributed data, comparisons between two groups were performed with the unpaired t-test, while comparisons between three or more groups were performed with the one-way analysis of variance (ANOVA) followed by the Bonferroni's or Tukey's for samples with homogeneous variances, or Tamhane's test multiple comparison test, for samples without homogeneous variances. The two-way ANOVA test followed by Tukey's multiple comparisons test was used to assess the effect of two independent variables on the dependent variable as well as their potential interaction. Two-tailed significance levels were considered, and results found statistically significant are depicted with an asterisk for p-values < 0.05.

Chapter 4

Results and Discussion

4.1. Parylene-c and PU surface activation

To assure a stable binding of the PEG-MAL hydrogel to both parylene-c surfaces and PU surfaces, the surfaces were functionalized with silane-PEG-MAL, to allow the covalent binding of the hydrogel precursor PEG-4MAL, using dithiol. Due to the hydrophobic nature of parylene-c and PU surfaces, both surfaces were activated via O_2 or UVO plasma to introduce free OH groups at the surface, capable of reacting with silane groups. To assess surface activation, samples were characterized in terms of surface wettability (water contact angle measurements) and alterations in surface chemical composition (XPS).

4.1.1. Contact angle

The wettability of the surfaces was assessed by determining the water contact angle between the water and the polymeric surface, using the captive bubble method.

Parylene-c substrates: The effect of O_2 plasma treatment time on the water contact angle is shown in **Figure 13**. Contact angles significantly decreased after only 2 s of exposure to O_2 plasma reaching an average water contact angle (θ) value of 1,07° ± 0,68°. This remained unaltered over the range of plasma treatment periods examined. Results demonstrate the surface transition from hydrophobic to hydrophilic since untreated parylene C surfaces showed an average water contact angle (θ) of 81,89° ± 3,16°, which falls within the range of relatively high hydrophobicity [147]. The water contact angle of the untreated surface is similar to what has been reported in the literature [148]. Noteworthy, it is important to refer that the plasma conditions used in our studies may be different from those found in the literature, which may be the reason why the literature describes a less pronounced decline in the contact angle values for the short period of time tested [149]. The induced surface hydrophilicity of parylene-c upon exposure to O_2 plasma has been attributed to the fact that oxygen plasma initiates intermolecular reactions resulting in the formation of oxygen-containing functional groups [150].

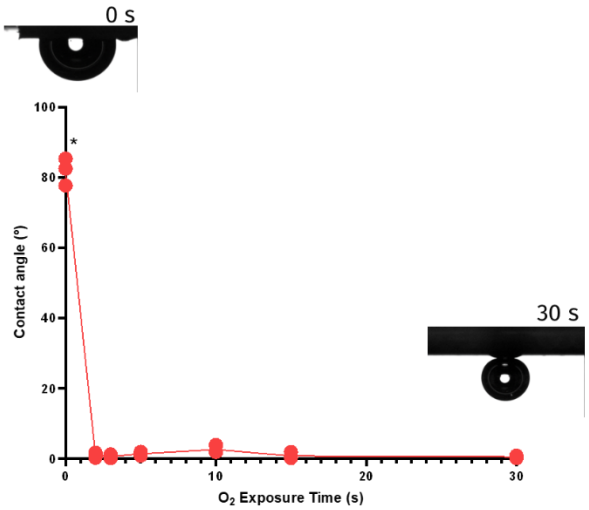

Figure 13 - Water contact angle (deg) of parylene-c as a function of O_2 plasma treatment exposure time, as determined by the captive bubble method. Results from three independent experiments; * $p < 0,05$ vs other time exposures (One-way ANOVA followed by Tamhane's test)

PU surfaces: The effect of UVO plasma treatment time on the water contact angle is shown in **Figure 14**. Contact angle significantly decreased with exposure time, reaching an average water contact angle

(θ) of 8,68° ± 2,95° upon an exposure time of 200 s. Increasing the exposure time to 300 s did not result in significant improvement in surface wettability. In fact, already for the shorter treatment time tested (50 s), water contact angle values significantly lower than that of unmodified PU (58,85° ± 1,12°) were observed, indicating that plasma treatment was effective in modifying the PU surface. It is important to refer that literature contact angle values of water on PU surface are slightly higher (65° to 75°) than those obtained in this experience [140]. Additionally, the linear trend of water contact angle values to decrease until reaching a constant value as exposure duration increases have also been observed in the literature. However, while UVO periods longer than 100 s have been said to be sufficient to reach a plateau, here it was only observed after 200 s [140]. The induced hydrophilicity of PU surface upon exposure to UVO treatment is believed to be related to the highly reactive oxidizing agents (atomic oxygen and ozone molecules) that react with polymer surface forming oxygen-containing functional groups, which are responsible for increased surface wettability.

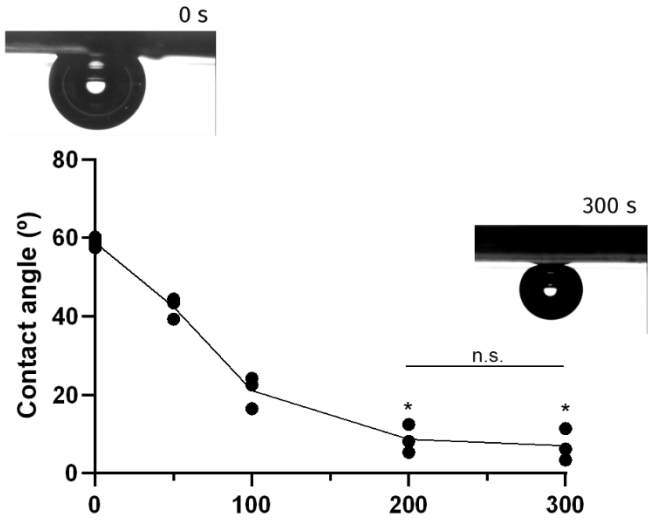

Figure 14 **-** Water contact angle (deg) of PU surfaces as a function of UVO plasma treatment exposure time, as determined by the captive bubble method. Results shown are from three independent experiments, performed in duplicate; *p < 0,05 vs other time exposures (One-way ANOVA followed by Bonferroni's test)

4.1.2. XPS analysis

Changes in the chemical composition of samples after surface activation were first evaluated through XPS analysis. This surface-sensitive quantitative spectroscopic technique provided information regarding the elemental composition and type of functional groups present at the polymeric surface upon plasma treatment.

Parylene-c surfaces: Surfaces exposed to plasma exposure time shorter or equal to 10 s were chosen for XPS analysis. The representative XPS survey spectra of unmodified parylene is shown in **Figure 15A**. Carbon and chloride are the two main components of parylene-c. Theoretically, chloride and carbon are present in parylene-c ($C_{16}H_{14}Cl_2$) in concentrations of 11% and 89%, respectively. The analysis of the element atomic percentages (%) calculated from the XPS survey of our samples shows for chloride and carbon atomic percentages are highly similar to the expected ones: 10.5 and 89.5%, respectively (**Table 1**). Following O_2 plasma treatment, the O 1s peak appeared and the C 1s peak diminished. Both C 1s and O 1s peaks suggest the introduction of oxygenated species into the outer parylene-c surface through O_2 plasma treatment. With increasing exposure time to O_2 plasma, the atomic percentages of chlorine and carbon consistently decreased, while that of oxygen increased (**Table 1**).

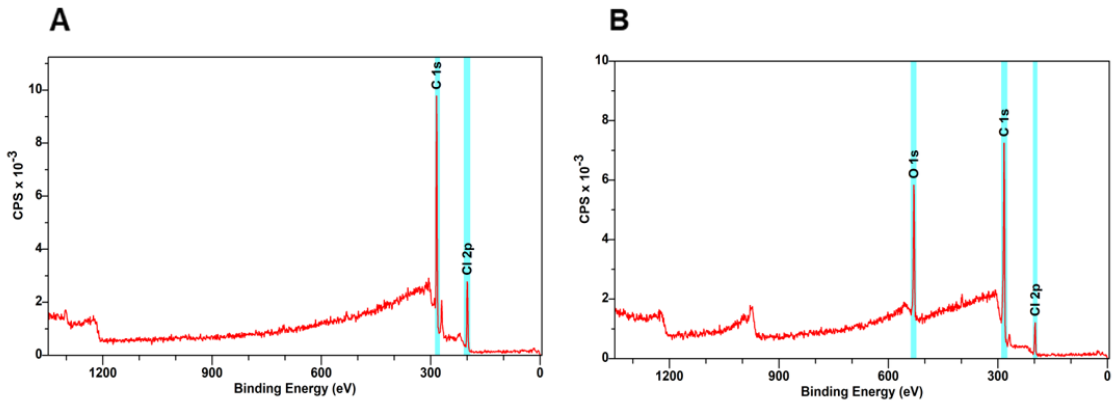

Figure 15 - XPS survey scans of parylene C substrates (A) unmodified and (B) modified for 10 s with oxygen plasma.

For a more detailed surface chemical analysis, high-resolution spectra of the C 1s and O 1s regions were acquired (**Figure 16**) In line with previous findings, both C1s and O1s peaks suggest the introduction of oxygen into the outer parylene-c surface through the plasma treatment. Curve-fitting of the C 1s high-resolution core XPS spectra was subsequently performed to get insight into the carbon species present. **Figure 17** shows representative C 1s spectra of unmodified parylene-c surfaces and parylene surfaces exposed to O_2 plasma for 10 s, after peak deconvolution. C 1s spectrum for non-modified parylene was deconvoluted into 3 peaks. The peak at the lowest BE (285.0 eV) corresponds to (C-C) and (C-H) bonding. The second peak, located around 286.4 eV, was assigned to the (C-Cl) bond. The third is a very small peak located at 291.4 eV, which possibly corresponds to the π-π* shake-up transition satellite of the aromatic ring [151]. The C1s spectrum shows significant chemistry change after O_2 treatment, in accordance with other studies, owing to the presence of carbon bound to oxygen, such in hydroxyl, carbonyl, and carboxyl species [147], and additional peaks were observed. The peak at 286.3 eV corresponds to the (C-OH) group. Two additional components are present at 287.6 eV and 289.4 eV binding energies, which were attributed to C=O and O–C=O groups, respectively. The presence of these hydrophilic groups explains the rise in surface wettability upon O_2 plasma treatment observed by contact angle measurements. The percentages of the different C 1s components, relative to that of the (C-C/C-H) component, are shown in **Table 1.** The C-OH/(C-C/C-H) ratio found suggests that **hydroxyl groups,** required for reaction with silane-PEG-MAL, are more numerous after 2 seconds of parylene exposure to O_2 plasma, beginning to decline with increasing treatment time.

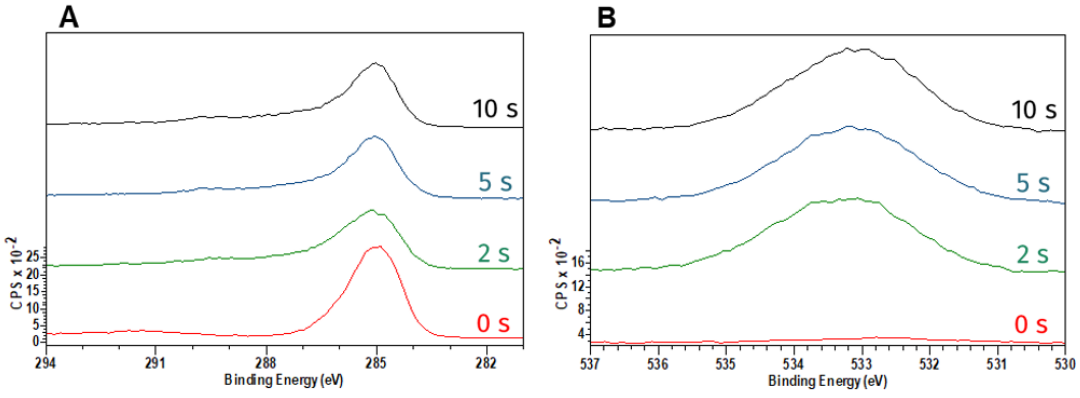

Figure 16 - Changes in C 1s (A) and O 1s (B) XPS high resolution spectra peak profile of parylene-c surfaces, as a function of O_2 plasma exposure time.

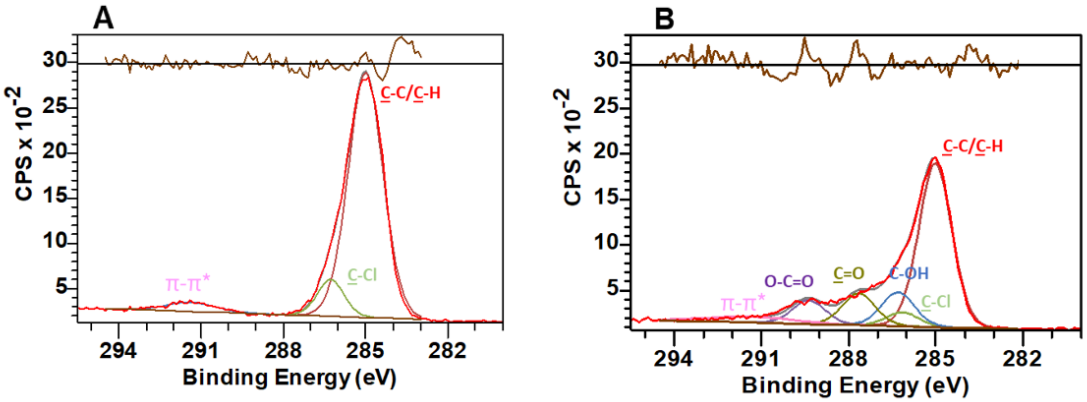

Figure 17 - XPS C 1s high-resolution spectra peak profiles and components obtained after curve fitting. (A) unmodified parylene-c surfaces and (B) parylene-c surfaces exposed to O_2 plasma for 10 s.

Table 1 - XPS Element Atomic Percentages obtained for parylene-c surfaces, as a function of O_2 plasma exposure time. The O/C atomic ratio and C 1s region component intensity ratios obtained after curve fitting are also shown.

C	C (%)	Cl (%)	O (%)	O/C	C-Cl/C-C	C-OH /C-C	C=O/C-C	O-C=O/C-C
0 s	89,5	10,5	-	-	11,7	-	-	-
2 s	79,9	4,6	15,6	19,5	13,0	29,0	18,6	14,2
5 s	79,2	3,9	16,9	21,4	8,9	21,1	18,2	13,2
10 s	78,6	3,3	18,2	23,1	8,5	20,7	19,5	14,4

PU surface: The XPS survey spectra of unmodified PU surfaces and PU surfaces exposed to UVO plasma for 300 s are depicted in **Figure 18**, and element atomic percentages are shown in **Table 2**. XPS results showed the characteristic peaks of PU, namely carbon (C1s), oxygen (O1s), and nitrogen (N1s), and atomic element percentages similar to those described in the literature [152]. After UVO plasma treatment, a significant increase in the oxygen content of the PU surface is expected as a result of the UVO treatment's breaking down of the long-chain PU molecules, between the soft and hard segment, which then allows atomic oxygen or ozone gas to react quickly to produce oxygen-carbon single and double bonding groups (hydroxyl, carbonyl and carboxyl species) [153]. Exposure to UVO plasma resulted in an increase in the oxygen atomic percentage (at%) with increasing exposure time, with correspondent reduction of the carbon at% and concomitant increase of the O/C ratio. The slight rise in nitrogen at% detected may be due to plasma-induced etching of the PU surface. [154]

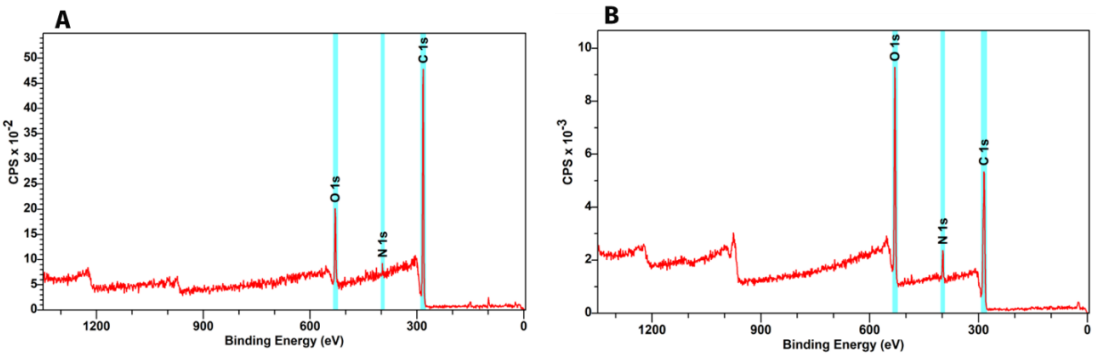

Figure 18 - XPS survey scans of (A) unmodified PU surfaces and (B) PU surfaces exposed to UVO plasma for 300 s.

For detailed chemical surface characterization, XPS high-resolution spectra of the C 1s and O 1s peaks were obtained (**Figure 19**). After UVO plasma treatment, changes in the shape of the C 1s envelope and in C 1s peak intensity were evident (**Figure 19A**). Spectral changes also occurred in the O 1s peak. The O 1s position remained unchanged, but with increasing exposure to UVO, an increase in peak intensity and peak broadening was noticeable (**Figure 19B**). **Figure 20A** shows a representative C 1s spectra of unmodified PU surfaces, after peak deconvolution. The C 1s spectrum of unmodified PU revealed the characteristic components of this polymer. The dominant peak at 285.0 eV corresponds to the (C-C/C-H) bond, the 286.4 eV peak is related to (C-O-C) and (C-NH-CO-O) bonds, and the third peak at 289,3 eV corresponds to (N–CO–O) bond in the urethane group (**Figure 20A**). Curve-fitting of a representative C 1s spectra of PU surfaces exposed to UVO plasma (300 s), is depicted in **Figure 20B**. After exposure to UVO plasma, plasma-induced hydroxyl species can be expected at the same binding energy as the ether groups and C-N-CO-O groups, from the polyurethane soft segment. Although the soft segment of the PU is probably removed by photolysis, the contribution of C-O species is presumed to maintain the concentration of this peak stable, as we also found (**Table 2**) [144, 149]. UVO-treated spectra showed an additional peak with an intensity of 288,3 eV, which corresponds to the binding energy of generated carbonyl groups (C=O) [144]. Carboxyl (COOH) have a binding energy similar to the N-CO-O groups and it is assumed to be the cause of the peak increase. The percentages of the different C 1s components, relative to the (C-C/C-H) component, are presented in **Table 2**. As the exposure to UVO plasma increases, the percentages of all oxygen-bound carbon species relative to that of the (C-C/C-H) component consistently increase. The presence of new hydrophilic groups containing carbon-oxygen bonds correlates well with the rise in surface wettability observed by contact angle measurements. The time for UVO plasma treatment chosen for the subsequent studies was **200 s,** due to the high C-OH/(C-C/C-H) ratio found in PU-surfaces after a 200 s UVO plasma treatment. Even though higher C-OH/(C-C/C-C) ratios were obtained after a 300 s treatment, this did not significantly improve the surface hydrophilicity, suggesting that few changes occurred at the surface. As such, all subsequent experiments were performed with PU surfaces activated for 200 s with UVO plasma.

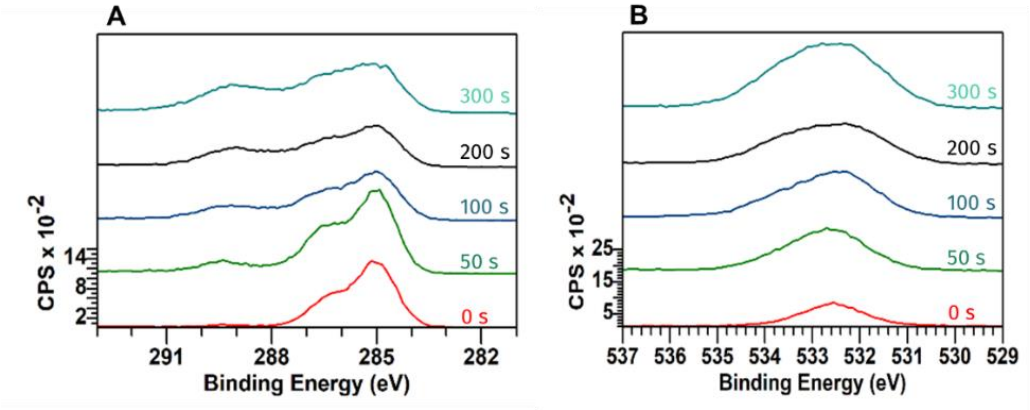

Figure 19 **-** Changes in C1s (A) and O1s (B) XPS high resolution spectra peak profile of PU surfaces, as a function of UVO plasma exposure time.

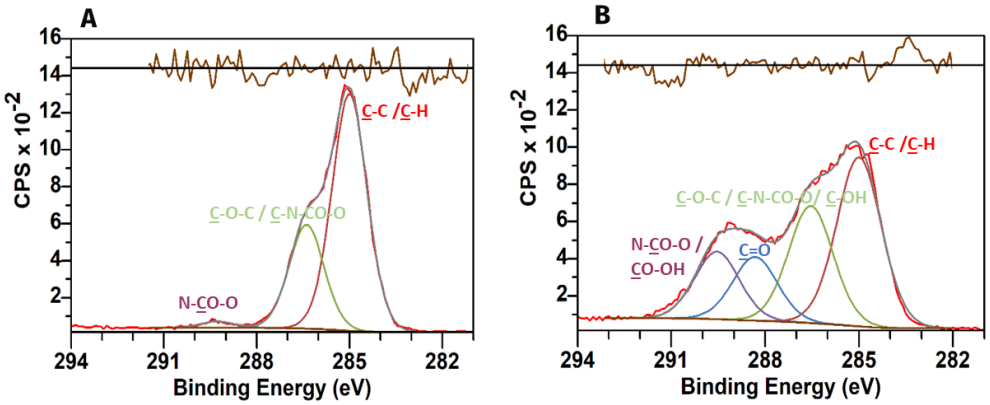

Figure 20 - XPS C 1s high resolution spectra XPS peak profiles and components obtained after curve fitting. (A) unmodified PU surfaces and (B) PU surfaces exposed to UVO plasma for 300 s.

Table 2 - XPS Element Atomic Percentages obtained for PU surfaces, as a function of UVO plasma exposure time. The O/C atomic ratio and C 1s region component intensity ratios relative to that of the C-C/C-H component are also shown. For atomic percentages, results are the mean of 3 measurements performed in random locations of the sample (N = 1). The component intensity ratios presented correspond to representative C 1s high resolution spectra.

	C (%)	O (%)	N (%)	O/C	C-O-C, C-N-CO-O, C-O-C, C-N-CO-O, C-OH / C-C	N-CO-O, N-CO-O, COOH / C-C	C=O / C-C
0 s	87,57 ± 0,63	10,80 ± 0,27	1,63 ± 0,91	0,12	43,84	2,76	-
50 s	82,09 ± 0,40	15,38 ± 0,19	2,53 ± 0,28	0,19	54,17	12,53	6,15
100 s	78,23 ± 0,98	17,93 ± 1,06	3,84 ± 0,08	0,22	55,66	23,71	17,72
200 s	76,23 ± 2,13	19,81 ± 1,60	3,96 ± 0,55	0,25	60,02	38,83	26,40
300 s	72,37 ± 2,42	24,26 ± 1,19	3,37 ± 1,23	0,31	69,27	37,77	40,00

4.1. Surface functionalization with silane-PEG-MAL

To assess the functionalization of the surfaces with silane-PEG-MAL, surfaces were characterized in terms of maleimide surface density (Thiol Assay), alterations in surface chemical composition (XPS and FTIR- ATR) and surface topography (AFM).

4.1.1. Maleimide surface density

Maleimide groups in PEG-4MAL macromers efficiently react with thiol-containing moieties through Michael-type addition. As such, to quantify maleimide surface density, we measured the amount of unreacted/free thiols after surface incubation with reduced glutathione (GSH), using a Fluorometric Thiol Quantitation Kit.

Parylene-c surfaces: To optimize the surface functionalization of parylene-c with silane-PEG-MAL, two different concentrations of silane-PEG-MAL were tested (10 and 25 mg/mL) on parylene surfaces activated with O_2 plasma for 2, 5, or 10 s. **Figure 21** shows the maleimide surface density achieved for each condition. While the O_2 exposure time did not significantly impact the maleimide surface density, surface functionalization with 25 mg/mL of silane-PEG-MAL resulted in significantly higher maleimide surface densities, compared to the use of 10 mg/mL. As such, 25 mg/mL was the silane-PEG-MAL concentration selected to functionalize parylene-c surfaces with maleimide groups in the subsequent studies. Additionally, since a longer exposure to O_2 plasma did not result in higher maleimide surface densities, the shortest O_2 plasma treatment was chosen, due to its higher ability to generate OH groups on parylene-c surfaces. However, since the 2 s O_2 treatment was difficult to replicate, 5 s treatments were selected for use in the subsequent assays.

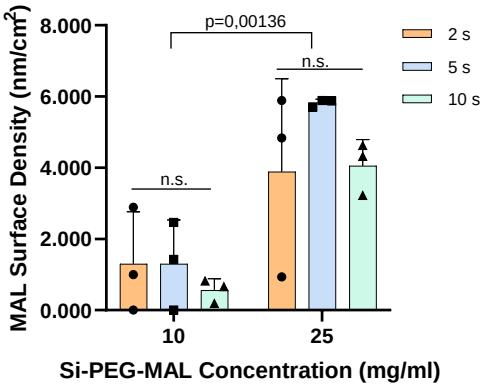

Figure 21 - Maleimide surface density of parylene-c surfaces after functionalization with silane-PEG-MAL, as a function of O_2 exposure time and silane-PEG-MAL concentration. Results from three independent experiments are shown. The use of the highest silane-PEG-MA concentration tested (25 mg/mL) resulted in significantly higher MAL surface densities, but the O_2 exposure time did not affect the latter. Two-way ANOVA test ($p < 0,01$ for PEG Concentration effect, $p = 0,286$ for Exposure time effect, $p = 0,491$ for interactions)

PU surfaces: For PU surface functionalization, three concentrations of silane-PEG-MAL were tested (5, 10, and 25 mg/mL) on PU surfaces activated with UVO plasma (200 s). While there were no significant differences between 5 and 10 mg/mL of silane-PEG-MAL, the use of 25 mg/mL led to significantly higher maleimide surface densities, when compared to the other two concentrations tested (**Figure 22**). The concentration of silane-PEG-MAL chosen for surface functionalization of PU surfaces with maleimide groups was therefore **25 mg/mL**.

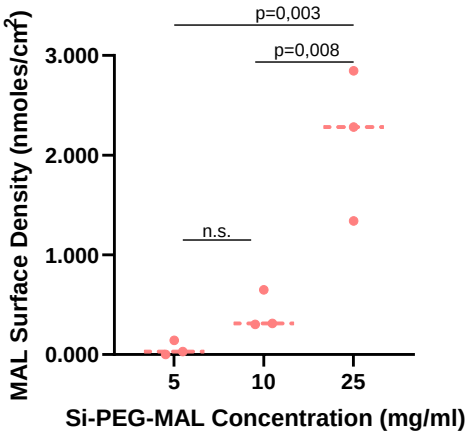

Figure 22 - Maleimide surface density of PU surfaces after functionalization with silane-PEG-MAL, as a function of silane-PEG-MAL concentration. Results from three independent experiments are shown. The use of the highest silane-PEG-MA concentration tested (25 mg/mL) resulted in significantly higher MAL surface densities when compared to any of the lower concentrations tested (One-way ANOVA followed by Tuckey).

4.1.2. XPS Analysis

Parylene-c and PU functionalization was also validated using XPS analysis. The presence of the moiety is determined by searching for the atomic element (silicon) present in silane-PEG-MAL but absent in both parylene and PU.

Parylene-c surfaces: Figure 23 shows the survey spectra of oxygen plasma treated for 5 s parylene-c samples and the spectra of oxygen plasma treated for 5 s functionalized with 25 mg/mL of silane-PEG-MAL parylene-c. The presence of a silicon peak assures the presence of the moiety. Additionally, because parylene-c lacks nitrogen as well, and this element is also present in the moiety, a nitrogen peak also appears. The correspondent element atomic percentages calculated from the survey spectra

are presented in **Table 3**. Higher percentages of silicon and nitrogen are found on the surface after functionalization with the highest silane-PEG-MAL concentration tested (25mg/mL). This result supports the results from the quantitative analysis of maleimide surface density using the Fluorometric Thiol Quantitation Kit, which revealed a higher maleimide surface density after surface functionalization using 25 mg/mL of silane-PEG-MA. As such, in all subsequent experiments, O_2-activated parylene-c surfaces were functionalized with 25 mg/mL of silane-PEG-MAL.

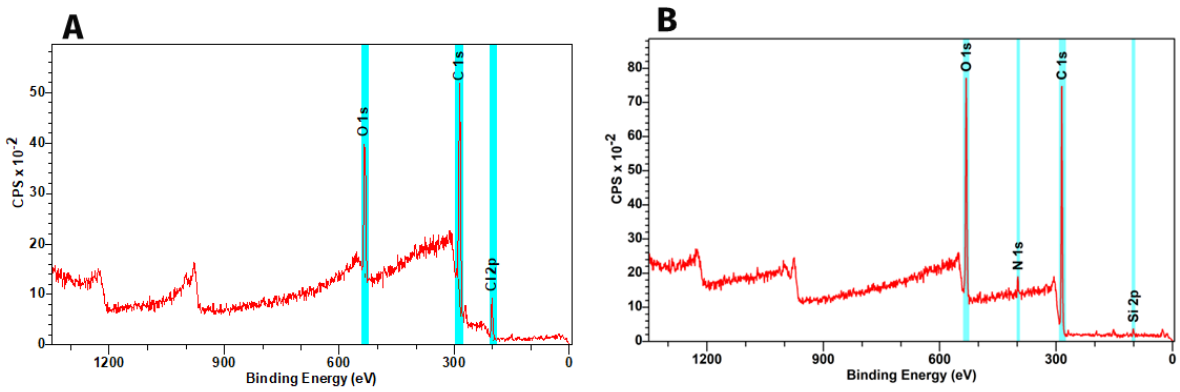

Figure 23 **-** XPS survey scans of parylene-c surfaces. (A) activated with O_2 plasma for 5 s, and (B) activated with O_2 plasma and functionalized with 25 mg/mL of silane-PEG-MAL.

Table 3 **-** XPS Element Atomic Percentages obtained for parylene surfaces activated with O_2 plasma for 5 s (O_2 activated) or parylene surfaces activated with O_2 plasma and functionalized with 10 or 25 mg/mL of silane-PEG-MAL (si-PEG-MAL 10 and si-PEG-MAL 25, respectively). Results are the mean of 3 measurements performed in random locations of the sample (N = 1).

	O_2 treated	**silane-PEG-MAL concentration (mg/mL)**	
		10	25
O	16,93	15,08	22,50
C	79,18	81,05	73,88
Cl	3,89	2,98	0,00
N	0,00	0,73	2,34
Si	0,00	0,17	1,27

PU surfaces: The XPS survey spectrum of UVO-activated PU surfaces functionalized with 25 mg/mL of si-PEG-MAL PU films is displayed in **Figure 24.** The appearance of the Si 2p peak indicates the presence of silane-PEG-MAL. The correspondent element atomic percentages are presented in **Table 4**. Again, the higher percentages of silicon were achieved using the highest silane-PEG-MAL concentration tested. These results are in accordance with the trend observed for higher maleimide surface densities when using silane-PEG-MAL at 25 mg/mL. For this reason, this silane-PEG-MAL concentration appears to be effective for the functionalization of UVO-activated PU surfaces.

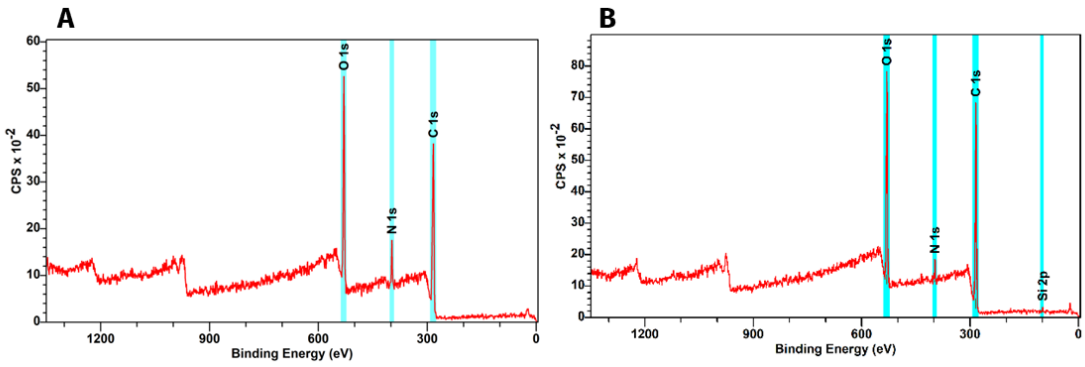

Figure 24 - XPS survey scans of PU surfaces. (A) activated with UVO plasma (200 s) and (B) activated with UVO plasma and functionalized with 25 mg/mL of silane-PEG-MAL.

Table 4 - XPS Element Atomic Percentages obtained for PU surfaces activated with UVO plasma (200s) and functionalized with silane-PEG-MAL, as a function of silane-PEG-MAL concentration. Results are the mean of 3 measurements performed in random locations of the sample (N = 1).

	UVO treated	silane-PEG-MAL concentration (mg/mL)		
		0	10	25
O	19,81	13,44	23,72	22,29
C	76,23	85,18	72,06	72,86
N	3,96	1,12	3,64	3,06
Si	0,00	0,25	0,58	1,79

4.1.3. ATR-FTIR

Fourier transform infrared spectroscopy identifies the main chemical functional groups of the outer surface (information depth of 0.5 µm–2 µm) of samples and any additions or changes to the chemical composition after plasma treatment. This technique uses the unique absorption of IR radiation of specific functional groups for the chemical characterization of a polymer [155]. FTIR was used to investigate the modifications in the surface chemistry of the parylene-c and PU samples after O_2 and UVO treatment, respectively, and subsequent si-PEG-MAL functionalization. This technique identifies the main functional groups and the chemical structure of polymeric materials by the absorption of IR radiation by vibrations.

Parylene-c surfaces: The ATR-FTIR spectrum of unmodified parylene-c surfaces, as well as the chemical structure of parylene-c, is shown in **Figure 25**. The characteristics bands of parylene-c include the peaks of C-C and C=C bonds, related to the stretching vibration of the benzene ring (1451 to 1608 cm^{-1}) [151]. The linear aliphatic structure of the methylene groups (CH_2) is observed by the C–H stretching vibrations at 2925 cm^{-1} and 2861 cm^{-1} and the C-H bending vibrations at 1493 cm^{-1} [156]. The peak at 3019 cm^{-1} was assigned to the stretching vibration of the C-H bond on the aromatic ring. The peak at 824 cm^{-1} represents the two C-H bending vibrations of the adjacent hydrogen atoms on the benzene ring, while the peak at 877 cm^{-1} represents the other C-H bending vibration of the adjacent hydrogen atom. The second energy vibration is overlayed by one of the C-Cl energy vibrations [151]. C-Cl stretching vibration corresponds to the peaks at 1049 cm^{-1} and 875 cm^{-1} [157, 158]. According to the literature, oxygen-containing groups appear in parylene structures after oxygen plasma treatments with exposure time superior to 5 seconds. The oxygen-containing groups include carbonyl groups (C=O), associated with carboxylic acids or aldehydes with stretching vibrations at 1700 cm^{-1} [158], O-H groups from carboxylic acids present at the high-frequency region, around 3100 cm^{-1}, and C-O groups, with a stretching vibration peak from 1085 cm^{-1} to 1310 cm^{-1} [158]. Additionally, as previously mentioned, the bands' intensities linked to aromatic C-H and C-Cl stretching vibrations may decrease following plasma exposure. This may indicate the role of aromatic groups in functionalization

reactions. However, no significant changes were observed in this peak after parylene-c O_2 treatment. Results are depicted in Appendix A. Parylene may not have been exposed to oxygen long enough for the technique to detect chemical changes. These results suggest that the parylene-c chemical structure was not significantly modified by the applied O_2 plasma treatments, so that to be detected by ATR-FTIR, a technique which is far less surface sensitive than XPS (information depth of 5 to 10 nm). Other studies have also reported no discernible changes in parylene-c ATR-FTIR spectra caused by oxidation or substitution of functional groups after plasma treatment in parylene-c samples [147]. Parylene-c surface chemical structure preservation may be an indicator that significant polymer features, such as insulation properties, were preserved. The rise in PEG content with silane-PEG-MAL was expected to be detected through the presence of PEG' distinctive vibrations, namely C-O-C stretching at 1104 cm^{-1} and C-H stretching of O-CH_2 at 2855 cm^{-1} [159]. However, no evident differences were found in the ATR-FTIR spectra of parylene-c surfaces functionalized with silane-PEG-MAL, compared with that of oxygen-treated surfaces. Regarding the maleimide group, characteristic vibrations include a prominent band related to the imide I at 1713 cm^{-1}. Stretching vibrations of the other maleimide group members include imide II and imide IV at 1397 cm^{-1} and 695 cm^{-1}, respectively, and CH of CH=CH group and C=C stretch at 828 cm-1 and 1600 cm^{-1}, respectively [160]. However, there were no significant changes in these wavenumber regions that might suggest the presence of maleimide groups. Results are depicted in Appendix A.

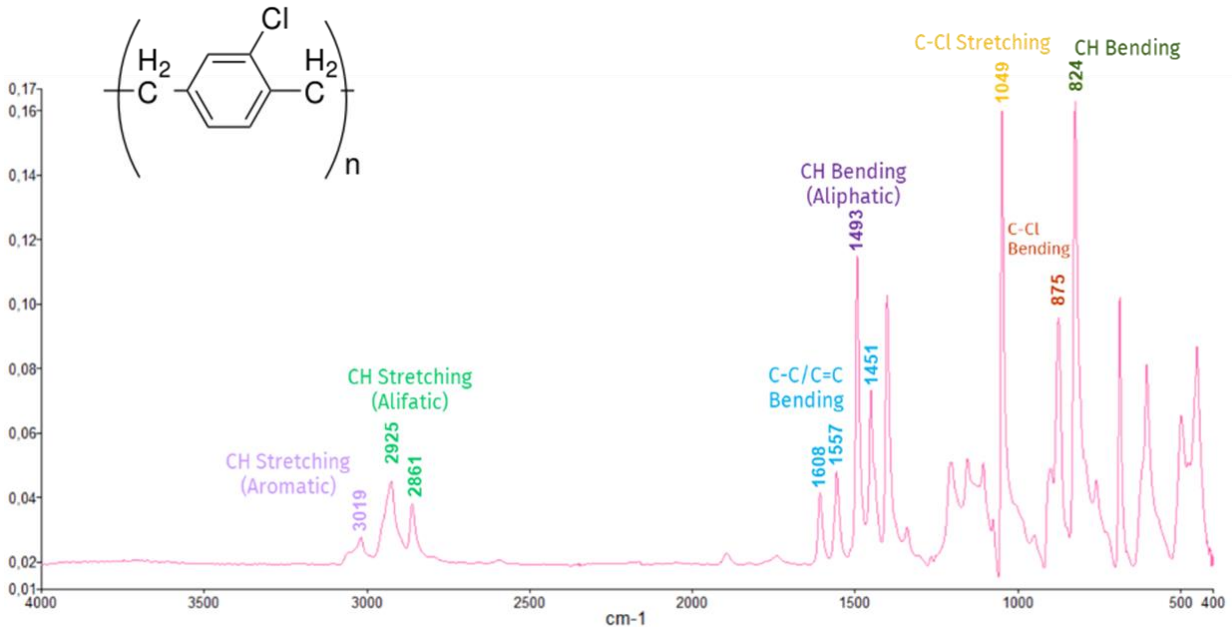

Figure 25 **-** ATR-FTIR absorption spectrum of an unmodified parylene-c surface.

PU surfaces: A representative ATR-FTIR spectrum of unmodified PU surfaces, as well as the chemical structure of PU is depicted in **Figure 26**. Spectra obtained is very similar to the ones found in the literature. PU bands include N–H stretching vibration at 3325 cm^{-1} and C–H stretching vibration of O–CH_2 at about 2939 cm^{-1} and 2854 cm^{-1}. According to their conjugation, carbonyl groups have different vibrations at 1730 cm^{-1} and 1700 cm^{-1} for (N–C=O) and (O–C=O), respectively. Spectrum also includes N–H stretching vibration from the urethane group (N–CO–O) at 1529 cm^{-1}, C–H bending vibration of the urethane group at 1414 cm^{-1}, C–O and C–N stretching vibration at 1221 cm^{-1}, and the C–O–C stretching vibration at 1104 cm^{-1} and 1078 cm^{-1} [159, 161]. **Figure 27** presents the spectra of unmodified and UVO plasma treated after 300s. After exposure to UVO plasma, no significant changes were observed in the C-H stretching vibration of O-CH_2 at 2854 cm^{-1}, as well as the stretching vibration of C-O-C at 1103 cm^{-1}. Since the UVO treatment is reported to introduce oxygen-containing groups in the PU surface such as carbonyls, carboxyls, and hydroxyls, characteristic bands may appear/increase in the spectrum.

However, the O-H stretching vibration of the free group or intermolecular bonded, at 3700-3584 cm^{-1} and 3550-3200 cm^{-1}, respectively, was not very evident in the spectrum, and only a broadening of the peak near the N-H stretching peak, at about 3400 and 3500 cm^{-1}, was observed. According to the literature, C=O stretching vibration from the carboxylic acid is located at 1760 cm^{-1} [162]. The presence of PU vibrations in this wavenumber region makes it harder to detect changes. We observed an increase in the peak at 1728 cm^{-1}, associated with the C=O stretching vibration of the N-C=O group, as well as a peak at 1776 cm^{-1}, which may be due to the C=O stretching vibration from free carboxyl groups. Upon functionalization with silane-PEG-MAL, neither the characteristic vibrational peaks of PEG nor those of the maleimide group were detected. Results are depicted in Appendix B. Maleimide groups are particularly difficult to detect in PU, due to the overlap of PU characteristic. As such, when comparing the UVO-treated PU surfaces with those functionalised with silane-PEG-MAL, no noticeable differences were found. The lack of differences suggests that silane-PEG-MAL forms a very thin layer on top of PU surfaces which cannot be detected using ATR-FTIR, due to its low surface sensitivity.

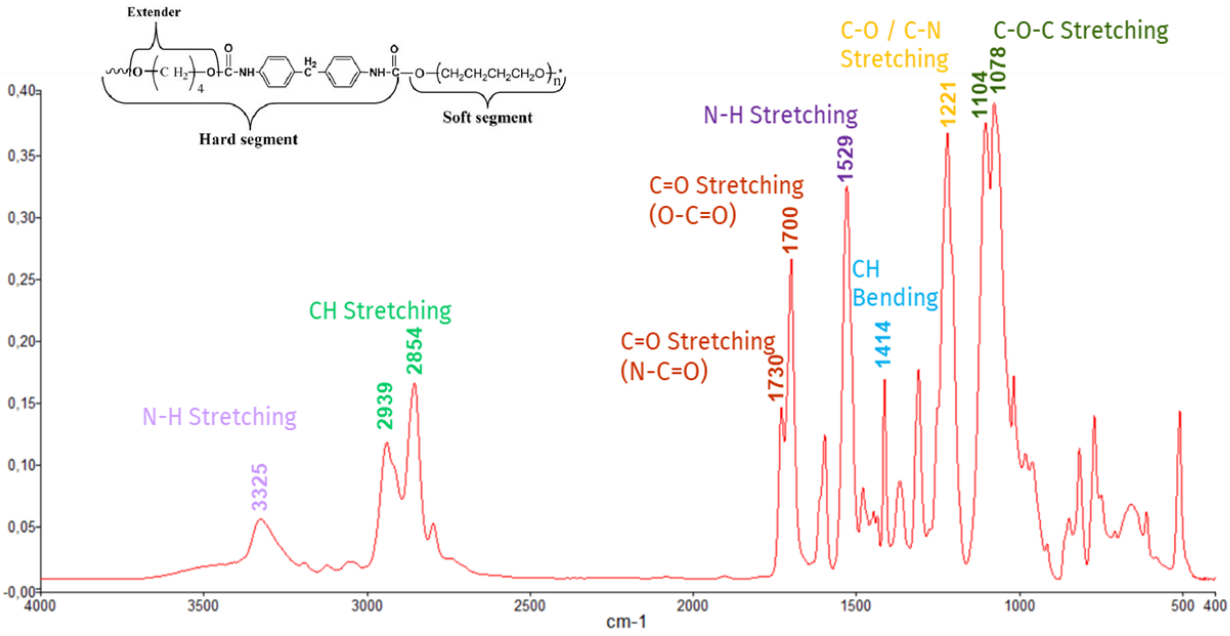

Figure 26 - ATR-FTIR absorption spectrum of an unmodified PU surface.

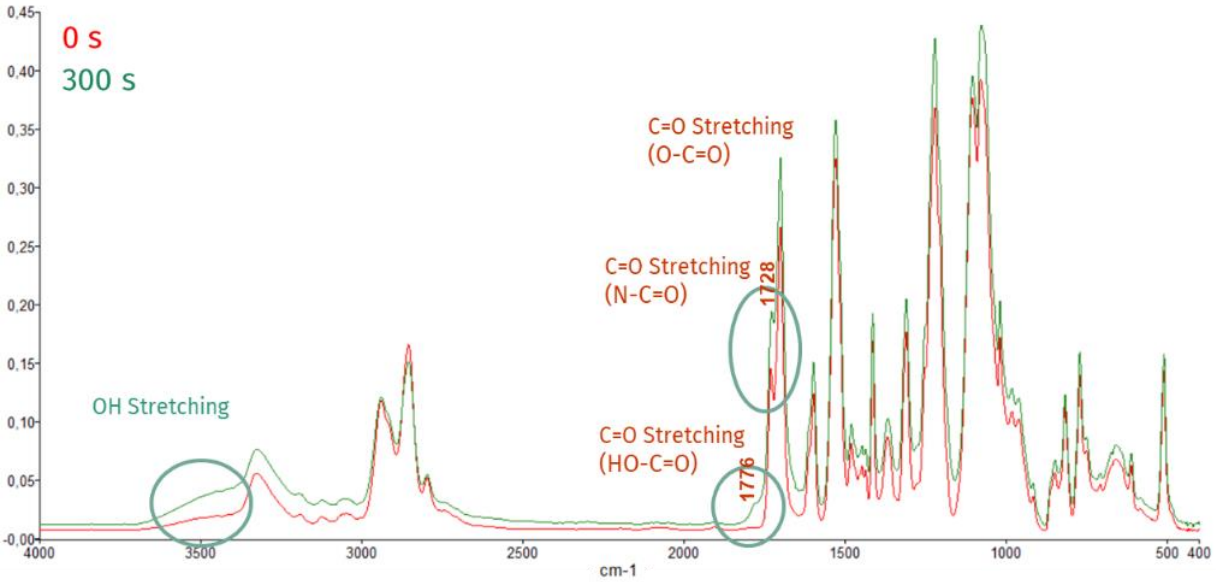

Figure 27 – ATR-FTIR absorption spectra of unmodified PU surfaces (red) and PU surfaces exposed to UVO plasma for 300 s (in green).

4.1.4. AFM

AFM technique is a powerful tool that enables both nanoscale imaging and nanomechanical characterization of biological materials in physiological conditions [163].

Parylene surfaces: In the 2D AFM images of the unmodified surfaces, O_2 plasma treated (5 s) surfaces and surface sample functionalized with silane-PEG-MAL parylene-c are presented in **Figure 28**. No significant differences in surface topography were observed. **Table 5** displays the surface roughness parameters found analysis for the different surfaces. No appreciable variations were detected upon surface activation with O_2 plasma. Despite the reports in the literature describing a slight increase of surface roughness with increased O_2 exposure time, these observations were found for treatment times longer than 5 s [164]. After functionalization using si-PEG-MAL, there were no discernible changes in surface roughness, as shown in **Table 5**, which suggest a uniform deposition of silane-PEG-MAL or, alternatively, lack of functionalization. Since the grafting of silane-PEG-MAL to parylene surfaces was previously validated by XPS and using a Fluorometric Thiol Quantitation Kit, it is difficult to assume that functionalization did not take place.

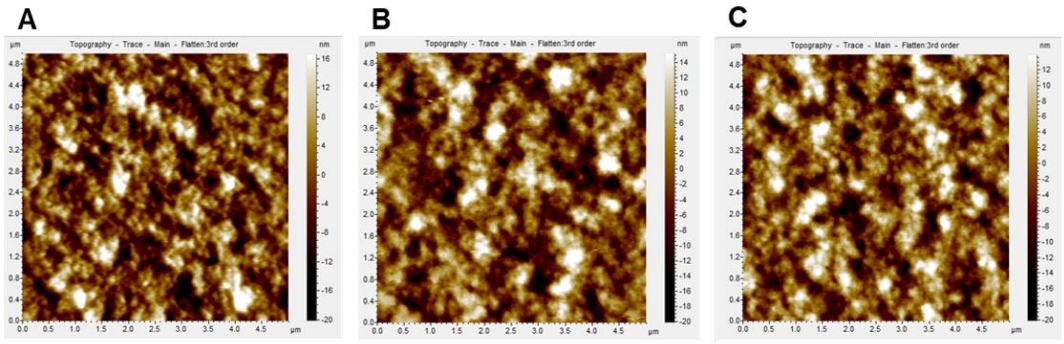

Figure 28 **-** 2D AFM images of unmodified parylene surfaces (A), O_2-plasma treated parylene-c surfaces (B), and parylene-c surfaces functionalized with silane-PEG-MAL (C). Images acquired under ambient conditions.

Table 5 **-** Surface roughness parameters of unmodified parylene-c, O_2-plasma treated parylene-c, and parylene-c surfaces functionalized with silane-PEG-MAL, determined over a 5x5 µm² scanned area. Results are the mean ± SD of 3 measurements (N=1)

	R_a (nm)	R_z (nm)
Unmodified parylene-c	6,82 ± 0,63	67,78 ± 4,27
Oxygen treated	6,46 ± 0,23	65,46 ± 1,19
silane-PEG-MAL	6,94 ± 0,57	61,81 ± 6,90

PU surfaces: 2D AFM images of unmodified surfaces, surfaces treated with UVO plasma (for 200 s), and surfaces functionalized with silane-PEG-MAL, are presented in **Figure 22,** and the correspondent area roughness analysis in **Table 6**. All surfaces revealed homogenous and smooth surfaces. Nevertheless, measured values of roughness parameters for unmodified surfaces were superior to those reported in the literature, which may be due to the solving cast process used for the preparation of PU surfaces, which can produce minor imperfections at the surface [165]. In addition, while we expected a rise of the surface roughness resultant from the UVO treatment [165], this trend was not observed. Surface functionalization with silane-PEG-MAL resulted in rougher surface, as suggested by the increase in the R_a and R_z values, when compared to unmodified and UVO-treated PU surfaces (**Table 6**). These findings further support an effective functionalization.

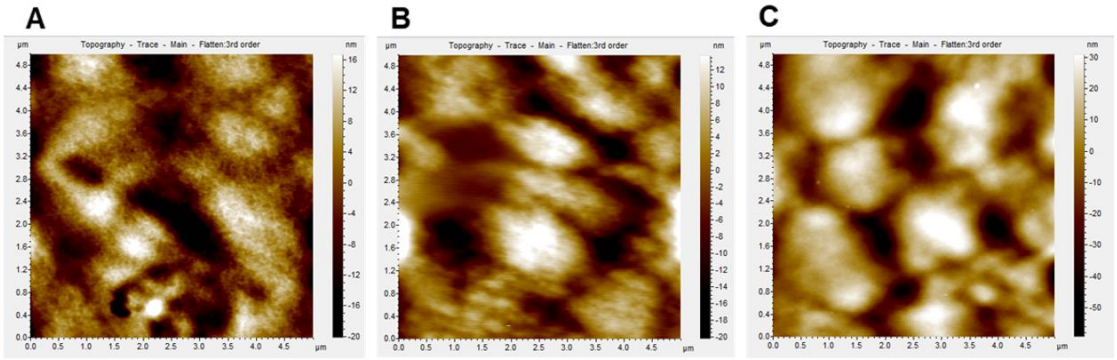

Figure 29 **-** 2D AFM images of unmodified PU surfaces (A), UVO-plasma treated PU surfaces, and PU surfaces functionalized with silane-PEG-MAL. Images acquired under ambient conditions.

Table 6 **-** Surface roughness parameters of unmodified PU, UVO-plasma treated PU, and PU surfaces functionalized with silane-PEG-MAL. Surface roughness was determined over a 5x5 µm² scanned area. Results are the mean ± SD of 3 measurements (N=1).

	R_a (nm)	R_z (nm)
Unmodified PU	10,71 ± 0,55	85,67 ± 15,26
UVO treated	10,51 ± 2,02	74,66 ± 10,29
silane-PEG-MAL	26,49 ± 1,86	161,46 ± 15,92

4.2. Coating of parylene-c surfaces with PEG-4MAL-based hydrogels

Due to time constraints, the deposition of PEG-4MAL hydrogels was only tested on parylene-c surfaces.

A final polymer concentration of 10% (w/v) was used. This density is described to form hydrogels with mechanical properties around 187 to 256 Pa [128], which is within the range of values preferred to interact with brain tissue (400-1000Pa) [166], and to allow neurite branching and extension (200–400 Pa) [128].

Parylene surfaces were subjected to 2, 4 or 6 PEG-4MAL/PEG-dithiol treatments (PEG-4MAL hydrogel ×2 and PEG-4MAL hydrogel ×4, PEG-4MAL hydrogel x6 depositions, respectively). To confirm the presence of a PEG-4MAL hydrogel, surfaces were characterized in terms of chemical composition (FTIR), surface topography (AFM), and hydrogel thickness (ellipsometry).

4.2.1. ATR-FTIR

The ATR-FTIR spectrum of a PEG-4MAL hydrogel ×2-coated parylene-surfaces (**Figure 30**), did not show the typical absorption peak of the sulfhydryl (-SH) at around 2400 cm^{-1} [167], suggesting the absence of free thiol groups, and the full reaction of –SH groups from the PEG-dithiol cross-linker with the maleimide groups from the PEG-4MAL macromer via Michael-type reaction [167]. The stretching vibration correspondent to the soft segment of C–O–C from PEG at 1150 cm^{-1} [159], also present in PEG-dithiol, was not detected. Nevertheless, the FTIR spectra showed an absorbance peak around 1643 cm^{-1}, which was assigned to the amide I peak (C=O stretching vibration) of the amide bond present, close to the maleimide groups of the PEG-4MAL macromer used [168]. The amide group has typical absorption spectrum bands: amide I (1600-1800 cm-1), amide II (1470-1570 cm-1), amide III (1250-1350 cm-1), and amide A (3300-3500 cm-1) [169]. It is challenging to observe the amide II, III and A spectrum bands since they are overlaid by parylene-c vibrations. After PEG-4MAL hydrogel deposition, all the characteristic vibrational peaks of parylene-c were less evident, becoming less apparent with the increase of PEG-4MAL/PEG-dithiol treatments. Results are depicted in Appendix C. O-H stretching vibrations appear around the high spectrum region, indicating the presence of water [170]. This was expected since the substrates were characterized in a hydrated state.

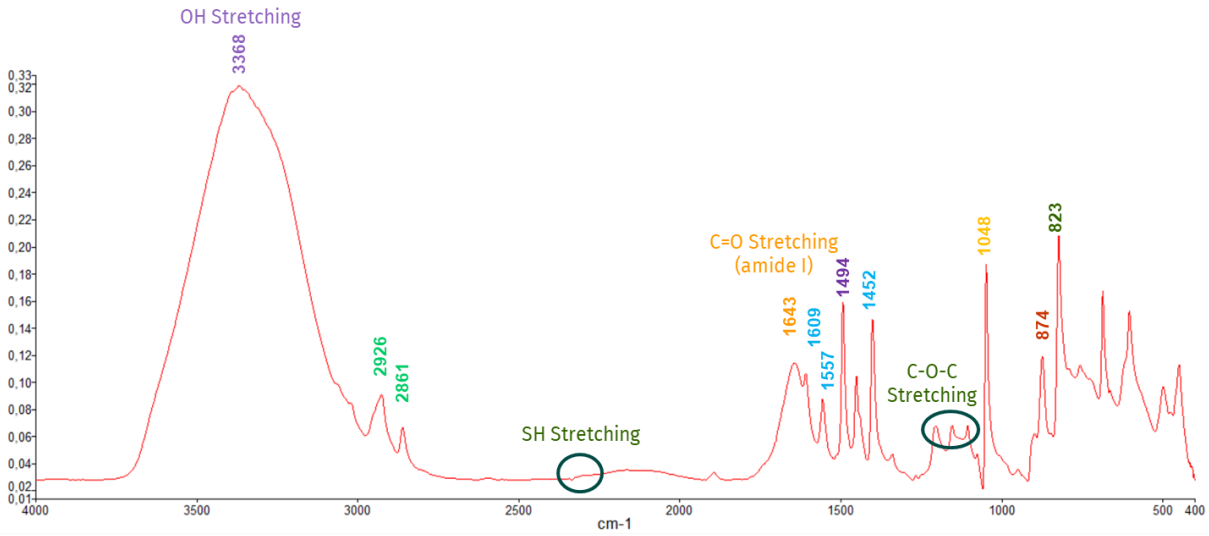

Figure 30 **-** ATR-FTIR absorption spectrum of a parylene-c surface coated with PEG-4MAL hydrogel x2-based coating under hydrated conditions.

4.2.2. AFM

Three-dimensional (3D) AFM images of untreated parylene-c surfaces, and parylene surfaces subjected to 2 or 4 PEG-4MAL/PEG-dithiol treatments (PEG-4MAL hydrogel ×2 and PEG-4MAL hydrogel ×4, respectively) are shown in **Figure 31**. The AFM 3D images of unmodified parylene show in general, a smooth surface, with a z-axis data scale of 712,5 nm (**Figure 31A**). Area roughness analysis reveals values for R_a and R_z of 6,81 and 67,77 nm, respectively (**Table 7**). After 2 PEG-4MAL/PEG-dithiol treatments, the surfaces showed a distinct surface morphology and a rise in the z-axis data scale to 1,5 µm suggesting hydrogel deposition (**Figure 31B**). Although the R_a value was similar to that of unmodified surfaces, the R_z value obtained was higher. These differences were more evident after 4 PEG-4MAL/PEG-dithiol treatments, as shown by the rise of the 3D image z-axis scale to 4,2 µm (**Figure**

31C) and by the increase of the Ra and Rz to 36,89 nm and 336,52 nm, respectively (**Table 7**), further suggesting the successful deposition of the hydrogel at the surface.

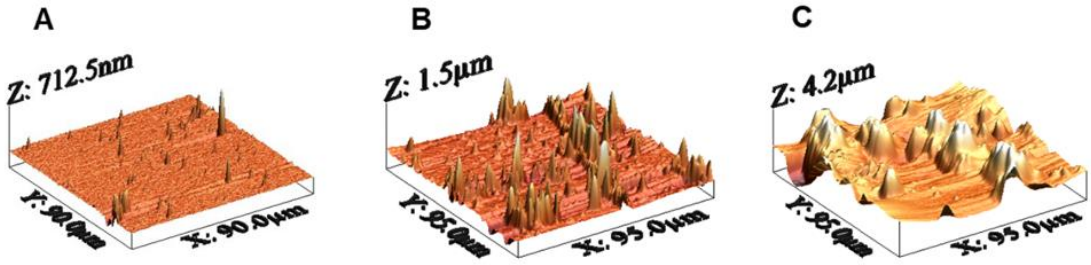

Figure 31 **-** Three-dimensional (3D) AFM images of unmodified parylene-c surfaces (A) parylene-c surfaces subjected to 2 4MAL/PEG-dithiol treatments (B), and parylene-c surfaces subjected to 4 PEG-4MAL/PEG-dithiol treatments (C). Images were acquired under ambient (A) or liquid (B and C) conditions.

Table 7 **-** Surface roughness parameters of unmodified parylene-c, parylene-c surfaces subjected to two 4MAL/PEG-dithiol treatments (PEG-4MAL Hydrogel ×2), and parylene-c surfaces subjected to four PEG-4MAL/PEG-dithiol treatments (PEG-4MAL Hydrogel ×4). Surface roughness was determined over a 5x5 µm^2 scanned area. Results are the mean ± SD of 3 measurements (n = 1).

	R_a (nm)	R_z (nm)
Unmodified parylene-c	6,82 ± 0,63	67,78 ± 4,27
PEG-4MAL hydrogel x2	6,68 ± 0,93	96,72 ± 32,71
PEG-4MAL hydrogel x4	36,89 ± 13,29	336,52 ± 216,73

4.2.3. Hydrogel Thickness

Ellipsometry is a very sensitive, non-destructive technique used to measure the changes in light polarization as this is reflected from a material structure, which in turn allows the determination of a thin film thickness.

Because PEG-4MAL hydrogel coatings' water content interferes with the light reflected from the substrate, wet cell method is a better option for determining the hydrogel's thickness. Wet cell ellipsometry allows to analyse of the samples in a wet environment. However, while performing the method, the standard deviations acquired were too high for data to be considered accurate. This might be a result of the equipment's limitations, as it can only scan the light at a particular wavelength (532 nm). Thickness assessment through wet cell ellipsometry has already been reported, however, the method was performed by scanning from 350 nm to 800 nm [133].

4.3. Deposition of a PEG-4MAL- based hydrogel coating decorated site-specific immobilized laminin.

4.3.1. Laminin immobilization

Laminin immobilization was qualitatively assessed at a first approach, examining laminin distribution at the surface, via immunofluorescence. According to the results, bare parylene-c substrates exhibit residual or non-existent LN (fluorescent signal), confirming the lack of autofluorescence from the substrate. (**Figure 32A**). Laminin was incubated with parylene-c surface coated with PEG-4MAL hydrogel functionalized with LN using 5 and 10 µM of NtA (**Figure 32B, C**). Fluorescence images show a bright green colour along the surface substrates, indicating the presence of LN. Furthermore, fluorescence is observed along the entire surface, suggesting a homogenous distribution of LN.

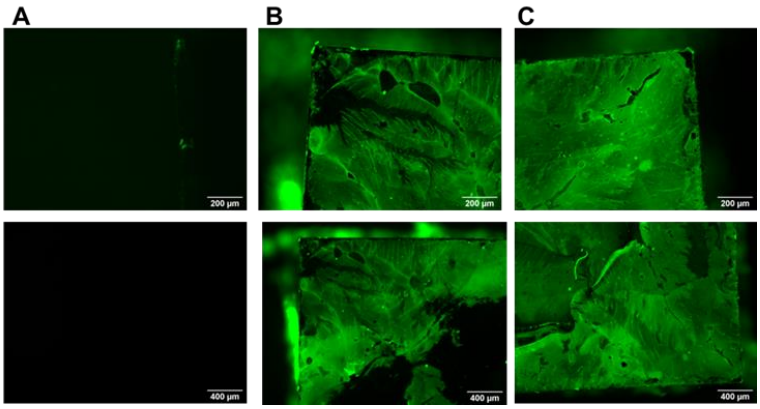

Figure 32 **-** LN distribution (in green) on unmodified parylene-c surfaces (A) and parylene surfaces coated with PEG-4MAL hydrogel decorated with site selective immobilized LN using 5 or 10 µM of NtA (B and C, respectively). Images were acquired with an inverted fluorescence microscope.

4.3.2. In vitro biological performance evaluation of the hydrogel coating

4.3.2.1. Cell adhesion of cortical neurons

Cortical neurons were seeded on unmodified parylene-c surfaces, parylene-c surfaces coated with bare PEG-4MAL hydrogel, or on parylene-c surfaces coated with PEG-4MAL hydrogel decorated with site-specific-immobilized LN using 5 or 10 µM of NtA. Cells were cultured for 24 h and processed for DNA staining, for subsequent quantification of cell adhesion, by quantifying the total area occupied by nuclei per sample surface, through image analysis. Fluorescence images revealed very few cells adhered to the bare PEG-4MAL hydrogel coating, as expected from the non-adhesive properties of PEG. Functionalization of the hydrogel coating with LN using 5 µM of NtA did not alter cell adhesion to the PEG-4MAL coating, while increasing the NtA concentration to 10 µM effectively promoted cell adhesion to the PEG-4MAL hydrogel coating (**Figure 33**). The subsequent quantitative image analysis of the total area of the nuclei per sample surface further supported the qualitative results (**Figure 34**). Although significant differences were not found among the three surfaces tested, a trend for higher numbers of cortical neurons was found on PEG-4MAL coatings decorated with site-specific immobilized LN, particularly for the highest NtA concentration tested (10 µM).

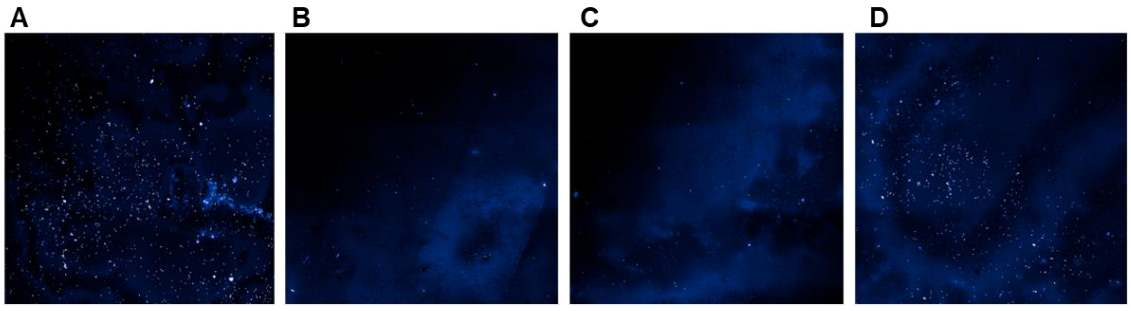

Figure 33 **-** Distribution of adhered cortical neurons on unmodified parylene-c surfaces (A), parylene-c surfaces coated with bare PEG-4MAL hydrogel (B), and parylene-c surfaces coated with PEG-4MAL hydrogel decorated with site-specific-immobilized LN using 5 or 10 µM of NtA (C and D, respectively). Images shown correspond to cell-seeded surfaces processed for DNA staining (in blue) after 24h of cell culture. Images and acquired with a high content screening system under confocal optical mode, using a 10× objective (scanned area ≅ 18 mm^2). The non-adhesive properties of the PEG-4MAL coating are evidenced, while its decoration with site-specific LN using the highest NtA concentration tested (10 µM) promoted cell adhesion.

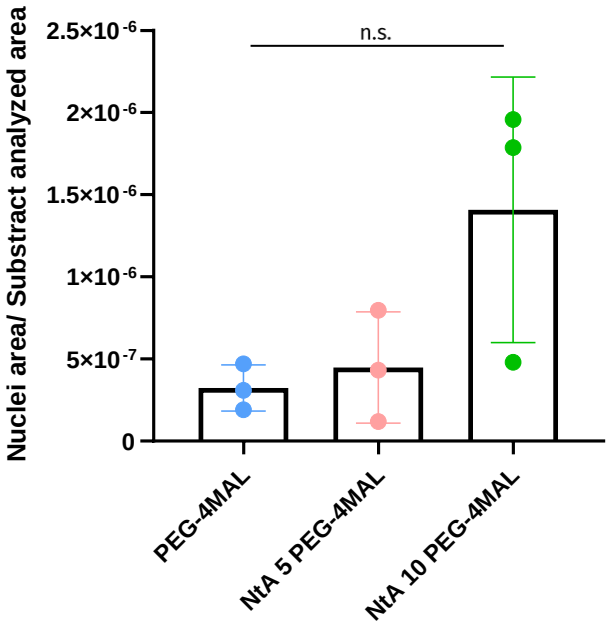

Figure 34 **-** Total area covered by the nuclei of adhered cortical neurons on parylene-c surfaces coated with bare PEG-4MAL hydrogel (PEG-4MAL) or PEG-4MAL hydrogel decorated with site-specific-immobilized LN using 5 or 10 µM of NtA (NtA 5 PEG-4MAL and NtA 10 PEG-4MAL, respectively). Cell-seeded surfaces were processed for DNA staining after 24h of cell culture. Results from a single independent experiment performed in triplicate are presented. A trend for higher cell adhesion is found for the highest NtA concentration used (10 µM), although no significant differences are found between groups (One-way ANOVA followed by Tuckey).

Conclusion and Future Perspectives

Chronically implanted neural electrodes trigger an inflammatory response eventually resulting in foreign body reaction, neuronal death, and ultimate electrode failure. To improve the tissue response to implanted electrodes, we designed a polymer coating for neural electrodes that consists of a non-fouling PEG-4MAL hydrogel coating exploring the bioactive effect of site-specific immobilized LN, a glycoprotein with reported neurite extension promoting ability. Parylene-c and PU substrates were used as surrogates of intracortical and deep brain electrodes, respectively since they are polymer coatings commonly employed to reduce FBR in clinical applications. The initial established goals can be outlined in 2 major sections: (a) Preparation and characterization of a hydrogel coating decorated with site-selective immobilized LN, and (b) Evaluation of the *in vitro* biological performance of the developed hydrogel coatings.

To assure a stable binding of the hydrogel, substrate surfaces were functionalized with maleimide (MAL) groups, through the surface functionalization with silane-PEG-maleimide, since this moiety binds covalently to the hydrogel precursor PEG-4MAL. Due to the hydrophobic nature of parylene-c and PU surfaces, both surfaces were activated with oxygenated groups via O_2 or UVO plasma, respectively, to introduce free hydroxyl groups (OH groups) at the surface, capable of reacting with silane groups. Different exposure times were used for surface activation of both substrates. The water contact angle confirmed the plasma treatment efficiency in both substrates since all the exposure times were able to decrease the water contact value obtained for unmodified substrates. For parylene-c substrates, the water contact angle value plateaued after 2 s, whereas in PU films, it required 200 s to reach a constant value. The presence of hydroxyl groups on the surfaces was confirmed by XPS measurements for all the exposure times. The higher concentration of these groups was obtained after 2 s, and after 300 s, for parylene-c and PU substrates, respectively. However, for PU films, since this feature does not significantly improve the surface hydrophilicity of 300 s compared to 200 s of plasma treatment, few changes are believed to have occurred in the PU surface between the two exposure times. Therefore, subsequent experiments were performed with PU surfaces activated for 200 s with UVO plasma.

Functionalization with silane-PEG-MAL with different concentrations was confirmed by quantification of maleimide groups present at the substrate surface. Results show that the higher concentration (25 mM) of the moiety used resulted in a higher maleimide surface density for both substrates. Additionally, for parylene-c substrates, longer exposure times to O_2 plasma did not result in higher maleimide surface densities. Thus, the shortest O_2 plasma treatment was chosen due to its higher ability to generate OH groups on parylene-c surfaces. However, since the 2 s O_2 treatment was difficult to replicate, 5 s treatments were selected for use in the subsequent assays. The surface roughness of PU changed comparatively to the activated surface; however, the surface roughness of parylene-c showed no discernible alterations. While results support the efficient functionalization of silane-PEG-MAL, is important to verify if the silane-PEG-MAL distribution is homogeneous, which is essential to allow a stable binding of the hydrogel. Studies are currently being carried out to characterize the surface distribution of maleimide groups, using a maleimide-reactive PEG conjugated to a fluorophore.

Due to time constraints, PEG-4MAL hydrogels were only formed on parylene-c surfaces. However, additional research is necessary to assess if the same approach can be used to produce PEG-4MAL-based hydrogel coatings on PU surfaces. Synthetic hydrogels based on PEG-4MAL and PEG-dithiol, through the Michael-type addition reaction were successfully deposited at parylene-c surface substrates. 2 and 4 treatments of PEG-4MAL/PEG-dithiol were analysed by AFM, showing distinct surface morphology compared with unmodified parylene surface. These differences were more evident after 4 treatments of PEG-4MAL/PEG-dithiol.

Assessing the film thickness is also a very important parameter regarding hydrogel characterization. It is important to correlate the number of treatments with the number of treatments used to form the

hydrogel in order to optimize the PEG-4MAL/ PEG-dithiol reaction. The thickness of the substrates was measured in the lab ellipsometer using a wet cell method. However, the results were unreliable due to the high standard deviation of the measurements. Further studies must be made. Additionally, hydrogel's Young modulus can be determined by analysis of atomic force microscopy (AFM) indentation. This technique is a simple method to evaluate the hardness and elastic modulus of thin films. While previous studies have determined that a final polymer density of 10% (w/v) is ideal to resemble brain tissue mechanical properties, it is crucial to verify the true value of our hydrogel's mechanical properties. However, the institute's equipment is unable to calibrate the laser for the time required to carry out the assay. Thus, this technique was not available to characterize the films, but it should be used going forward. Hydrogel stability is another important characteristic that must be assured. By exposing the substrates to ultrasounds for around two hours while they are hydrated, it is possible to assess the hydrogel's correct attachment and stability by evaluating ultrasounds' effect on hydrogel characteristics.

The deposition of a PEG-4MAL hydrogel decorated with site-specific immobilized laminin (LN) was performed on parylene surfaces subjected to a single PEG-4MAL/PEG-dithiol treatment, as a proof-of-concept. After one treatment, substrates were immersed in PEG-4MAL and then in NtA with two concentrations (5 and 10 µM). NtA was used to assure the exposure of LN bioactive domains upon its immobilization, via high-affinity binding.

LN immobilization was assessed at a first approach, examining LN distribution at the surface by immunofluorescence. Results confirmed the presence of LN on NtA-functionalized coatings, for the NtA concentrations tested. The ability of the developed coating to support cell adhesion of cortical neurons was subsequently assessed. A trend for higher numbers of adhered cells was found on PEG-4MAL coatings decorated with site-specific immobilized LN, when compared to bare PEG-4MAL coatings, particularly for the highest NtA concentration tested.

DNA fluorescent staining coupled with high content image analysis was used to assess biological performance. PEG-4MAL hydrogels confirmed their anti-fouling character by showing a minimal number of adhered cells, which is useful to reduce non-specific cell adhesion and protein absorption. No significant differences were observed between the number of cells of parylene-c surfaces coated with bare hydrogels and hydrogels functionalized with site-selective LN using NTA in both concentrations (5 and 10 µM). However, a tendency for the increase in the number of cells with the increase of NtA concentration is observed, which evidences the potentiality of this coating. Besides cell adhesion, it is also important to evaluate PEG-4MAL based coating decorated with site-selective immobilized LN influence on neurite outgrowth. Studies are being carried out to assess cell spreading by F-actin staining. Importantly, adding degradable cross-linkers to the hydrogels is another parameter that should be added in the future. The behaviour of the cortical neurons may be positively impacted by the introduction of a cell-degradable hydrogel to simulate the dynamic and reciprocal interactions between cells and their native surroundings.

A further advantage of PEG-4MAL hydrogels is their chemical versatility and robustness, which can be exploited to introduce different bioactive molecules to the hydrogel. The assessment of the additive or synergetic effect of other peptides besides LN on cortical neurons would be of great importance to reduce FBR.

One important observation is the need to assess neurite outgrowth and cell adhesion on hydrogel-coated surfaces in environments that replicate the pro-inflammatory conditions with which electrodes are confronted upon implantation. Co-culturing of neurons and astrocytes, while LPS and IFN were present, may serve as a representation of the unfavourable conditions to which electrodes are exposed.

Additionally, the 2D cell culture model is a good starting point, but the use of more complex *in vitro* systems is required to ascertain whether the coating is able to perform efficiently *in vivo*. Although both 2D and 3D systems have been employed for *in vitro* evaluation, they do not accurately reproduce the

host response to electrode surfaces because they lack vascular, BBB breach and inflammatory reactions, which influence greatly the electrode performance. It is important to develop substantial research focused on relevant *in vitro* biological platforms to increase their complexity to electrode evaluation before performing *in vivo* analysis.

Overall, these results suggest that the functionalization of parylene-c and PU-insulated electrodes with PEG-MAL-based hydrogels decorated with site-specific immobilized LN may be of interest to enhance the biocompatibility of electrode-neural interfaces. Further studies are required in order to further validate the present findings, and to assess the full potential of this engineered coating.

Appendix A

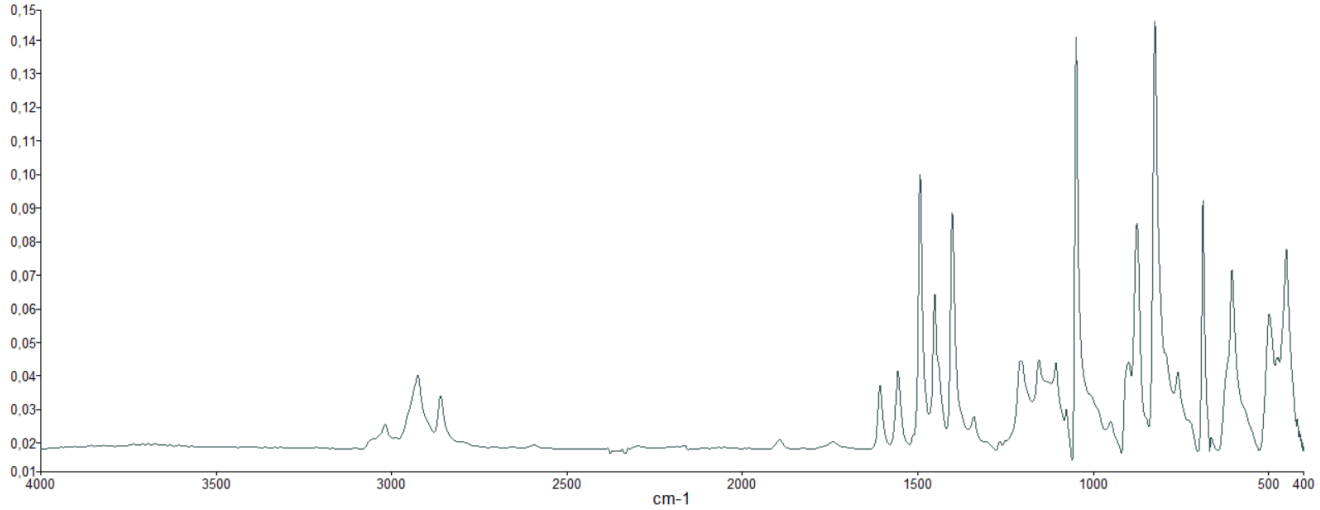

Figure A.1 **-** ATR-FTIR absorption spectrum of parylene-c surfaces activated with O_2 plasma (5 s).

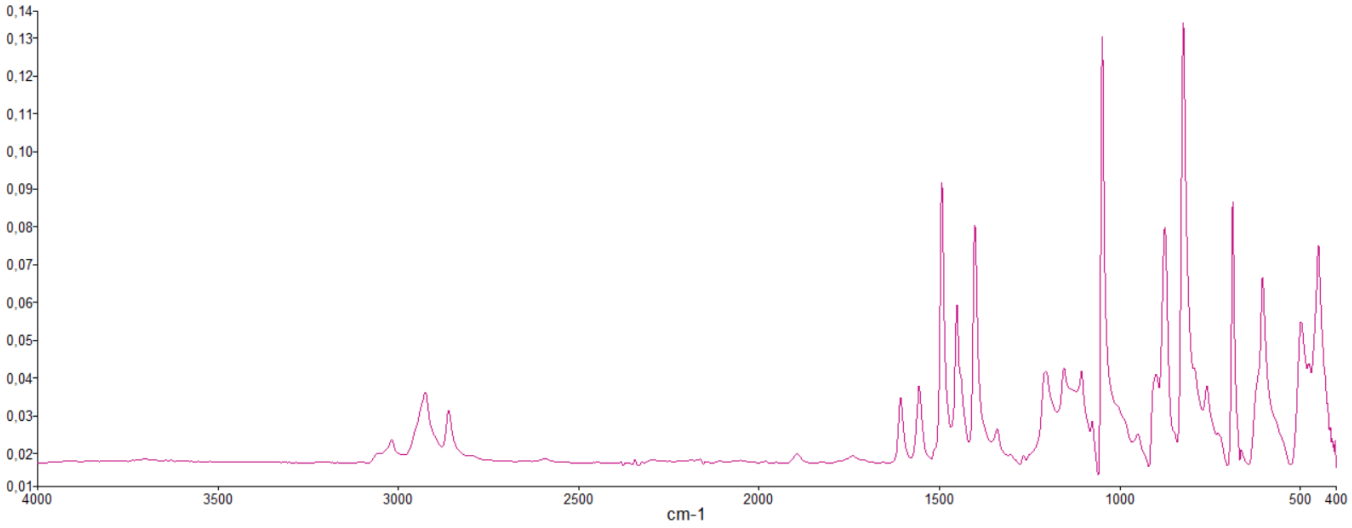

Figure A.2 **-** ATR-FTIR absorption spectrum of parylene-c surface functionalized with silane-PEG-MAL.

Appendix B

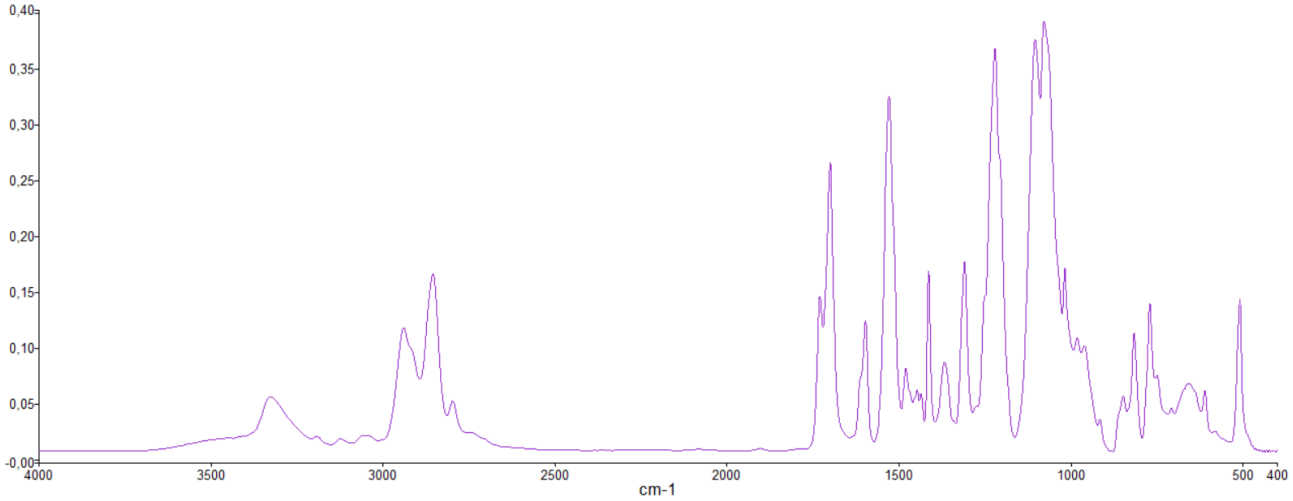

Figure B.1 - ATR-FTIR absorption spectrum of PU surface functionalized with silane-PEG-MAL.

Appendix C

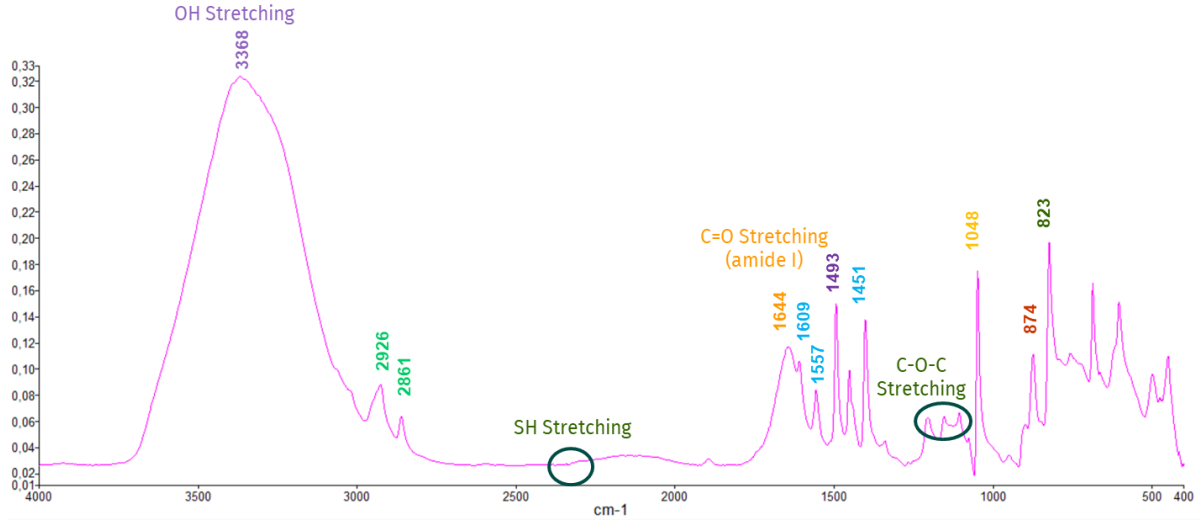

Figure C.1 **-** ATR-FTIR absorption spectrum of a parylene-c surface subjected to 4 4MAL/PEG-dithiol treatments.

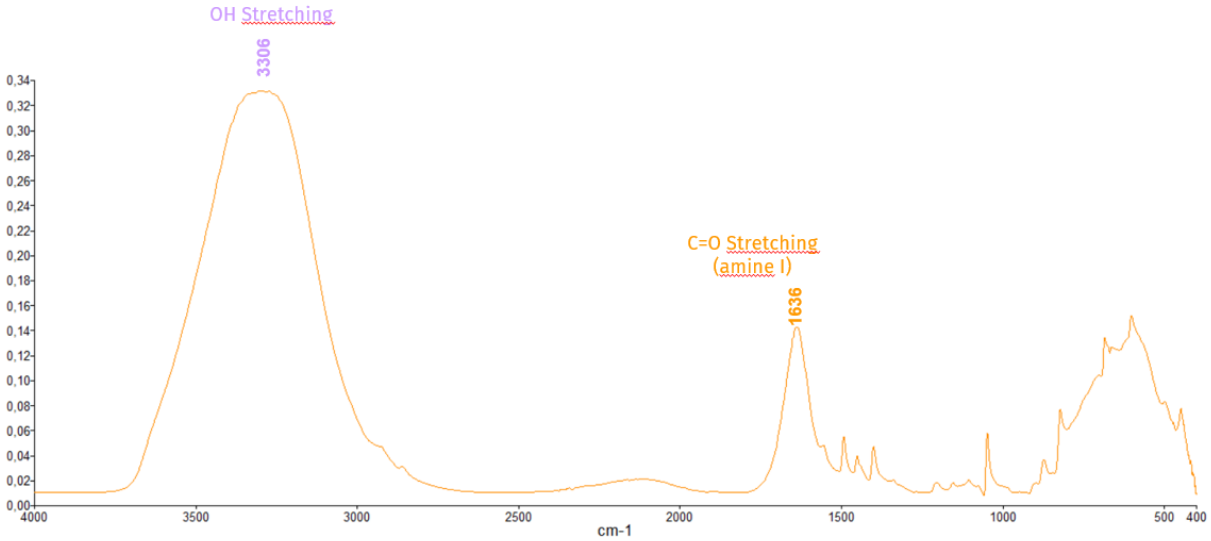

Figure C.2 **-** ATR-FTIR absorption spectrum of a parylene-c surface subjected to 6 4MAL/PEG-dithiol treatments.

Bibliography:

[1] A. M. M. Sousa, K. A. Meyer, G. Santpere, F. O. Gulden, e N. Sestan, «Evolution of the Human Nervous System Function, Structure, and Development», *Cell*, vol. 170, n. 2, pp. 226–247, doi: 10.1016/j.cell.2017.06.036.

[2] B. P. Daly, D. M. Eichen, B. Bailer, R. T. Brown, e C. L. Buchanan, «Central Nervous System», em *Encyclopedia of Human Behavior (Second Edition)*, V. S. Ramachandran, Ed. San Diego: Academic Press, pp. 454–459. doi: 10.1016/B978-0-12-375000-6.00084-7.

[3] Y. Shan, X. Cui, X. Chen, e Z. Li, «Recent progress of electroactive interface in neural engineering», *WIREs Nanomedicine and Nanobiotechnology*, p. e01827, doi: 10.1002/wnan.1827.

[4] W. M. Grill, S. E. Norman, e R. V. Bellamkonda, «Implanted Neural Interfaces: Biochallenges and Engineered Solutions», *Annual Review of Biomedical Engineering*, vol. 11, n. 1, pp. 1–24, doi: 10.1146/annurev-bioeng-061008-124927.

[5] B. He *et al.*, «Grand Challenges in Mapping the Human Brain: NSF Workshop Report», *IEEE Transactions on Biomedical Engineering*, vol. 60, n. 11, pp. 2983–2992, doi: 10.1109/TBME.2013.2283970.

[6] B. J. Edelman, N. Johnson, A. Sohrabpour, S. Tong, N. Thakor, e B. He, «Systems Neuroengineering: Understanding and Interacting with the Brain», *Engineering (Beijing)*, vol. 1, n. 3, pp. 292–308, doi: 10.15302/j-eng-2015078.

[7] S. Bhaskara, T. Sakorikar, S. Chatterjee, K. V. Shabari Girishan, e H. J. Pandya, «Recent advancements in Micro-engineered devices for surface and deep brain animal studies: A review», *Sensing and Bio-Sensing Research*, vol. 36, p. 100483, doi: 10.1016/j.sbsr.2022.100483.

[8] J. K. Chapin, K. A. Moxon, R. S. Markowitz, e M. A. Nicolelis, «Real-time control of a robot arm using simultaneously recorded neurons in the motor cortex», *Nat Neurosci*, vol. 2, n. 7, pp. 664–670, doi: 10.1038/10223.

[9] M. D. Serruya, N. G. Hatsopoulos, L. Paninski, M. R. Fellows, e J. P. Donoghue, «Instant neural control of a movement signal», *Nature*, vol. 416, n. 6877, Art. n. 6877, doi: 10.1038/416141a.

[10] M. A. Lebedev e M. A. L. Nicolelis, «Brain–machine interfaces: past, present and future», *Trends in Neurosciences*, vol. 29, n. 9, pp. 536–546, doi: 10.1016/j.tins.2006.07.004.

[11] A. Campbell e C. Wu, «Chronically Implanted Intracranial Electrodes: Tissue Reaction and Electrical Changes», *Micromachines*, vol. 9, n. 9, Art. n. 9, doi: 10.3390/mi9090430.

[12] M. A. Lebedev e M. A. L. Nicolelis, «Brain-Machine Interfaces: From Basic Science to Neuroprostheses and Neurorehabilitation», *Physiological Reviews*, vol. 97, n. 2, pp. 767–837, doi: 10.1152/physrev.00027.2016.

[13] A. E. Hramov, V. A. Maksimenko, e A. N. Pisarchik, «Physical principles of brain–computer interfaces and their applications for rehabilitation, robotics and control of human brain states», *Physics Reports*, vol. 918, pp. 1–133, doi: 10.1016/j.physrep.2021.03.002.

[14] N. J. Hill *et al.*, «Recording Human Electrocorticographic (ECoG) Signals for Neuroscientific Research and Real-time Functional Cortical Mapping», *J Vis Exp*, n. 64, p. 3993, doi: 10.3791/3993.

[15] B. Ji *et al.*, «Recent advances in wireless epicortical and intracortical neuronal recording systems», *Sci. China Inf. Sci.*, vol. 65, n. 4, p. 140401, , doi: 10.1007/s11432-021-3373-1.

[16] Y. Park, T. S. Chung, G. Lee, e J. A. Rogers, «Materials Chemistry of Neural Interface Technologies and Recent Advances in Three-Dimensional Systems», *Chem. Rev.*, vol. 122, n. 5, pp. 5277–5316, doi: 10.1021/acs.chemrev.1c00639.

[17] J. K. Krauss *et al.*, «Technology of deep brain stimulation: current status and future directions», *Nat Rev Neurol*, vol. 17, n. 2, pp. 75–87, doi: 10.1038/s41582-020-00426-z.

[18] R. L. Saldanha, M. E. Urdaneta, e K. J. Otto, «The Role of Electrode-Site Placement in the Long-Term Stability of Intracortical Microstimulation», *Front Neurosci*, vol. 15, p. 712578, doi: 10.3389/fnins.2021.712578.
[19] «Intracortical Microelectrode Array Unit Yield under Chronic Conditions: A Comparative Evaluation». https://www.mdpi.com/2072-666X/12/8/972
[20] M. Jorfi, J. L. Skousen, C. Weder, e J. R. Capadona, «Progress Towards Biocompatible Intracortical Microelectrodes for Neural Interfacing Applications», *J Neural Eng*, vol. 12, n. 1, p. 011001, doi: 10.1088/1741-2560/12/1/011001.
[21] J. O. Usoro, B. S. Sturgill, K. C. Musselman, J. R. Capadona, e J. J. Pancrazio, «Intracortical Microelectrode Array Unit Yield under Chronic Conditions: A Comparative Evaluation», *Micromachines (Basel)*, vol. 12, n. 8, p. 972, doi: 10.3390/mi12080972.
[22] B. Gunasekera, T. Saxena, R. Bellamkonda, e L. Karumbaiah, «Intracortical Recording Interfaces: Current Challenges to Chronic Recording Function», *ACS Chem. Neurosci.*, vol. 6, n. 1, pp. 68–83, doi: 10.1021/cn5002864.
[23] P. Lin, Y. Tsao, e L.-W. Kuo, *Controlling the Biocompatibility and Mechanical Effects of Implantable Microelectrodes to Improve Chronic Neural Recordings in the Auditory Nervous System*. IntechOpen, doi: 10.5772/intechopen.72659.
[24] B. S. Armour, E. A. Courtney-Long, M. H. Fox, H. Fredine, e A. Cahill, «Prevalence and Causes of Paralysis—United States, 2013», *Am J Public Health*, vol. 106, n. 10, pp. 1855–1857, doi: 10.2105/AJPH.2016.303270.
[25] V. K. Mushahwar, L. Guevremont, e R. Saigal, «Could cortical signals control intraspinal stimulators? A theoretical evaluation», *IEEE Transactions on Neural Systems and Rehabilitation Engineering*, vol. 14, n. 2, pp. 198–201, doi: 10.1109/TNSRE.2006.875532.
[26] K. C. Davis *et al.*, «Design-development of an at-home modular brain–computer interface (BCI) platform in a case study of cervical spinal cord injury», *Journal of NeuroEngineering and Rehabilitation*, vol. 19, n. 1, p. 53, doi: 10.1186/s12984-022-01026-2.
[27] J. J. Daly e J. R. Wolpaw, «Brain–computer interfaces in neurological rehabilitation», *The Lancet Neurology*, vol. 7, n. 11, pp. 1032–1043, doi: 10.1016/S1474-4422(08)70223-0.
[28] Y. Kasukawa *et al.*, «Advanced Equipment Development and Clinical Application in Neurorehabilitation for Spinal Cord Injury: Historical Perspectives and Future Directions», *Applied Sciences*, vol. 12, n. 9, Art. n. 9, doi: 10.3390/app12094532.
[29] T. Milekovic *et al.*, «Volitional control of single-electrode high gamma local field potentials by people with paralysis», *J Neurophysiol*, vol. 121, n. 4, pp. 1428–1450, doi: 10.1152/jn.00131.2018.
[30] «Brain-Computer Interfaces in Medicine - ClinicalKey». https://www.clinicalkey.com/#!/content/playContent/1-s2.0-S0025619612001231?returnurl=https:%2F%2Flinkinghub.elsevier.com%2Fretrieve%2Fpii%2FS0025619612001231%3Fshowall%3Dtrue&referrer=, Accessed 5/07/2022.
[31] «Intra-cortical brain-machine interfaces for controlling upper-limb powered muscle and robotic systems in spinal cord injury», *Clinical Neurology and Neurosurgery*, vol. 196, p. 106069, doi: 10.1016/j.clineuro.2020.106069.
[32] S. N. Flesher *et al.*, «A brain-computer interface that evokes tactile sensations improves robotic arm control», *Science*, vol. 372, n. 6544, pp. 831–836, doi: 10.1126/science.abd0380.
[33] D. A. Moses *et al.*, «Neuroprosthesis for Decoding Speech in a Paralyzed Person with Anarthria», *N Engl J Med*, vol. 385, n. 3, pp. 217–227, doi: 10.1056/NEJMoa2027540.
[34] A. B. Rapeaux e T. G. Constandinou, «Implantable brain machine interfaces: first-in-human studies, technology challenges and trends», *Current Opinion in Biotechnology*, vol. 72, pp. 102–111, doi: 10.1016/j.copbio.2021.10.001.
[35] F. R. Willett, D. T. Avansino, L. R. Hochberg, J. M. Henderson, e K. V. Shenoy, «High-performance brain-to-text communication via handwriting», *Nature*, vol. 593, n. 7858, Art. n. 7858, doi: 10.1038/s41586-021-03506-2.

[36] C. Pandarinath *et al.*, «High performance communication by people with paralysis using an intracortical brain-computer interface», *eLife*, vol. 6, p. e18554, doi: 10.7554/eLife.18554.
[37] A. B. Ajiboye *et al.*, «Restoration of reaching and grasping movements through brain-controlled muscle stimulation in a person with tetraplegia: a proof-of-concept demonstration», *The Lancet*, vol. 389, n. 10081, pp. 1821–1830, doi: 10.1016/S0140-6736(17)30601-3.
[38] «Brain-computer interface (BCI)», *Assignment Point*. https://assignmentpoint.com/brain-computer-interface-bci/, Accessed: 10/9/22.
[39] C. E. Bouton *et al.*, «Restoring cortical control of functional movement in a human with quadriplegia», *Nature*, vol. 533, n. 7602, Art. n. 7602, doi: 10.1038/nature17435.
[40] M. Capogrosso *et al.*, «A brain-spine interface alleviating gait deficits after spinal cord injury in primates», *Nature*, vol. 539, n. 7628, pp. 284–288, doi: 10.1038/nature20118.
[41] Y. Lee e S. B. Jun, «Strategies for minimizing glial response to chronically-implanted microelectrode arrays for neural interface», *Biomed. Eng. Lett.*, vol. 4, n. 2, pp. 120–128, doi: 10.1007/s13534-014-0134-2.
[42] M. Jakobs, A. Fomenko, A. M. Lozano, e K. L. Kiening, «Cellular, molecular, and clinical mechanisms of action of deep brain stimulation—a systematic review on established indications and outlook on future developments», *EMBO Molecular Medicine*, vol. 11, n. 4, p. e9575 doi: 10.15252/emmm.201809575.
[43] J. Frey *et al.*, «Past, Present, and Future of Deep Brain Stimulation: Hardware, Software, Imaging, Physiology and Novel Approaches», *Frontiers in Neurology*, vol. 13, 2022, https://www.frontiersin.org/articles/10.3389/fneur.2022.825178
[44] T. Koeglsperger, C. Palleis, F. Hell, J. H. Mehrkens, e K. Bötzel, «Deep Brain Stimulation Programming for Movement Disorders: Current Concepts and Evidence-Based Strategies», *Frontiers in Neurology*, vol. 10, 2019, https://www.frontiersin.org/articles/10.3389/fneur.2019.00410
[45] A. C. Meidahl, G. Tinkhauser, D. M. Herz, H. Cagnan, J. Debarros, e P. Brown, «Adaptive Deep Brain Stimulation for Movement Disorders: The Long Road to Clinical Therapy», *Mov Disord*, vol. 32, n. 6, pp. 810–819, doi: 10.1002/mds.27022.
[46] I. E. Harmsen *et al.*, «Clinical trials for deep brain stimulation: Current state of affairs», *Brain Stimulation*, vol. 13, n. 2, pp. 378–385, doi: 10.1016/j.brs.2019.11.008.
[47] M. Hariz, «My 25 Stimulating Years with DBS in Parkinson's Disease», *J Parkinsons Dis*, vol. 7, n. Suppl 1, pp. S33–S41, doi: 10.3233/JPD-179007.
[48] C. McKinnon *et al.*, «Deep brain stimulation: potential for neuroprotection», *Annals of Clinical and Translational Neurology*, vol. 6, n. 1, pp. 174–185, doi: 10.1002/acn3.682.
[49] N. Malek, «Deep Brain Stimulation in Parkinson's Disease», *Neurology India*, vol. 67, n. 4, p. 968, doi: 10.4103/0028-3886.266268.
[50] P. Blomstedt, G.-M. Hariz, M. I. Hariz, e L.-O. D. Koskinen, «Thalamic deep brain stimulation in the treatment of essential tremor: a long-term follow-up», *Br J Neurosurg*, vol. 21, n. 5, pp. 504–509, doi: 10.1080/02688690701552278.
[51] R. G. Cury, S. K. Kalia, B. B. Shah, J. Jimenez-Shahed, L. K. Prashanth, e E. Moro, «Surgical treatment of dystonia», *Expert Review of Neurotherapeutics*, vol. 18, n. 6, pp. 477–492, doi: 10.1080/14737175.2018.1478288.
[52] M. Vissani, I. U. Isaias, e A. Mazzoni, «Deep brain stimulation: a review of the open neural engineering challenges», *J. Neural Eng.*, vol. 17, n. 5, p. 051002, doi: 10.1088/1741-2552/abb581.
[53] A. M. Lozano *et al.*, «Deep brain stimulation: current challenges and future directions», *Nat Rev Neurol*, vol. 15, n. 3, pp. 148–160, doi: 10.1038/s41582-018-0128-2.
[54] B. R. Bloem, M. S. Okun, e C. Klein, «Parkinson's disease», *The Lancet*, vol. 397, n. 10291, pp. 2284–2303, doi: 10.1016/S0140-6736(21)00218-X.

[55] E. R. Dorsey *et al.*, «Projected number of people with Parkinson disease in the most populous nations, 2005 through 2030», *Neurology*, vol. 68, n. 5, pp. 384–386, doi: 10.1212/01.wnl.0000247740.47667.03.
[56] V. Rački *et al.*, «Cognitive Impact of Deep Brain Stimulation in Parkinson's Disease Patients: A Systematic Review», *Frontiers in Human Neuroscience*, vol. 16, 2022, https://www.frontiersin.org/articles/10.3389/fnhum.2022.867055
[57] «Current and future directions of deep brain stimulation for neurological and psychiatric disorders in: Journal of Neurosurgery Volume 131 Issue 2 (2019) Journals».
[58] M. Hariz e P. Blomstedt, «Deep brain stimulation for Parkinson's disease», *Journal of Internal Medicine*, doi: 10.1111/joim.13541.
[59] R. Mehanna e E. C. Lai, «Deep brain stimulation in Parkinson's disease», *Translational Neurodegeneration*, vol. 2, n. 1, p. 22, doi: 10.1186/2047-9158-2-22.
[60] H. Abboud *et al.*, «Comprehensive, Multidisciplinary Deep Brain Stimulation Screening for Parkinson Patients: No Room for "Short Cuts"», *Movement Disorders Clinical Practice*, vol. 1, n. 4, pp. 336–341, doi: 10.1002/mdc3.12090.
[61] M. G. Rizzone *et al.*, «Long-term outcome of subthalamic nucleus DBS in Parkinson's disease: From the advanced phase towards the late stage of the disease?», *Parkinsonism & Related Disorders*, vol. 20, n. 4, pp. 376–381, doi: 10.1016/j.parkreldis.2014.01.012.
[62] P. Limousin e T. Foltynie, «Long-term outcomes of deep brain stimulation in Parkinson disease», *Nat Rev Neurol*, vol. 15, n. 4, Art. n. 4, doi: 10.1038/s41582-019-0145-9.
[63] S. R. Potel, S. Marceglia, S. Meoni, S. K. Kalia, R. G. Cury, e E. Moro, «Advances in DBS Technology and Novel Applications: Focus on Movement Disorders», *Curr Neurol Neurosci Rep*, vol. 22, n. 9, pp. 577–588, doi: 10.1007/s11910-022-01221-7.
[64] M. Gulino, D. Kim, S. Pané, S. D. Santos, e A. P. Pêgo, «Tissue Response to Neural Implants: The Use of Model Systems Toward New Design Solutions of Implantable Microelectrodes», *Front. Neurosci.*, vol. 13, p. 689, doi: 10.3389/fnins.2019.00689.
[65] V. L. Feigin *et al.*, «Global, regional, and national burden of neurological disorders, 1990–2016: a systematic analysis for the Global Burden of Disease Study 2016», *The Lancet Neurology*, vol. 18, n. 5, pp. 459–480, doi: 10.1016/S1474-4422(18)30499-X.
[66] K. Gammon, «Neurodegenerative disease: Brain windfall», *Nature*, vol. 515, n. 7526, Art. n. 7526, doi: 10.1038/nj7526-299a.
[67] https://www.stratviewresearch.com e https://www.stratviewresearch.com/1646/neurotechnology-market.html, «Neurotechnology Market | Market Size, Share & Forecast Analysis», *stratviewresearch.com* Acessed: 15/06/2022
[68] «Deep Brain Stimulation Devices Market Size Report, 2030». https://www.grandviewresearch.com/industry-analysis/deep-brain-stimulators-dbs-market Accessed: 15/06/2022.
[69] «Brain Computer Interface Market Report, 2022-2030». https://www.grandviewresearch.com/industry-analysis/brain-computer-interfaces-market, Accessed: 15/06/2022.
[70] J. H. Jennings e G. D. Stuber, «Tools for Resolving Functional Activity and Connectivity within Intact Neural Circuits», *Curr Biol*, vol. 24, n. 1, pp. R41–R50, doi: 10.1016/j.cub.2013.11.042.
[71] J. C. Barrese, J. Aceros, e J. P. Donoghue, «Scanning electron microscopy of chronically implanted intracortical microelectrode arrays in non-human primates», *J Neural Eng*, vol. 13, n. 2, p. 026003, doi: 10.1088/1741-2560/13/2/026003.
[72] A. Prasad *et al.*, «Coupling biotic and abiotic metrics to create a testbed for predicting neural electrode performance», *Annu Int Conf IEEE Eng Med Biol Soc*, vol. 2011, pp. 3020–3023, doi: 10.1109/IEMBS.2011.6090827.

[73] V. Sankar, E. Patrick, R. Dieme, J. C. Sanchez, A. Prasad, e T. Nishida, «Electrode impedance analysis of chronic tungsten microwire neural implants: understanding abiotic vs. biotic contributions», *Front Neuroeng*, vol. 7, p. 13, doi: 10.3389/fneng.2014.00013.
[74] V. S. Polikov, P. A. Tresco, e W. M. Reichert, «Response of brain tissue to chronically implanted neural electrodes», *Journal of Neuroscience Methods*, vol. 148, n. 1, pp. 1–18, doi: 10.1016/j.jneumeth.2005.08.015.
[75] A. M. Jurga, M. Paleczna, e K. Z. Kuter, «Overview of General and Discriminating Markers of Differential Microglia Phenotypes», *Frontiers in Cellular Neuroscience*, vol. 14, 2020, https://www.frontiersin.org/articles/10.3389/fncel.2020.00198, Accessed 17/07/22.
[76] M. Pekny, U. Wilhelmsson, T. Tatlisumak, e M. Pekna, «Astrocyte activation and reactive gliosis—A new target in stroke?», *Neuroscience Letters*, vol. 689, pp. 45–55, doi: 10.1016/j.neulet.2018.07.021.
[77] D. H. Szarowski *et al.*, «Brain responses to micro-machined silicon devices», *Brain Research*, vol. 983, n. 1, pp. 23–35, doi: 10.1016/S0006-8993(03)03023-3.
[78] J. Groothuis, N. F. Ramsey, G. M. J. Ramakers, e G. van der Plasse, «Physiological Challenges for Intracortical Electrodes», *Brain Stimulation*, vol. 7, n. 1, pp. 1–6, doi: 10.1016/j.brs.2013.07.001.
[79] S. Moore *et al.*, «A role of oligodendrocytes in information processing», *Nat Commun*, vol. 11, n. 1, Art. n. 1, doi: 10.1038/s41467-020-19152-7.
[80] J. W. Salatino, K. A. Ludwig, T. D. Y. Kozai, e E. K. Purcell, «Glial responses to implanted electrodes in the brain», *Nat Biomed Eng*, vol. 1, n. 11, pp. 862–877, doi: 10.1038/s41551-017-0154-1.
[81] K. Woeppel, Q. Yang, e X. T. Cui, «Recent advances in neural electrode–tissue interfaces», *Current Opinion in Biomedical Engineering*, vol. 4, pp. 21–31, doi: 10.1016/j.cobme.2017.09.003.
[82] T. D. Y. Kozai, A. S. Jaquins-Gerstl, A. L. Vazquez, A. C. Michael, e X. T. Cui, «Brain Tissue Responses to Neural Implants Impact Signal Sensitivity and Intervention Strategies», *ACS Chem. Neurosci.*, vol. 6, n. 1, pp. 48–67, doi: 10.1021/cn500256e.
[83] S. M. Wellman, F. Cambi, e T. DY. Kozai, «The role of oligodendrocytes and their progenitors on neural interface technology: A novel perspective on tissue regeneration and repair», *Biomaterials*, vol. 183, pp. 200–217, doi: 10.1016/j.biomaterials.2018.08.046.
[84] J. S. Guimaraes, N. A. M. Lemos, M. A. M. Freire, A. Pereira, e S. Ribeiro, «Microelectrode implants, inflammatory response and long-lasting effects on NADPH diaphorase neurons in the rat frontal cortex», *Exp Brain Res*, doi: 10.1007/s00221-022-06434-3.
[85] R. Biran, D. C. Martin, e P. A. Tresco, «Neuronal cell loss accompanies the brain tissue response to chronically implanted silicon microelectrode arrays», *Experimental Neurology*, vol. 195, n. 1, pp. 115–126, doi: 10.1016/j.expneurol.2005.04.020.
[86] T. D. Y. Kozai *et al.*, «Chronic tissue response to carboxymethyl cellulose based dissolvable insertion needle for ultra-small neural probes», *Biomaterials*, vol. 35, n. 34, pp. 9255–9268, doi: 10.1016/j.biomaterials.2014.07.039.
[87] S. A. Liddelow *et al.*, «Neurotoxic reactive astrocytes are induced by activated microglia», *Nature*, vol. 541, n. 7638, Art. n. 7638, doi: 10.1038/nature21029.
[88] B. D. Winslow e P. A. Tresco, «Quantitative analysis of the tissue response to chronically implanted microwire electrodes in rat cortex», *Biomaterials*, vol. 31, n. 7, pp. 1558–1567, doi: 10.1016/j.biomaterials.2009.11.049.
[89] R. Biran, D. Martin, e P. Tresco, «The brain tissue response to implanted silicon microelectrode arrays is increased when the device is tethered to the skull», *Journal of Biomedical Materials Research A*, vol. 82A, pp. 169–178, doi: 10.1002/jbm.a.31138.
[90] G. C. McConnell, H. D. Rees, A. I. Levey, C.-A. Gutekunst, R. E. Gross, e R. V. Bellamkonda, «Implanted neural electrodes cause chronic, local inflammation that is correlated with

local neurodegeneration», *J. Neural Eng.*, vol. 6, n. 5, p. 056003, doi: 10.1088/1741-2560/6/5/056003.
[91] B. D. Winslow, M. B. Christensen, W.-K. Yang, F. Solzbacher, e P. A. Tresco, «A comparison of the tissue response to chronically implanted Parylene-C-coated and uncoated planar silicon microelectrode arrays in rat cortex», *Biomaterials*, vol. 31, n. 35, pp. 9163–9172, doi: 10.1016/j.biomaterials.2010.05.050.
[92] C. R. Butson, C. B. Maks, e C. C. McIntyre, «Sources and effects of electrode impedance during deep brain stimulation», *Clin Neurophysiol*, vol. 117, n. 2, pp. 447–454, doi: 10.1016/j.clinph.2005.10.007.
[93] K. L. Helton, B. D. Ratner, e N. A. Wisniewski, «Biomechanics of the Sensor-Tissue Interface—Effects of Motion, Pressure, and Design on Sensor Performance and the Foreign Body Response—Part I: Theoretical Framework», *J Diabetes Sci Technol*, vol. 5, n. 3, pp. 632–646, doi: 10.1177/193229681100500317.
[94] L. Karumbaiah *et al.*, «Relationship between intracortical electrode design and chronic recording function», *Biomaterials*, vol. 34, n. 33, pp. 8061–8074, doi: 10.1016/j.biomaterials.2013.07.016.
[95] D. R. Merrill, «Materials considerations of implantable neuroengineering devices for clinical use», *Current Opinion in Solid State and Materials Science*, vol. 18, n. 6, pp. 329–336, doi: 10.1016/j.cossms.2014.07.002.
[96] J. P. Harris *et al.*, «Mechanically adaptive intracortical implants improve the proximity of neuronal cell bodies», *J Neural Eng*, vol. 8, n. 6, p. 066011, doi: 10.1088/1741-2560/8/6/066011.
[97] J. Subbaroyan, D. C. Martin, e D. R. Kipke, «A finite-element model of the mechanical effects of implantable microelectrodes in the cerebral cortex», *J. Neural Eng.*, vol. 2, n. 4, pp. 103–113, doi: 10.1088/1741-2560/2/4/006.
[98] J. K. Nguyen *et al.*, «Mechanically-compliant intracortical implants reduce the neuroinflammatory response», *J. Neural Eng.*, vol. 11, n. 5, p. 056014, doi: 10.1088/1741-2560/11/5/056014.
[99] M. Ferguson, D. Sharma, D. Ross, e F. Zhao, «A Critical Review of Microelectrode Arrays and Strategies for Improving Neural Interfaces», *Advanced Healthcare Materials*, vol. 8, n. 19, p. 1900558, doi: 10.1002/adhm.201900558.
[100] K. M. Szostak, L. Grand, e T. G. Constandinou, «Neural Interfaces for Intracortical Recording: Requirements, Fabrication Methods, and Characteristics», *Front Neurosci*, vol. 11, p. 665, doi: 10.3389/fnins.2017.00665.
[101] D. Rodger *et al.*, «Flexible parylene-based multielectrode array technology for high-density neural stimulation and recording», *Sensors and Actuators B: Chemical*, vol. 132, n. 2, pp. 449–460, doi: 10.1016/j.snb.2007.10.069.
[102] H. S. Sohal, G. J. Clowry, A. Jackson, A. O'Neill, e S. N. Baker, «Mechanical Flexibility Reduces the Foreign Body Response to Long-Term Implanted Microelectrodes in Rabbit Cortex», *PLOS ONE*, vol. 11, n. 10, p. e0165606, doi: 10.1371/journal.pone.0165606.
[103] Z. J. Du *et al.*, «Ultrasoft microwire neural electrodes improve chronic tissue integration», *Acta Biomaterialia*, vol. 53, pp. 46–58, doi: 10.1016/j.actbio.2017.02.010.
[104] D. Kil, L. Brancato, e R. Puers, «Dextran as a fast resorbable and mechanically stiff coating for flexible neural probes», *J. Phys.: Conf. Ser.*, vol. 922, p. 012016, doi: 10.1088/1742-6596/922/1/012016.
[105] D. Kil *et al.*, «Dextran as a Resorbable Coating Material for Flexible Neural Probes», *Micromachines*, vol. 10, n. 1, Art. n. 1, doi: 10.3390/mi10010061.
[106] Y. S. Zhang e A. Khademhosseini, «Advances in engineering hydrogels», *Science*, vol. 356, n. 6337, p. eaaf3627, doi: 10.1126/science.aaf3627.
[107] H. Yuk, B. Lu, e X. Zhao, «Hydrogel bioelectronics», *Chem. Soc. Rev.*, vol. 48, n. 6, pp. 1642–1667, doi: 10.1039/C8CS00595H.

[108] Q. Liang *et al.*, «Highly Stretchable Hydrogels as Wearable and Implantable Sensors for Recording Physiological and Brain Neural Signals», *Adv Sci (Weinh)*, vol. 9, n. 16, p. 2201059, doi: 10.1002/advs.202201059.
[109] D.-H. Kim, J. A. Wiler, D. J. Anderson, D. R. Kipke, e D. C. Martin, «Conducting polymers on hydrogel-coated neural electrode provide sensitive neural recordings in auditory cortex», *Acta Biomater*, vol. 6, n. 1, pp. 57–62, doi: 10.1016/j.actbio.2009.07.034.
[110] L. Rao, H. Zhou, T. Li, C. Li, e Y. Y. Duan, «Polyethylene glycol-containing polyurethane hydrogel coatings for improving the biocompatibility of neural electrodes», *Acta Biomater*, vol. 8, n. 6, pp. 2233–2242, doi: 10.1016/j.actbio.2012.03.001.
[111] S. M. Gutowski *et al.*, «Host Response to Microgel Coatings on Neural Electrodes Implanted in the Brain», *J Biomed Mater Res A*, vol. 102, n. 5, pp. 1486–1499, doi: 10.1002/jbm.a.34799.
[112] A. N. Dalrymple *et al.*, «Electrochemical and biological performance of chronically stimulated conductive hydrogel electrodes», *J. Neural Eng.*, vol. 17, n. 2, p. 026018, doi: 10.1088/1741-2552/ab7cfc.
[113] K. C. Spencer, J. C. Sy, K. B. Ramadi, A. M. Graybiel, R. Langer, e M. J. Cima, «Characterization of Mechanically Matched Hydrogel Coatings to Improve the Biocompatibility of Neural Implants», *Sci Rep*, vol. 7, p. 1952, doi: 10.1038/s41598-017-02107-2.
[114] W. Shen *et al.*, «Extracellular matrix-based intracortical microelectrodes: Toward a microfabricated neural interface based on natural materials», *Microsyst Nanoeng*, vol. 1, n. 1, p. 15010, doi: 10.1038/micronano.2015.10.
[115] F. Vitale *et al.*, «Biomimetic extracellular matrix coatings improve the chronic biocompatibility of microfabricated subdural microelectrode arrays», *PLOS ONE*, vol. 13, n. 11, p. e0206137, doi: 10.1371/journal.pone.0206137.
[116] W. He, G. C. McConnell, e R. V. Bellamkonda, «Nanoscale laminin coating modulates cortical scarring response around implanted silicon microelectrode arrays», *J. Neural Eng.*, vol. 3, n. 4, pp. 316–326, doi: 10.1088/1741-2560/3/4/009.
[117] E. Azemi, C. F. Lagenaur, e X. T. Cui, «The surface immobilization of the neural adhesion molecule L1 on neural probes and its effect on neuronal density and gliosis at the probe/tissue interface», *Biomaterials*, vol. 32, n. 3, pp. 681–692, doi: 10.1016/j.biomaterials.2010.09.033.
[118] A. Nirwane e Y. Yao, «Laminins and their receptors in the CNS», *Biological Reviews*, vol. 94, n. 1, pp. 283–306, doi: 10.1111/brv.12454.
[119] D. Barros, I. F. Amaral, e A. P. Pêgo, «Laminin-Inspired Cell-Instructive Microenvironments for Neural Stem Cells», *Biomacromolecules*, vol. 21, n. 2, pp. 276–293, doi: 10.1021/acs.biomac.9b01319.
[120] A. Sonnenberg, C. J. Linders, P. W. Modderman, C. H. Damsky, M. Aumailley, e R. Timpl, «Integrin recognition of different cell-binding fragments of laminin (P1, E3, E8) and evidence that alpha 6 beta 1 but not alpha 6 beta 4 functions as a major receptor for fragment E8», *J Cell Biol*, vol. 110, n. 6, pp. 2145–2155, doi: 10.1083/jcb.110.6.2145.
[121] D. Harrison, S.-A. Hussain, A. C. Combs, J. M. Ervasti, P. D. Yurchenco, e E. Hohenester, «Crystal Structure and Cell Surface Anchorage Sites of Laminin α1LG4-5*», *Journal of Biological Chemistry*, vol. 282, n. 15, pp. 11573–11581, doi: 10.1074/jbc.M610657200.
[122] J. Ishihara *et al.*, «Laminin heparin-binding peptides bind to several growth factors and enhance diabetic wound healing», *Nat Commun*, vol. 9, n. 1, Art. n. 1, doi: 10.1038/s41467-018-04525-w.
[123] R. Timpl, D. Tisi, J. F. Talts, Z. Andac, T. Sasaki, e E. Hohenester, «Structure and function of laminin LG modules», *Matrix Biol*, vol. 19, n. 4, pp. 309–317, doi: 10.1016/s0945-053x(00)00072-x.

[124] K. J. Hamill, K. Kligys, S. B. Hopkinson, e J. C. R. Jones, «Laminin deposition in the extracellular matrix: a complex picture emerges», *Journal of Cell Science*, vol. 122, n. 24, pp. 4409–4417, doi: 10.1242/jcs.041095.
[125] W. R. Stauffer e X. T. Cui, «Polypyrrole doped with 2 peptide sequences from laminin», *Biomaterials*, vol. 27, n. 11, pp. 2405–2413, doi: 10.1016/j.biomaterials.2005.10.024.
[126] W. He e R. V. Bellamkonda, «Nanoscale neuro-integrative coatings for neural implants», *Biomaterials*, vol. 26, n. 16, pp. 2983–2990, doi: 10.1016/j.biomaterials.2004.08.021.
[127] D. Barros *et al.*, «An affinity-based approach to engineer laminin-presenting cell instructive microenvironments», *Biomaterials*, vol. 192, pp. 601–611, doi: 10.1016/j.biomaterials.2018.10.039.
[128] D. Barros *et al.*, «Engineering hydrogels with affinity-bound laminin as 3D neural stem cell culture systems», *Biomater. Sci.*, vol. 7, n. 12, pp. 5338–5349, doi: 10.1039/C9BM00348G.
[129] A. J. Allman *et al.*, «Xenogeneic extracellular matrix grafts elicit a TH2-restricted immune response», *Transplantation*, vol. 71, n. 11, pp. 1631–1640, doi: 10.1097/00007890-200106150-00024.
[130] C. M. Nolan, C. D. Reyes, J. D. Debord, A. J. García, e L. A. Lyon, «Phase Transition Behavior, Protein Adsorption, and Cell Adhesion Resistance of Poly(ethylene glycol) Cross-Linked Microgel Particles», *Biomacromolecules*, vol. 6, n. 4, pp. 2032–2039, doi: 10.1021/bm0500087.
[131] E. A. Phelps *et al.*, «Maleimide Cross-Linked Bioactive PEG Hydrogel Exhibits Improved Reaction Kinetics and Cross-Linking for Cell Encapsulation and In Situ Delivery», *Advanced Materials*, vol. 24, n. 1, pp. 64–70, doi: 10.1002/adma.201103574.
[132] W. M. Han *et al.*, «Synthetic matrix enhances transplanted satellite cell engraftment in dystrophic and aged skeletal muscle with comorbid trauma», *Science Advances*, vol. 4, n. 8, p. eaar4008, doi: 10.1126/sciadv.aar4008.
[133] S. M. Gutowski *et al.*, «Protease-degradable PEG-maleimide coating with on-demand release of IL-1Ra to improve tissue response to neural electrodes», *Biomaterials*, vol. 44, pp. 55–70, doi: 10.1016/j.biomaterials.2014.12.009.
[134] C. Boehler *et al.*, «Actively controlled release of Dexamethasone from neural microelectrodes in a chronic in vivo study», *Biomaterials*, vol. 129, pp. 176–187, doi: 10.1016/j.biomaterials.2017.03.019.
[135] W. P. Arend, «The balance between IL-1 and IL-1Ra in disease», *Cytokine & Growth Factor Reviews*, vol. 13, n. 4, pp. 323–340, doi: 10.1016/S1359-6101(02)00020-5.
[136] A. H. Taub, R. Hogri, A. Magal, M. Mintz, e Y. Shacham-Diamand, «Bioactive anti-inflammatory coating for chronic neural electrodes», *Journal of Biomedical Materials Research Part A*, vol. 100A, n. 7, pp. 1854–1858, doi: 10.1002/jbm.a.34152.
[137] Y. W. Fan, F. Z. Cui, S. P. Hou, Q. Y. Xu, L. N. Chen, e I.-S. Lee, «Culture of neural cells on silicon wafers with nano-scale surface topograph», *J Neurosci Methods*, vol. 120, n. 1, pp. 17–23, doi: 10.1016/s0165-0270(02)00181-4.
[138] E. S. Ereifej *et al.*, «Nanopatterning effects on astrocyte reactivity», *Journal of Biomedical Materials Research Part A*, vol. 101A, n. 6, pp. 1743–1757, doi: 10.1002/jbm.a.34480.
[139] C. A. R. Chapman *et al.*, «Nanoporous Gold as a Neural Interface Coating: Effects of Topography, Surface Chemistry, and Feature Size», *ACS Appl. Mater. Interfaces*, vol. 7, n. 13, pp. 7093–7100, doi: 10.1021/acsami.5b00410.
[140] P. Kuang, J.-H. Lee, C.-H. Kim, K.-M. Ho, e K. Constant, «Improved surface wettability of polyurethane films by ultraviolet ozone treatment», *Journal of Applied Polymer Science*, vol. 118, n. 5, pp. 3024–3033, doi: 10.1002/app.32712.
[141] «Resolving surface chemical states in XPS analysis of first row transition metals, oxides and hydroxides: Sc, Ti, V, Cu and Zn - ScienceDirect». https://www.sciencedirect.com/science/article/pii/S0169433210010287

[142] D. R. Baer *et al.*, «XPS guide: Charge neutralization and binding energy referencing for insulating samples», *Journal of Vacuum Science & Technology A*, vol. 38, n. 3, p. 031204, doi: 10.1116/6.0000057.
[143] R. Caldwell, M. G. Street, R. Sharma, P. Takmakov, B. Baker, e L. Rieth, «Characterization of Parylene-C degradation mechanisms: In vitro reactive accelerated aging model compared to multiyear in vivo implantation», *Biomaterials*, vol. 232, p. 119731, doi: 10.1016/j.biomaterials.2019.119731.
[144] B. Beamson, G. D., «High Resolution XPS of Organic Polymers: The Scienta ESCA300 Database», *ACS Publications*, https://pubs.acs.org/doi/pdf/10.1021/ed070pA25.5
[145] I. Horcas, R. Fernández, J. M. Gómez-Rodríguez, J. Colchero, J. Gómez-Herrero, e A. M. Baro, «WSXM: A software for scanning probe microscopy and a tool for nanotechnology», *Review of Scientific Instruments*, vol. 78, n. 1, p. 013705, doi: 10.1063/1.2432410.
[146] Z. Balion *et al.*, «Cerebellar Cells Self-Assemble into Functional Organoids on Synthetic, Chemically Crosslinked ECM-Mimicking Peptide Hydrogels», *Biomolecules*, vol. 10, n. 5, p. E754, doi: 10.3390/biom10050754.
[147] J. S. Song, S. Lee, S. H. Jung, G. C. Cha, e M. S. Mun, «Improved biocompatibility of parylene-C films prepared by chemical vapor deposition and the subsequent plasma treatment», *Journal of Applied Polymer Science*, vol. 112, n. 6, pp. 3677–3685, doi: 10.1002/app.29774.
[148] L. Brancato, D. Decrop, J. Lammertyn, e R. Puers, «Surface Nanostructuring of Parylene-C Coatings for Blood Contacting Implants», *Materials (Basel)*, vol. 11, n. 7, p. 1109, , doi: 10.3390/ma11071109.
[149] «Oxygen plasma functionalization of parylene C coating for implants surface: Nanotopography and active sites for drug anchoring - ScienceDirect». https://www.sciencedirect.com/science/article/pii/S0928493113003731
[150] «Oxygen plasma induced hydrophilicity of Parylene-C thin films - ScienceDirect». https://www.sciencedirect.com/science/article/pii/S0169433212012512
[151] T. Wang, B. Yang, X. Chen, X. Wang, C. Yang, e J. Liu, «Nonhomogeneous surface properties of parylene-C film etched by an atmospheric pressure He/O2 micro-plasma jet in ambient air», *Applied Surface Science*, vol. 383, pp. 261–267, doi: 10.1016/j.apsusc.2016.04.191.
[152] M. C. L. Martins, D. Wang, J. Ji, L. Feng, e M. A. Barbosa, «Albumin and fibrinogen adsorption on PU–PHEMA surfaces», *Biomaterials*, vol. 24, n. 12, pp. 2067–2076, doi: 10.1016/S0142-9612(03)00002-4.
[153] «Increased Wettability and Surface Free Energy of Polyurethane by Ultraviolet Ozone Treatment | IntechOpen». https://www.intechopen.com/chapters/48690 Accesses 6/06/2022
[154] J. Matinha-Cardoso *et al.*, «Surface activation of medical grade polyurethane for the covalent immobilization of an anti-adhesive biopolymeric coating», *J Mater Chem B*, vol. 9, n. 17, pp. 3705–3715, doi: 10.1039/d1tb00278c.
[155] J. M. Anderson e G. Voskerician, «The challenge of biocompatibility evaluation of biocomposites», em *Biomedical Composites*, L. Ambrosio, Ed. Woodhead Publishing, 2010, pp. 325–353. doi: 10.1533/9781845697372.3.325.
[156] V. Santucci, F. Maury, e F. Senocq, «Vapor phase surface functionalization under ultra violet activation of parylene thin films grown by chemical vapor deposition», *Thin Solid Films*, vol. 518, pp. 1675–1681, doi: 10.1016/j.tsf.2009.11.064.
[157] M. Bera, A. Rivaton, C. Gandon, e J. L. Gardette, «Comparison of the photodegradation of parylene C and parylene N», *European Polymer Journal*, vol. 36, n. 9, pp. 1765–1777, doi: 10.1016/S0014-3057(99)00259-1.

[158] M. J. Herman e M. W. Blair, «Determination of chemical decay mechanisms of Parylene-C during X-ray irradiation using two-dimensional correlation FTIR», *Polymer Degradation and Stability*, vol. 171, p. 109024, doi: 10.1016/j.polymdegradstab.2019.109024.
[159] L. Rao, H. Zhou, T. Li, C. Li, e Y. Y. Duan, «Polyethylene glycol-containing polyurethane hydrogel coatings for improving the biocompatibility of neural electrodes», *Acta Biomaterialia*, vol. 8, n. 6, pp. 2233–2242, doi: 10.1016/j.actbio.2012.03.001.
[160] H. Ishida e S. Ohba, «Synthesis and characterization of maleimide and norbornene functionalized benzoxazines», *Polymer*, vol. 46, n. 15, pp. 5588–5595, doi: 10.1016/j.polymer.2005.04.080.
[161] A. E. Abusrafa, S. Habib, e A. Popelka, «Surface Functionalization of a Polyurethane Surface via Radio-Frequency Cold Plasma Treatment Using Different Gases», *Coatings*, vol. 10, n. 11, Art. n. 11, doi: 10.3390/coatings10111067.
[162] Merck, «IR Spectrum Table». https://www.sigmaaldrich.com/PT/en/technical-documents/technical-article/analytical-chemistry/photometry-and-reflectometry/ir-spectrum-table Accesses 12/06/2022
[163] S. Sinha Ray, «Techniques for characterizing the structure and properties of polymer nanocomposites», em *Environmentally Friendly Polymer Nanocomposites*, S. Sinha Ray, Ed. Woodhead Publishing, pp. 74–88. doi: 10.1533/9780857097828.1.74.
[164] S. Gholizadeh, D. M. Lincoln, Z. Allahyari, L. P. Widom, R. N. Carter, e T. R. Gaborski, «Effects of Oxygen Plasma Treatment on Parylene C and Parylene N Membrane Biocompatibility for Tissue Barrier Models». bioRxiv, p. 2022.06.09.495451, doi: 10.1101/2022.06.09.495451.
[165] «Improved surface wettability of polyurethane films by ultraviolet ozone treatment - Kuang - 2010 - Journal of Applied Polymer Science - Wiley Online Library». https://onlinelibrary.wiley.com/doi/10.1002/app.32712, Accessed 24/08/2022.
[166] B. S. Elkin, A. I. Ilankovan, e B. Morrison, «A detailed viscoelastic characterization of the P17 and adult rat brain», *J Neurotrauma*, vol. 28, n. 11, pp. 2235–2244, doi: 10.1089/neu.2010.1604.
[167] S. Liu *et al.*, «Effects of the proportion of two different cross-linkers on the material and biological properties of enzymatically degradable PEG hydrogels», *Polymer Degradation and Stability*, vol. 172, p. 109067, doi: 10.1016/j.polymdegradstab.2019.109067.
[168] W. Gallagher, «FTIR Analysis of Protein Structure», p. 8.
[169] Y. Ji *et al.*, «DFT-Calculated IR Spectrum Amide I, II, and III Band Contributions of N-Methylacetamide Fine Components», *ACS Omega*, vol. 5, n. 15, pp. 8572–8578, doi: 10.1021/acsomega.9b04421.
[170] E. M. Davis, N. M. Benetatos, W. F. Regnault, K. I. Winey, e Y. A. Elabd, «The influence of thermal history on structure and water transport in Parylene C coatings», *Polymer*, vol. 52, n. 23, pp. 5378–5386, doi: 10.1016/j.polymer.2011.08.010.